Detailed Analyses and Numerical Modeling of a New Multi-Staged Fluidized-Bed Gasifier

Von der Fakultät für Maschinenbau, Verfahrens- und Energietechnik

der Technischen Universität Bergakademie Freiberg

genehmigte

Dissertation

zur Erlangung des akademischen Grades

Doktor-Ingenieur (Dr.-Ing.)

vorgelegt

von Diplom-Wirtschafts-Ingenieur Alexander Laugwitz
geboren am 28. Oktober 1983 in Berlin

Gutachter: Prof. Dr.-Ing. Bernd Meyer (TU Bergakademie Freiberg)

Prof. Dr.-Ing. Stefan Murza (Hochschule Augsburg)

Tag der Verleihung: 19.10.2017

Declaration

I hereby declare that I completed this work without any improper help from any third-party and without using any aids other than those cited. All ideas derived directly or indirectly from other sources are identified as such. In the selection and use of materials and in the writing of the manuscript I received support from the following persons:

- Prof. Dr. Bernd Meyer (supervisor)
- P. Rößger & L. Porter (hints on CFD Modeling and esp. visualization of results)
- Dr. A. Richter (hints on text and illustration)

Persons other than those above did not contribute to the writing of this thesis. I did not seek the help of a professional doctorate consultant. Only those persons identified as having done so received any financial payment from me for any work done for me.

This thesis has not previously been published in the same or a similar form in Germany or abroad.

Freiberg, 19.03.2017 Alexander Laugwitz

Acknowledgement

Ich danke meinem Doktorvater Prof. Bernd Meyer, dass ich mit seiner Unterstützung die vorliegende Arbeit am IEC verfassen konnte. Seine wissenschaftliche Expertise und sein Engagement für das IEC sowie die TUBAF haben mich stets motiviert seinem Vorbild zu folgen.

Außerdem möchte ich mich bei Dr. Martin Gräbner bedanken. Unter seiner hervorragenden Anleitung konnte ich mich in die Themen Kohlevergasung und Wirbelschichttechnik einarbeiten.

Von den vielen ausgezeichneten Kollegen die mich über die Jahre am Lehrstuhl begleitet haben möchte ich besonders Konrad Uebel, André Bader und Dr. Lars-Erik Gärtner meinen Dank aussprechen. Die vielen fruchtbaren Diskussionen zu Methodiken und Einsatzgrenzen von Simulations-Tools oder zur Didaktik beim Vermitteln von Wissen, aber auch die Formulierung von wissenschaftlichen Aufgaben entlang von technologischen Fragestellungen waren von unschätzbarem Wert für meine Tätigkeiten am Lehrstuhl.

Schließlich möchte ich mich bei Martin Schurz bedanken, der mit vorbildhaftem Engagement die COORVED Technikumsanlage aufgebaut und betrieben hat. Er war ein wichtiger Gesprächspartner um Fragen zum INCI Prozess und der COORVED Anlage zu diskutieren.

To Isabel

Table of Contents

Nomenclature

Symbol	Dimension	Meaning
Ar	m	Area of a fluidized bed, tube, reactor
Ar	-	Archimedes number (buoyancy/internal viscous forces)
Be	-	Beranek number (inertial force/buoyancy force)
C1	-	emperical constant in equations to calculate the point of fluidization
C2	-	emperical constant in equations to calculate the point of fluidization
C_D	-	drag function: e.g. Syamlal, Wen-Yu, Gidaspow
c_{fr}	-	coefficient of friction
D	m	reactor diameter
d*	-	normalized diameter ($d^*=Ar^{1/3}$)
D_0	m	nozzle diameter in jetting beds
$D_{0,hydr}$	m	hydraulic nozzle diameter in jetting beds
d_{bubble}	m	bubble diameter
D_i	m	spout draft tube diameter in spouted beds
d_p	m	particle diameter (specific surface equivalent)
d_{sp}	m	spout diameter
e	-	coefficient of restitution
f_d	-	$f_d=f(C_D)$;
Fr	-	Froude number (inertial force/gravity force)
Fr_{jet}	-	Froude number in jetting-fluidized beds
g_0	-	radial distribution function
G_{fr}	-	frictional modulus
H	m	reactor height
H_0	m	static bed height
H_f	m	height of fountain
H_{sp}	m	height of spouted bed
K_d		momentum exchange coeff.(gas/solids)
K_{ds}		momentum exchange coeff.(solid/solids)
l_b	m	bubble detaching lenght
L_c	m	cell size
Le	-	Lewis number
l_{jet}	m	jet length
$l_{jet\text{-}core}$	m	length of the jet core
l_{max}	m	maximal jet lenght
l_{min}	m	minimal jet lenght
m_s	kg	solids mass in a fluidized bed
Nu	-	Nusselt number
p	Pa	pressure
p´	Pa	pressure fluctuation
p_{fr}	Pa	frictional pressure
Pr	-	Prandtl number
p_s	Pa	solids pressure
$r_{1/2}$	m	Radial position at which the local jet velocity is half of its maximum
Re	-	Reynolds number (inertial force/ internal viscous force)
Re_{mf}	-	Reynolds number at point of fluidization
Re_p	-	Particle Reynolds numbern
Sh	-	Sherwood number
St	-	Stokes number
t_{rel}	s	particle relaxion tiem
u	m/s	superfical gas velocity
u*	-	normalized velocity ($u^*=Re/Ar^{1/3}$)
u**	-	normalized velocity ($u^{**}=(u-u_{mf})/(u_t-u_{mf})$)
u_{bg}	m/s	velocity of background gas in spout-fluid beds or jetting beds

u_{bubble}	m/s	bubble rise velocity
u_c	m/s	velocity resulting in maximum standard deviation in pressure fluctuations
u_{cf}	m/s	velocity at which all particles are fluidized for polydisperse bulk
$u_{cf,atm}$	m/s	velocity at which all particles are fluidized at atmospheric pressure for polydisperse bulk
$u_{cf,p}$	m/s	velocity at which all particles are fluidized at elevated pressure for polydisperse bulk
u_{jet}	m/s	initial superficial jet velocity
$u_{jet,z,b}$	m/s	jet velocity at the jet boundary
$u_{jet,z,max}$	m/s	maximal jet velocity along the axis
$u_{jet,z,r}$	m/s	jet velocity along the jet radius
u_k	m/s	velocity of fully developed turbulent bed
u_{mb}	m/s	minimum bubbling velocity
u_{mf}	m/s	minimum fluidization velocity
u_{msp}	m/s	minimum spouting velocity
u_s	m/s	solids velocity
$u_{s,z}$	m/s	vertical component of solids velocity
u_{se}	m/s	transport velocity, demacation between turbulent bed and fast-fluidized bed based on solids concentration profile
u_{sp}	m/s	spouting velocity
u_t	m/s	terminal velocity, single particle
$u_{t,rel}$	-	ratio of terminal velocities of multi particle system to single particle
u_{tr}	m/s	transport velocity, demacation between turbulent bed and fast-fluidized bed based on solids entrainment behaviour
Γ	°	cone angle in concial reactor geometries
γ_{jet}	°	jet half angle
Δp	Pa	pressure drop
ε	-	voidage (volume fraction gas; ($\varepsilon=1-\varepsilon_s$))
ε_{mf}	-	voidage at point of fluidization
ε_{patch}	-	voidage of an initially patched bed
ε_s	-	volume fraction solids ($\varepsilon_s=1-\varepsilon$)
$\varepsilon_{s,fr,max}$	-	friction packing limit
$\varepsilon_{s,max}$	-	maximum packing limit
η	kg/ms	dynamic viscosity
Θ		granluar temperature
λ_s	m^2/s	solids bulk viscosity
μ_s	Pas	solids shear viscosity
$\mu_{s,col}$	Pas	collisional part of the solids shear viscosity
$\mu_{s,fr}$	Pas	frictional part of the solids shear viscosity
$\mu_{s,kin}$	Pas	kinetic part of the solids shear viscosity arising from translation
ν	m^2/s	kinematic viscosity
ρ_f	kg/m^3	gas density
ρ_p	kg/m^3	apparent particle density
τ_s	-	solids stress tensor
Φ	°	angle of internal friction

Abbreviations

Abbreviation	Meaning
BGL	British Gas/Lurgi
CAE	Computer-Aided Engineering
FBDB	Fixed Bed Dry Bottom
FCC	Fluid Catalytic Cracking
BC	Boundary Condition
TFM	Two Fluid Model
KTGF	Kinetic Theory of Granular Flow

List of Figures

List of Tables

1 Introduction

This introduction provides the governing market situation under which needs the investigated coal gasifier is developed. Consequently, the second sub-section Objective of this Work is designated to explain how this thesis contributes to the development of a new gasifier.

1.1 Market Situation

The world market for coal gasification has seen a rapid increase over the last decade. Additionally, the worldwide syngas capacity (from all types of feedstock) is forecasted to more than double up from 147 GW_{th} (production capacity in 2015) to approx. 359 GW_{th} in 2020 [1]. Currently, approx. 170 million tons of coal are gasified per year, which is nearly as much as the total coal production rate in Germany 2014 (Germany ranks place 8 in the list of coal producing countries, by annual production rate and it is the largest producer in the EU). This demonstrates the significance of gasification technology.

Monitoring and evaluation of the coal gasification market reveals some major trends: 93% of the worldwide produced syngas is used for the production of chemicals and fuels (liquid and gaseous). Only a few coal gasification projects are IGCC power plants for low-emission, coal-based electricity generation [2]. In terms of feedstocks, it can be shown that 75% of syngas is produced from coal [1]. Additionally, it is known that more and more fluctuating coal menus are fed to gasifiers. This is encompassed with alternating coal qualities in terms of e.g. heating value, ash content, ash melting properties, reactivity and content of hazardous trace components (Hg, Cl, S, Na, K, As, Se, Cd, Cr, V, Pb, Ni ...). The reasons for fluctuating coal menus are manifold. Often, it is a result of the global trend to reduce coal-based power production for ecological reasons. Freed coal pushes into the gasification market. This causes operators to deal with coals other than the specified design coal/project coal.

Another feedstock-trend is the increasing market share of coals with a high-ash content [3], [4], [5], [6] and high ash-melting temperature. Moreover, modern technologies for mining and coal preparation cause an increasing fraction of coal fines to be produced [7], [8], [9]. As a result, high-ash coal fines (dry ash scontent >25 wt%, particle size with 90 wt% between 0 and 0.5 mm) push into the market [10].

Besides the feedstock situation, there is also a global trend for the investigated technology. An increasing number of gasification-technology vendors and new gasifiers are present in the market. Companies from China have developed most of these new gasifiers [11], [12]. A few are developed in the USA [13], [14] and in other countries e.g. Germany,

Japan, or Russia. Additionally, the well-established vendors are constantly developing and adapting their technology to cope with changing market needs, as summarized in Meyer [15] and Nikrityuk et al. [16]. In general, there is an increasing diversity in operating and planned gasifiers reflecting the diverging costumers needs for gasification products and applicable feedstocks. This trend is quantified in Table 1. Here, the most important gasifier vendors are shown. In 2014 Shell and GE had a 50% market share. In 2019 they will have only approx. one third whilst others will increase their market share (e.g. GSP, E-Gas, HT-L, OMB). These intense commercial R&D activities also prove the current and foreseen potential for coal gasification.

Finally, a trend towards larger projects is evident. Thus, the single unit capacity is increased to 3000 tpd (operating OMB gasifier) [17] and 5000 tpd (offered by KBR) [14], respectively. In addition to larger single unit capacities, more gasifiers are applied per project. The latest example is the second Nangxia coal-to-liquids project. Here, 24 Shenhua gasifiers (comparable to GSP gasifier) are employed to convert 20 mill tons of coal per year to 2.73 mill tons FT-diesel, 0.98 mill tons naphta and 1.0 mill tons other products [18].

However, still there is no commercial gasifier for high-ash coal fines available. The reasons and drawbacks of existing gasifiers are explained in Chapter 2.1. As a result, millions of tons of high-ash coal fines are stockpiled each year [19], [20], [21]. These unused leftovers accrue mainly from conventional coal combustion plants and coal gasification plants. If technologically feasible, their conversion would be a rewarding endeavor [21]. A promising solution to utilize this feedstock is presented in a patent from Meyer et al. [22].

Here, a staged fixed-bed and fluidized-bed gasification process is introduced. Gräbner and Meyer [23] compared this approach against conventional and innovative entrained-flow gasifiers. In this work, the thermodynamical advantages of the patented gasification principle were demonstrated. Currently this new gasification approach is demonstrated at the Technical University Bergakademie Freiberg in a lab-scale unit. The present thesis contributes to the development of this gasifier. The main objective is to describe, discuss and understand the gas-solid flow in this reactor.

Table 1 Market share for most successful gasifiers, adapted from Higman [1]

Installed capacity in GW_{th}	Operating 2014	Under construct. 2016	Planned 2019	Share 2014	Share 2019
GE (entrained flow, slurry)	30	43	46	25	19
Shell (entrained flow, dry)	30	32	39	25	16
Lurgi FBDB (fixed bed, dry)	19	20	21	16	9
OMB (entrained flow, slurry)	7	18	20	6	8
SEDIN (fixed bed, dry)	6	11	20	5	8
GSP (entrained flow, dry)	2	14	17	2	7
E-Gas (entrained flow, slurry)	1	11	17	1	7
HT-L (entrained flow, dry)	2	9	13	2	5
MCSG (entrained flow, slurry)	5	5	6	4	3
Others	17	35	44	14	18

1.2 Objective Work

The first objective is to provide tools to facilitate the understanding of the hydrodynamics inside a new, staged coal gasifier. Three computer-aided engineering (CAE) approaches to investigate the hydrodynamics will be comprehensively introduce and applied to the gasifier. A regime diagram according to Reh [24], ASPEN Plus® simulations and CFD simulations. This work intends to show, which type of information can be gained from the different tools at which degree of detail and reliability.

The reliability depends on the quality of model validation. Thus, the second objective of this work is to provide guidelines how to identify suitable validation experiments. Consequently experiments for each of the zones in the new staged gasifier are identified as validation experiments.

The third objective is to apply CFD to calculate each validation experiment with the same numerical setup at a reasonable accuracy. The validated CFD setup shall be successfully applied to calculate the new gasifier with its staged zones.

1.3 Structure of this Work

First, it is necessary to discuss the drawbacks of available gasifiers and deduce requirements of the new gasifier. For this, Chapter 2.1 introduces three types of gasifiers (fixed bed, fluidized bed, entrained flow). Their drawbacks regarding gasification of high-ash coals are highlighted. It is deduced that the new gasifier should be a fluidized-bed system providing complete carbon conversion.

As the new gasifier will be a staged fluidized-bed gasifier, the principles and methods to describe fluidized-bed systems have to be discussed. Hence, Chapter 2.2, discusses the relevant types of fluidized beds and its measures.

In the following, the general applicability and fundamentals of CAE tools to asses fluidized beds are described. Those tools encompass 0D flow regime diagrams (Chapter 3.1), 1D hydrodynamic calculators (Chapter 3.2) and 3D computational fluid dynamics (Chapter 3.3).

Before the new, staged coal gasifier can be assessed with those tools, the reactor principle will be introduced in Chapter 4. Here, emphasis is put on the hydrodynamics.

Subsequently, the hydrodynamics in the gasifier are visualized in different regime diagrams in Chapter 5.

The main part of this work is designated to CFD simulations. First, the applied software package and model implementation is verified in Chapter 6.1. The fundamental question of required computational-grid resolution and the need for validation are discussed in Chapter 6.2 and Chapter 6.3. After that, two validation experiments are identified and calculated in Chapter 6.3 and Chapter 6.4. The validated setup is then applied to the new gasifier in Chapter 6.5.

Finally, a simplified 1D approach is first validated in Chapter 7.1 before it can be used to calculate the new gasifier in Chapter 7.2.

Chapter 8 is designated to summarize the findings and Chapter 9 provides an outlook.

2 Fundamental Considerations

There is a vast amount of literature on the nature of coal [25], [26], [27], [28] and coal gasification [29], [30], [10] [31], [32], [33], [34]. A comparable amount of literature can be found for the principles of fluidization and fluidized-bed technologies, e.g., [35], [36], [37], [38], [39], [40], [41], [42], [43]. Thus, only a few relevant aspects are highlighted in the following, rather than providing an extended introduction to these topics.

2.1 Fundamentals of Gasification and Gasifiers

In an autothermal gasification process, sub-stoichiometric amounts of oxygen are contacted with the feedstock. The fed oxygen enables exothermic reactions. Those are required to provide the necessary heat for drying, devolatilization and other endothermal reactions (compare [44], [30]). By this partial oxidation, only a minor part of the feedstocks heating value is consumed to provide sensible heat. The majority is captured in the produced raw gas. Depending on the applied reactor type and other boundary conditions, the resulting cold-gas efficiency (ratio of the absolute heating values of feedstock input to the absolute heating values of produced raw gas) ranges between 63 and 85% [45].

Thus, by means of coal gasification, the heterogeneously composed and difficult to transport and handle feedstock is converted into a raw gas with a homogeneous composition that can easily be transported, further treated and exploited. The cleaned syngas can be utilized in manifold ways [46], [34]. Today, 65% from the totally produced syngas (147 GW_{th}) is converted into chemicals (methanol and its non-fuel-derivatives, olefins, oxo-alcohols, ammonia, urea, hydrogen, ...), 18% into liquid fuels (diesel, kerosene, naphtha, ...) 10% into gaseous fuels (e.g. substitute natural gas) and 7% into power (IGCC power plants, polygeneration) [46]. As shown in Figure 1 there are vast possible products and different applicable solid, liquid and gaseous feedstocks. However, 75.5% of the gasified feedstock is coal with an even increasing share (83% by 2020) [1].

Coal is comparably cheap and more or less equally distributed amongst the countries [47]. It´s availability and comparably high reserves at low prices are the main drivers for coal-to-X projects. Here, power production in an IGCC power plant has a lower environmental footprint compared to conventional coal to power stations [48], [49]. On the other hand, IGCC power production is well known to be more expensive. Additionally, the added value from domestic coal to fuels and coal to chemicals is larger than conventional coal to power and much higher than importing and only refining oil [50]. This explains

the dominance of chemicals and fuels production from coal over IGCC power plants in terms of installed capacity.

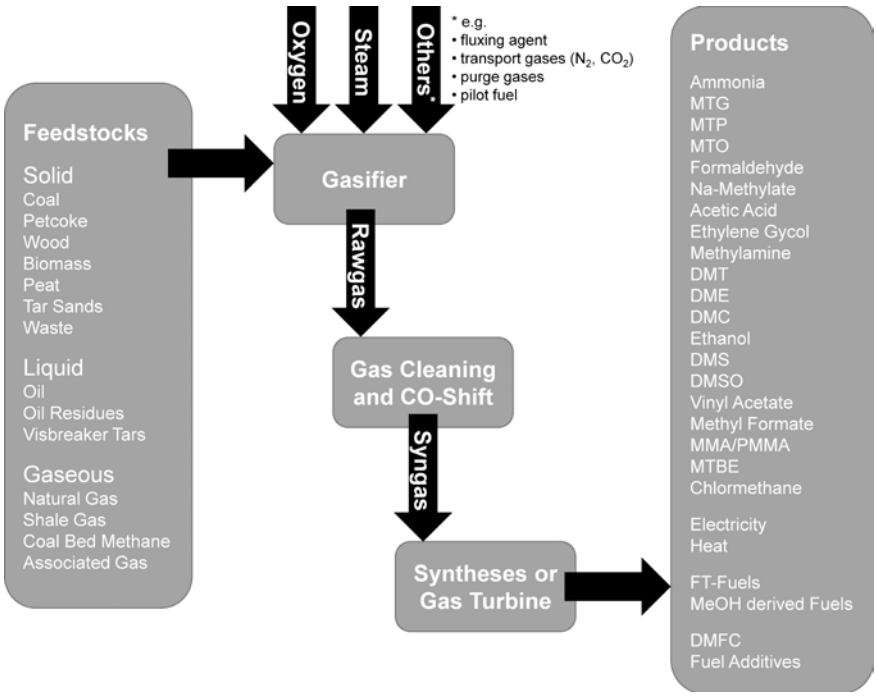

Figure 1 Examples of gasification feedstocks and syngas utilization

Since the beginning of industrial coal gasification in the early 20th century, many different types, ranks and qualities of coals have been converted into syngas [30], [29]. For this, different types of gasifiers have evolved. Those gasifiers can be classified according to different features [10] such as e.g.:

- bed type (fixed bed, fluidized bed, entrained flow)
- wall type (refractory lined, membrane wall, steam jacket)
- operational temperature (usually either above ash-fluid temperature or below the temperature of initial ash deformation, in a few cases at ash agglomerating conditions)
- coal feeding (dry via lock hoppers, dry via solid pumps, slurry)
- raw gas cooling (heat exchangers, chemical quench, water quench)

Other distinguishing features would be e.g. the operational pressure, oxygen purity, addition of fluxing agents or addition of catalysts.

For this thesis, the bed type and operational temperature are most interesting and will be further explained. All commercially available coal gasifiers can be clearly assigned to a fixed-bed, fluidized-bed or entrained-flow reactor type, compare Figure 2. Despite the commercially offered variety, none of the available gasifiers is thermodynamically, hydrodynamically and economically suitable for conversion of high-ash coal fines, as explained

in the following sub-sections. Even though suggested by different authors (e.g. [51], [52], [53], [54], [55]), there is no combination of bed types commercially offered, yet.

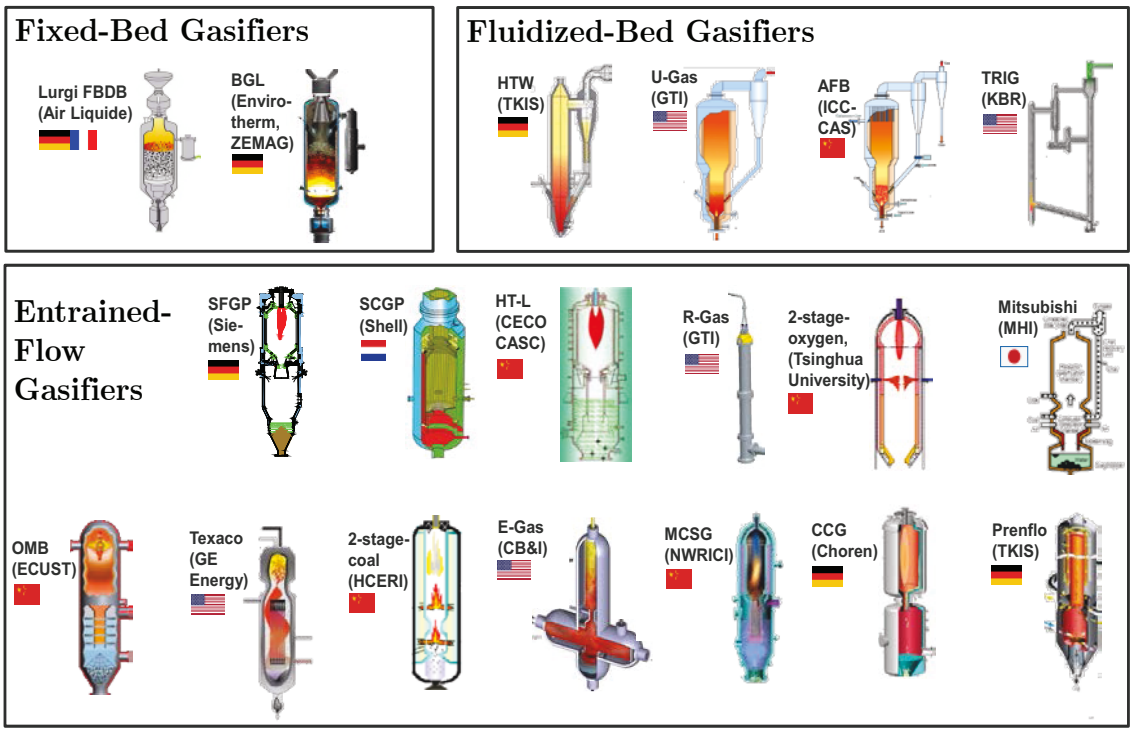

Figure 2 Overview of types of commercially available gasifiers

2.1.1 Counter-Current Fixed-Bed Gasifiers

Commercial fixed-bed coal gasifiers are fed from the top and the gasification agent flows in counter-current direction from the bottom to the top. The highest oxygen concentration is found at the very bottom. Here, an oxidation zone forms in which all the oxygen is consumed. Above the oxygen containing zone, endothermic conversion of devolatized coke takes place in the gasification zone. The produced gas flows upwards and provides heat for the devolatilization and drying of coal in the two respective zones above. This internal integration of combustion heat results in lowest oxygen consumption and the lowest raw-gas outlet temperature (350 – 800°C) compared to other gasifier types, [10]. Actually, this makes fixed-bed gasifiers most suitable for high-ash coals if the particle size is feasible.

Due to the low gas outlet temperatures, noticeable amounts of methane and higher hydrocarbons (tars, oils) can be found in the raw gas. Thus, the syngas-yield is lower compared to fluidized-bed and entrained-flow gasifiers, even though the cold-gas-efficiency is superior. The gas composition is especially suitable for the production of substitute natural gas (SNG) as up to 12 $wt\%_{dry}$ of CH_4 can be found in the syngas. On the other hand, production of chemical precursors such as methanol and its derived products will have a poor efficiency. In addition a considerable amount of tars and oils are produced, as the

devolatilization gases are not cracked in a hot zone in this type of gasifier. Separation and treatment of tars and oils is difficult and only a small fraction can be sold after upgrading.

However, the solid bottom product is virtually free from carbon. It is discharged as dry ash by means of a rotating grate and rabble rakes (e. g. Lurgi fixed bed dry bottom (FBDB®) gasifier, SEDIN gasifier) or as liquid slag through a tap hole (Britsh Gas/Lurgi (BGL) gasifier, compare Figure 3). All fixed-bed gasifiers are dry fed with the comparably largest coal particle size from 3 mm to 60 mm, [10]. Fines need to be removed during the feedstock preparation by means of sieving. Otherwise, fines would block the free gas paths between the particles. This would result in an instable gas flow through the particle bed. Consequences would be an unequal distribution of reactant gas over the bed diameter and prohibitive fluctuations in pressure drop. The former results in an incomplete carbon conversion and hot spots in the packed bed. The latter results in random gas eruptions at the top of the bed and accompanied increase in particle carry over.

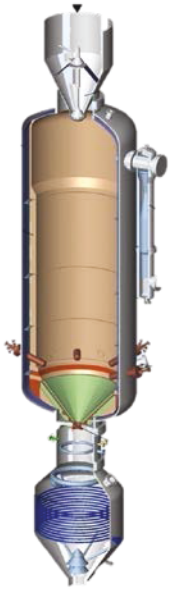

Figure 3 Example for fixed-bed gasification - BGL gasifier, adapted from Hirschfelder [56]

The addressed feedstock in this thesis (high-ash coal fines) cannot be gasified in fixed-bed gasifiers. Additionally, caking coals are difficult to gasify as they tend to produce packed beds of insufficient porosity. Further fundamentals on fixed-bed gasifiers can be found elsewhere [10], [30], [34], [57]. Former and recent R&D activities and current projects for BGL can be found e. g. in [58], [59], [60] and for Lurgi FBDB® e. g. in [61], [62]. Here it is shown how the vendors develop their gasifiers towards higher operational pressure, larger size of a single unit and higher availability as well as feedstock flexibility. Figure 3 shows the BGL fixed-bed gasifier as the only example for a combination of fixed-bed gasification and liquid slag discharge.

2.1.2 Fluidized-Bed Gasifiers

As explained in more detail in Chapter 2.2, there are different forms of appearance of fluidized beds. Most of which have already been commercially applied to gasification. As an example, the High-Temperature Winkler (HTW) gasifier operates according to a stationary, bubbling fluidized bed (see Figure 4) [63], [64]. Circulating-fluidized-bed gasification is commercially offered by e. g. Foster Wheeler [42], Outotec [65], Andritz [66] or Envirotherm [56]. These systems operate only at near atmospheric pressures.

Fast-fluidized-bed coal gasification is offered by KBR [14]. Here, operational principles from fluid catalytic cracking (FCC) technology is adapted. Jetting-fluidized-bed coal gasification was developed by GTI [67], [68] (now commercialized by SES [69]) and Kellog-Rust-Westinghouse (KRW) [70]. Spouted-bed coal gasifiers were developed e. g. by British Coal [71].

Regardless, the mode of fluidization, all fluidized-bed gasifiers are dry fed with particle sizes between 0.5 mm and 6 mm. They have a dry-ash discharge and a moderate consumption of steam and oxygen. Syngas quality is better compared to fixed-bed gasifiers as no higher hydrocarbons can be found. The methane content is around 5 $wt\%_{dry}$ owing to the operation temperatures. Typical gas outlet temperatures are between 850°C and 950°C [10]. Gasification temperatures below the ash melting are disadvantageous for higher rank coals as the reactivity is usually lower compared to low rank coals. Thus, the carbon conversion is poor at these gasification temperatures. On the other hand, because of the moderate temperatures, fluidized-bed gasifier have a thermodynamical advantage compared to entrained-flow gasifiers. This becomes especially evident for high-ash coals. As neither the heat of ash fusion, nor the sensible heat for heating the ash to higher temperatures is required [45]. Thus, in general, fluidized-bed are very promising for conversion of high-ash coal fines. But still, fluidized-bed gasifiers strongly lack behind fixed-bed gasifiers and entrained-flow gasifiers in terms of installed capacity. In fact, there are only a very few commercial demonstrations of coal gasification in fluidized beds [42].

The major drawback is the incomplete carbon conversion. This is a result of the residence time distribution and solids back-mixing of this reactor type (according to continuously stirred tank reactor). As a consequence, both the bottom ash (up to 5-25 wt% C-content) and fly ash (up to 50-60 wt% C-content) contain considerable amount of unconverted carbon [63], [68]. Carbon content depends on coal reactivity and mean gasification temperature. The fly ash needs to be separated from the raw gas (e. g. cyclones and candle filters) and is usually recycled back to the gasifier. This increases the complexity of the plant layout. The bottom ash contains too much carbon to be disposed. It must be post-combusted, which is in most cases done in an external combustion plant. Hence, the overall efficiency is depressed.

Reducing the carbon loss from fluidized-bed gasifiers would be a major breakthrough for the conversion of both high-ash coals and conventional coals in fluidized beds.

In the most cases fluidized-bed gasifier achieve thermal capacities between those from fixed-bed gasifiers and entrained-flow gasifiers. One exception is the TRIG gasifier. KBR offers this gasifier as a 5,000 tpd unit, which is approx. 1,000 MW of thermal input [14]. Thus, it is the largest gasifier available.

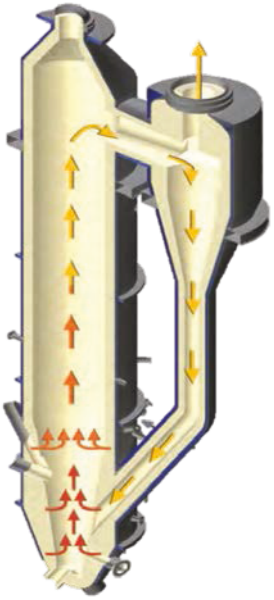

Figure 4 Example for fluidized-bed gasification - HTW gasifier, adapted from Radtke [72]

2.1.3 Entrained-Flow Gasifiers

Apart from the Lurgi FBDB® gasifier, there are only entrained-flow gasifiers with a relevant market share. Especially, in the last years, mainly entrained-flow gasifiers were chosen for new projects [1]. The advantages of entrained-flow gasifiers are a complete carbon conversion, a raw gas free of higher hydrocarbons and a very low methane content [30]. Moreover, because of the extended operating experience for entrained-flow gasifiers, the technological risk is smaller compared to gasifiers with less commercial success.

The most important advantage of entrained-flow gasifiers is the very high single unit capacity. Most vendors offer single units with a coal consumption capacity of 1,500–2,000 t/d. The Chinese OMB gasifier (developed by East China University of Science and Technology, ECUST) is currently operated on a 3,000 tons per day basis (Inner Mongolia, Rongxin, 65 bars, slurry gasifier) [17].

The required effort for coal preparation (grinding to pulverized coal) is comparably high. On the other hand, there are no coal-left-overs as discussed for fixed-bed gasifiers above. Coal is grinded to particle sizes below 0.25 mm and fed dry or as a slurry. The produced

fine coal needs to be quickly converted. Due to the shortest residence times, entrained-flow gasifiers operate at the highest temperatures to achieve complete carbon burnout. To overcome the "sticky-ash" region, entrained-flow gasifier operate 100 – 150 K above the ash-liquidus temperature (T_{25Pas}). The ash liquefies, flows downwards and is discharged at the bottom. The necessity to melt the ash and to reach the required operational temperatures is especially disadvantageous for low-quality feedstocks, such as high-ash coals. Thus, it is technically feasible to gasify high-ash coals but it has a poor thermodynamic performance [45] and questionable economics.

Figure 5 shows the GSP gasifier (Siemens gasifier) as a typical example for a dry-fed entrained-flow system. In addition to the gasifier with quench chamber and slag discharge, the coal feeding system is shown. It is comprised of a storage bunker, lock hopper system, feeding vessel (operated in a fluidized bed mode) and pneumatic conveying line to the burner.

Figure 5 Example for entrained-flow gasification - GSP gasifier, adapted from Hannemann [73]

2.1.4 Technology Development Trends

Even though coal gasification has 100 years of history and the currently available reactors have a long track of commercial operation, there is still considerably effort put in their improvement.

The main targets are to reduce investment costs and increase robustness towards higher availability [10]. As explained above, usually, the syngas is converted in a synthesis for production of chemicals and fuels. Thus, increasing the gasifier pressure is another common development trend. This is strongly connected to a fourth trend - increasing the

single unit capacity [14], [62], [74]. The aforementioned targets would improve process economics for each type of coal and product.

Other developments address applicability of low quality feedstocks (e.g. low quality coal, waste, sludge, biomass) to gasification routes. Thus, a lot of research effort is put in feedstock preparation (e.g. drying, torrefaction, milling, feeding) [75], [76], raw gas treatment (e.g. de-dusting, scrubbing, cleaning) [77] and new gasifiers [51], [54], [78], [79]. The latter, usually intends to overcome the drawbacks of fixed-bed and entrained-flow gasifiers, prohibiting utilization of low quality or "difficult" feedstocks.

It is interesting to note that most of the newly developed gasifiers apply fluidized-bed principles, rather than fixed beds or entrained beds even though the latter have much more commercial success. The reasons are two-fold: Besides a superior mixing of particles and gas, it is the practicable process temperature that is most important. As shown by Gräbner et al. [23,80] a gasification temperature of 1000 – 1100°C is favorable to maximize cold-gas-efficiency and syngas yield. Feedstock conversion at those temperatures can be realized most effectively in fluidized beds. As fluidized-bed operation is also applied for the gasifier under investigation in this work, some fundamentals of the associated hydrodynamics will be discussed in Chapter 2.2.

2.1.5 Conclusion

Coal gasification is a well established technology supplying a huge market for the production of chemicals, fuels and clean power from domestic coal. The great variety of commercially offered gasifiers can be classified into fixed-bed, fluidized-bed and entrained flow reactor. All have advantages and disadvantages in terms of thermodynamic performance, gas quality, investment costs and operation costs. Depending on the coal quality and desired product, different advantages and disadvantages will become more important. However, there is no gasifier available that can convert ash-rich coal fines into a high quality raw gas at feasible costs.

From a thermodynamic point of view, process temperatures between 1000°C and 1100°C will result in maximal cold gas efficiency and syngas yield. Thus, a fluidized-bed gasifier seems promising. If the carbon conversion in a fluidized-bed gasifier could be increased from 90-95% to 99.5%, the process would be most efficiently for converting low quality feedstocks, such as high-ash coal fines, compared to other reactors. A respective approach is introduced in Chapter 4.

2.2 Fundamentals of Fluidized-Bed Systems

Even though the very first fluidized bed was applied for coal gasification, there are many other industrial applications. Fluidized-bed processes can be found in combustion and gasification (e.g. BFB gasification, CFB combustion, plasma beds); coating and granulation (e.g. pharmaceuticals, food industry); catalytic reactors (e.g. FCC, Fischer-Tropsch synthesis,); extraction and processing of metals and minerals (e.g. drying, roasting, calcination, reduction); uranium processing (e.g. extraction, reduction, hydrofluorination); adsorption processes (e.g. flue-gas cleaning) [39,41,42]:

Owing the fact that manifold applications have been commercialized, there is a great variety in types and appearances of fluidized-beds. Thus, fluidized beds can be classified according to several features:

- gas velocities (e.g. bubbling beds, turbulent beds)
- particle properties (e.g. size, density, polydispersity)
- reactor geometry (e.g. shallow beds, spouted beds, spout-fluid beds)
- grate type and distribution of injection ports for fluidization agent (e.g. jetting beds, staged beds)

For different types of beds, different (semi-) empirical correlations have been developed to calculate key properties such as minimum fluidization velocity (u_{mf}), pressure drop (Δp), entrainment velocity (u_t), jet penetration length (l_{jet}), jet half angle (γ_{jet}), bubble size (d_b) and bubble rising velocity (u_b) and so forth. In this work, only a few bed types and a selection of their key figures will be discussed in Chapter 3.1. The choice is made according to the relevance for the new coal gasifier under investigation in this work (compare Chapter 4.1).

2.2.1 Particle Characterization

Description of a fluidized bed should start with characterizing the fluidized particles. The influence of particle shape and surface properties on fluidization behavior is very difficult to investigate and is generally thought to play a minor role. Thus, they are usually neglected in gasification and combustion in fluidized beds (exceptions can be found in fluidization of fine powders [81]). Of major importance are the size and density of the fluidized particles as well as the distribution of those two properties amongst the bulk. Several attempts have been made to classify and to predict the fluidization behavior of particles according to their size and density. Most widely used is the classification according to Geldart [82], which is applicable to gas-solid systems especially with air at room conditions. But also others have published their suggestions. Molerus [83] and Grace [84] have extended Geldard's work by the effect of particle cohesion and gas properties

at elevated temperatures and pressures, respectively. Goossens [85], has correlated Archimedes number (Ar) such that his classification is applicable for gases and liquids. However, all aforementioned classifications share the original structure proposed by Geldart. Thus, 4 groups of particles can be distinguished. Table 2 and Figure 6 summarize their characteristics [35].

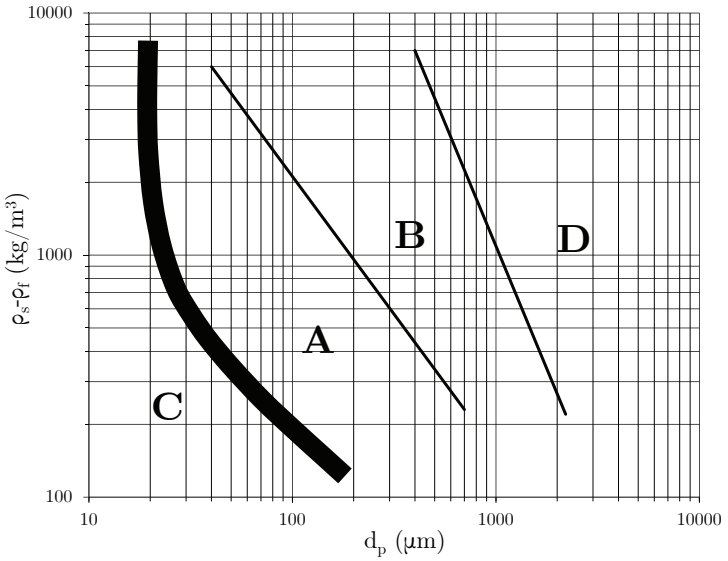

Figure 6 Geldart classification of particles

If different fluidized beds are compared to each other, it is mandatory to compare both the particles and the fluidizing agent The applied bed material in a certain experimental setup or simulation is crucible to the transfer of results and knowledge to another fluidized bed system. In Chapter 3.3, some examples and resulting limitations will be discussed.

Table 2 Geldart classification of particles [35,40]

Group	**Size (µm)**	**Density (kg/m³)**	**Comment; Examples**
A	20..100	500..2000	very well fluidizable, small bubbles; coal, coke, FCC catalyst
B	40..500	>1400	well fluidizable, coalescence forms large bubbles; sand
C	0..30	400..4500	poorly fluidizable, channeling, stirrer required; fly ash, cement, flour
D	>600	often <1400	slow and large bubbles, spoutable; ash-agglomerates, wood chips, beans

2.2.2 Types of Fluidized Beds and Key Parameters

In the following, fluidization phenomena will be explained that are based on different gas velocities, reactor geometries and the application of tuyères/nozzles.

Fluidized beds start to evolve, if the minimum fluidization velocity (u_{mf}) of the bed material was reached. The exerted drag force dominates over the sum of gravitational force and buoyancy. Thus, particles of the rigid fixed bed start to loosen and move. Particles of Geldart class A initially show a homogeneous expansion of the bed. After increasing the gas velocity to the so called minimum bubbling velocity (u_{mb}) the particles are no longer equally distributed but distinct gas bubbles emerge and rise. Thus, a bubbling-fluidized bed is developed. Particles of Geldart class B and D immediately start with bubbling behavior if u_{mf} is reached.

A further increase in superficial gas velocity leads to an increase in bed height and a decrease in the mean voidage of the bed. Thus, the effective gas velocity within the flow channels remains constant leading to a constant mean pressure drop of the bed. Whilst the pressure drop of a fixed bed is proportional to the gas velocity, it is constant for fluidized bed even for different velocities. The pressure drop equals the specific lifted bed mass (see Equation (2.1)).

$$\Delta p = \frac{m_s g}{A} \tag{2.1}$$

From this constancy, the most common measurement technique to determine u_{mf} has evolved. The procedure to determine u_{mf} from pressure drop measurements is usually done according to ASTM standard [86]. Alternative procedures apply acoustic techniques [87] or vibration-accelerator techniques [88] to identify the point of fluidization, but they have not seen too much prevalence.

However, the minimum fluidization velocity is one of the most important characteristics of a bulk material as it summarizes several properties such as size, density, or surface properties. Due to its importance, many different correlations to pre-calculate u_{mf} have been developed as summarized e.g. in Yang [89] or Farshi [90]. Most of them have the same structure. The Reynolds number (ratio between inertial and viscous forces) at the point of fluidization (Re_{mf}) is calculated from the Archimedes number (Ar; ratio between buoyancy and viscous forces) and two constants C1 and C2 that need to be determined experimentally.

$$Re_{mf} = \sqrt{C_1^{\,2} + C_2 Ar} - C_1 \tag{2.2}$$

Basis for this equation is to equate the frictional pressure gradient of a fluidized bed with the pressure drop of the fixed bed at the point of fluidization. Applying e.g. the Ergun equation [91] for this, one gets

$$-\frac{dp_f}{dz} = \frac{150 u_{mf} \nu (1-\varepsilon_{mf})}{d_p^{\,2} \varepsilon_{mf}^{\,3}} + \frac{1.75 u_{mf}}{d_p \varepsilon_{mf}^{\,3}} = \frac{(\rho_s - \rho_f) g}{\rho_f} \tag{2.3}$$

pressure gradient — frictional force of fluid through fixed bed — weight corrected by buoyancy

Rearranging and summarizing into dimensionless groups this equation results in

$$0 = Re_{mf}^{\,2} + \left(\frac{150}{1.75} 1-\varepsilon_{mf}\right) Re_{mf} - \frac{\varepsilon_{mf}^{\,3}}{1.75} Ar \tag{2.4}$$

From two solutions of this quadratic equation only one is physically realistic. The solution is already shown in Equation (2.2). Applying Ergun one gets

$$C_1 = 42.86(1-\varepsilon_{mf}) \quad \text{and} \quad C_2 = \frac{\varepsilon_{mf}^{\,3}}{1.75} \tag{2.5}$$

Table 3 summarizes some of the most common constants C1 and C2. Usually, an accuracy around ±30% is achieved for those empirical constants in conjunction with Equation (2.2) [89]. This shows that deviations up to 30% are common in calculating or simulating fluidized beds. The main reason is that empirical equations are based on a finite set of data points. Thus, materials can be found that behave differently compared to the materials considered in the sample data. On the other hand, a curve fitting over a large number of different materials results in two consequences. First, many different materials can be reflected with the empirical correlation at a certain confidence. Second, the accuracy of the prediction with respect to a distinct material vanishes.

Table 3 Constants for calculating the point of minimum fluidization

Reference	C1	C2	Comment
Ergun [91]	$42.86(1-\varepsilon_{mf})$	$\varepsilon_{mf}^3/1.75$	knowledge of voidage at point of fluidization required
Wen & Yu [92]	33.7	0.0408	widely accepted esp. for fine particles >0.5 mm
Babu [93]	25.25	0.0651	esp. for coal gasification materials
Chitester [94]	28.7	0.0494	esp. for gases at elevated pressures

Besides a large number of correlations for u_{mf}, several correlations can be found to estimate the minimum bubbling velocity (u_{mb}) [35], the minimum spouting velocity (u_{msp}) at which spouting in spouted beds starts [37], entrainment velocity (u_t) or other velocities marking the transition between different bed types (e.g. critical velocities u_k and u_c [95], compare Figure 7) as summarized in [35]. Some of those characteristic velocities will be used for validation purposes in later chapters.

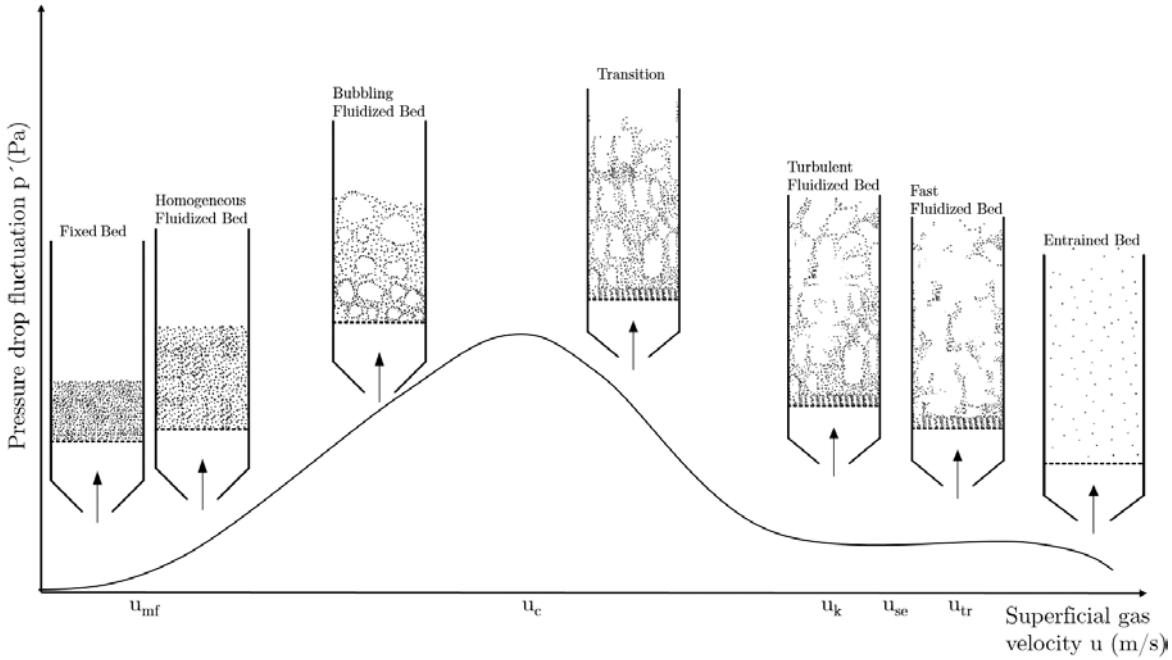

Figure 7 Bed types and pressure drop fluctuation

Above, it was explained that pressure drop measurements are applied to determine the point of incipient fluidization. In a comparable manner measurements of the pressure drop fluctuation are applied to determine the transition between different types of fluidized beds [39,40,96]. Whilst the mean value of the pressure drop is constant over different fluidization velocities, its fluctuation (p´) will change (see Figure 7). Again, this measure will be applied for validation of the numerical simulation setup (see Chapter 3.3). Given a cylindrically shaped reactor and a gas inlet at the very bottom by means of a grate or perforated plate the following bed types can be distinguished: Homogeneous fluidized beds, bubbling-, turbulent-, fast-fluidized and entrained beds, compare Kunii and Levenspiel [40] or Grace et al. [39]. The bubbling-fluidized bed is the most often applied type.

In Chapter 4, a new staged fluidized-bed gasifier will be introduced. The reactor encompasses, besides other bed types, a bubbling bed and a fast-fluidized bed. The fast-fluidized bed is of special interest as the main solids conversion occurs there. Thus, fast-bed characteristics are explained in the following.

2.2.3 Fast-Fluidized Beds

Fast-fluidized beds (or circulating-fluidized beds) are of special interest for this work as the two main reaction zones of the investigated gasifier will be a jetting bed followed by a fast-fluidized bed. Some basic information are presented in the following. Early commercial applications of fast-fluidized beds in the 60s and 70s were ahead of scientific understanding. As mentioned by Yerushalmi et al. [97] e.g. the Synthol Fischer-Tropsch syntheses at Sasolburg (South Africa) was operated under fast-bed conditions. Reh [98] has reported about two technologies invented and applied by Lurgi Chemie und Hüttentechnik GmbH – an aluminum hydroxide calcination and a hydrogen fluoride absorber, both operated as fast beds.

Fast-fluidized beds in industrial large-scale applications emerge at elevated gas velocities $u>2$ m/s (for comparison: turbulent-fluidized beds have gas velocities between 0.5 and 1.5 m/s [99]) and high solids loadings [97,100]. Thus, the fluidization number (u/u_{mf}) can be as high as 300. Cross-sectional mean solids concentration range from 0.15 in the bottom zone to 0.02 in the top region [101] (bubbling beds operate at 0.3-0.8). However, fast-fluidized beds can encounter a much larger radial gradient of solids concentration compared to bubbling beds. An important feature of fast-fluidized beds is the formation of particle clusters. Particles travel upwards in strands rather than being equally distributed over the reactor cross section. Moreover, due to the wall condition (gas velocity at the wall equals zero), particle strands can fall down close to the wall. This induces the so-called core-annulus structure with an internal recirculation and intense back-mixing of particles [100]. Strand formation is especially characteristic for Geldart A particles. Entrainment of strands requires much higher gas velocities, compared to entrainment of a single particle. Thus, fast-fluidized beds can be operated at superficial gas velocities above the terminal velocity (u_t) of a single particle from the bed material. This can be seen in Figure 15. For fine particles, there is a zone called "CFB-zone" above the entrainment line. Fast-fluidized beds (or circulating-fluidized beds) will be located in this area. In other words: at a given superficial gas velocity, strands travel upwards slower than the surrounding leaner phase [97]. The mean particle residence time and relative velocity are increased, compared to a dense or dilute transport system, which improves conversion. The resulting advantages for reactors are obvious. Still, fast beds have a uniform temperature distribution (which is a major advantage of fluidized beds in general) as particle back-mixing is intense [97]. On the other hand, back-mixing of gas is strongly reduced compared to bubbling-fluidized beds. The demarcation between turbulent bed and fast-fluidized bed is difficult to claim. Following the argumentation of Horio [96], turbulent beds are a transition regime between bubbling-fluidized beds and fast-fluidized beds. On the other hand, Bi et al. [99] argue that turbulent beds are a separate and distinct state of fluidization. However, Bi et al. [99] have summarized correlations for critical velocities demarcating turbulent beds from fast-fluidized beds (see Table 4).

Here, correlations to determine u_{tr} are based on measuring the solids entrainment behavior and correlations to determine u_{se} are based on measuring the solids concentration profile. Still, it is discussed which approach is most suitable [99,100,102]. In all cases is $u_{se} < u_{tr}$.

Table 4 Empirical Correlations for u_c, u_{tr} and u_{se}

Reference	Type of measurement	Comment	Equation
Bi and Grace [102]	Fluctuations of absolute pressure	-	$Re_c = 0.565Ar^{0.461}$ (2.6)
Leu et al. [103]	Fluctuations of absolute pressure		$Re_c = 0.568Ar^{0.578}$ (2.7)
Bi and Fan [104]	Solids entrainment behavior	widely accepted	$Re_{tr} = 2.28Ar^{0.419}$ (2.8)
Adánez et al. [105]	Solids entrainment behavior	for coal particles	$Re_{tr} = 2.078Ar^{0.458}$ (2.9)
Tsukada et al. [106]	Solids entrainment behavior	for elevated pressure	$Re_{tr} = 1.806Ar^{0.458}$ (2.10)
Bi et al. [99]	Solids concentration profile	widely accepted for	$Re_{se} = 1.53Ar^{0.5}$ (2.11)

As mentioned above, below the fast-fluidized bed a jetting bed can be found in the investigated gasifier (see Chapter 4.1). The nature of jetting beds is explained in the following.

2.2.4 Jetting-Fluidized Beds

Jetting phenomena in fluidized beds are generally discussed from two different perspectives.

a) Gas jets can be induced unintentionally or intentionally in the bottom gas entry region via the gas distributor (perforated plates, porous media, bubble caps, nozzles, spargers, pierced sheet grids, etc).

b) Larger and faster gas jets can be injected in a fluidized bed by feeding a comparable high portion of the gas through a single nozzle (horizontally or vertically). This type of jetting-fluidized bed can be found in coal gasifiers, agglomerators and granulators or dryers.

The first type of jetting is presented e.g. by Yang [89] or Karri and Werther [107]. It is widely investigated because intense mixing and high relative velocities can be found in the jetting region above the distributor. Thus, this region is important for the overall performance of a fluidized bed. It is of less importance for the present work and will not be discussed in the following. The latter type of jetting is important for this work because the gasifier under investigation has such a jetting region (compare Chapter 4.1). In the following, the terms "jetting" and "jetting-fluidized bed" refer to the latter type.

Jet properties

Jet properties in all types of jetting beds are a function of solid properties (size, density, polydispersity), gas velocity, gas density, and viscosity, solids loading, geometry and angles [108,109]. Most important key figures to characterize and compare jets are the jet half angle (γ_{jet}), the penetration depth (l_{jet}) and the jet velocity along the axis ($u_{jet,z}$). It is interesting to note that the jet velocity dissipates faster in a fluidized bed compared to a jet in a homogeneous medium by a factor of approx. 1.64 [89]. It is important to distinguish between two regions of the jet. The jet core is a short region right at the nozzle front. Its length ($l_{jet\text{-}core}$) is in the order of magnitude of the nozzle diameter. It is free of particles and is usually stable, not fluctuating and exhibits an almost constant velocity along its axis until $l_{jet\text{-}core}$ is reached. On the other hand, the remaining jet does fluctuate and flickers around under most conditions [110]. Thus, time averaging is required for evaluation of the aforementioned key characteristics. Still, there is a large discrepancy between the many proposed correlations to calculate e.g. the jet length (l_{jet}) [89]. One reason is the different possible appearances of jets and resulting different assumptions of the jet length based on visual impression. Yang [89] has summarized 3 types of jets that are discussed most often (see Figure 8). Bubbling jets (left side of Figure 8) are more likely if a) jet velocity is low, b) particles are fine and c) particles are of wide size distribution.

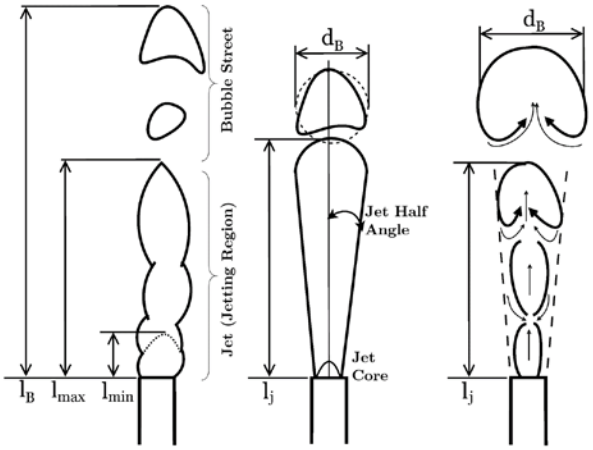

Figure 8 Types of jets in fluidized beds

Empirical correlations

Table 5 presents a few correlations to calculate the expected jet penetration length. Usually, calculated jet length based on these suggestions, deviate by ±40% compared to experimental results [111]. As already discussed in Chapter 2.2.2, the empirically derived models have comparably low accuracies because only a limited number of data have been regarded in the development. Generally, deviations from 30%-40% are possible in the prediction of the hydrodynamics in fluidized beds such as bubbling beds, fast beds, and jetting beds.

Table 5 Correlations for jet penetration length

Reference	Comment	Correlation
Yang [112]	widely accepted	$\frac{l_j}{D_0} = 6.5\left[\left(\frac{\rho_f}{\rho_s-\rho_f}\right)\left(\frac{u_{jet}^2}{gD_0}\right)\right]^{0.5}$; where $l_j = \frac{(l_{min}+l_{max})}{2}$ (2.12)
Yang [111]	for pressurized systems, C=7.65 for u=u_{cf}; else C depending on solids (varying between 1.81 and 4.21; C=2.84 for FMC char	$\frac{l_{max}}{D_0} = C\left[\frac{(u_{cf})_{atm}}{(u_{cf})_p}\left(\frac{\rho_f}{\rho_s-\rho_f}\right)\left(\frac{u_{jet}^2}{gD_0}\right)\right]^n$; where $n = 0.472$ for $u = u_{cf}$, $n = 0.835$ for $u > u_{cf}$ (2.13)
Merry [113]	widely accepted for all types of jets even though developed for vertical multiple distributor jets	$\frac{l_{max}}{D_0} = 5.2\left(\frac{\rho_f D_0}{\rho_p d_s}\right)^{0.3}\left[1.3\left(\frac{u_{jet}^2}{gD_0}\right)^{0.2} - 1\right]$ (2.14)

Comparable to Equations (2.12) and (2.13), most published correleations are based on the two-phase Froude number (Fr_{jet}) (see Equation (2.15)), which is corrected by different empirical constants and process prameters (e.g densities of gas and solid, nozzle geometry, particle size, fluidization velocity).

$$Fr_{jet} = \frac{u_{jet}^2}{gD_0}\frac{\rho_f}{(\rho_s-\rho_f)} \tag{2.15}$$

The variety of identified influencing factors and inconsistencies amongst the publications make it difficult to favor one correlation over the other and to apply them for scal-up purposes [89,110].

Less correlations have been published for the jet half angle. Again it is the proposed correlation from Merry [113] that is applied in the most cases (see Equation (2.16)).

$$\cot \gamma_{jet} = 10.4 \left(\frac{\rho_s d_s}{\rho_f D_0} \right)^{-0.3} \tag{2.16}$$

Even though corrections of the coefficients have been suggested to fit to more experimental data (e.g. Wu and Whiting [114]), Merry's correlation is still state of the art. Especially in the frequent case of fluctuating and flickering jets, the jet half angle applies for the time-averaged jet only. It is nearly impossible to find this theoretical value on a snapshot basis for the jet. Thus, jet interactions with the confining walls can hardly be discussed from this value.

Yang [89] reports that experimentally derived jet half angles over a very wide range of conditions have been found from 3.5 degree to 25 degree. It is also reported for less extreme boundary conditions that the jet half angle usually lies between 8 degree and 15 degree [110]. Jet length and jet half angle are closely connected to the jet velocity profile. Yang and Keairns [115] have shown how the velocity magnitude at the jet axis decreases over height. Moreover, it was shown, how the penetration depth (l_{jet}) increases if an increasing amount of solids are entrained in the jet. Based on their measurements the authors derived a universal velocity profile.

Universal jet velocity profile

Universal applicability of the suggested velocity profile is based on nondimensionalization of the abscissa by dividing the radial position (r) by the position ($r_{1/2}$) at which the local jet velocity is half of its maximum at the jet axis at the given height (z). The ordinate is nondimensionalized by calculating the quotient from

[jet velocity at a certain radial position ($u_{jet,z,r}$)]–[jet velocity at the jet boundary ($u_{jet,z,b}$)]

and

[jet velocity at the jet axis ($u_{jet,z,max}$)]–[jet velocity at the jet boundary].

Plotting this quotient over the nondimensional radius will give the same profile for each height (z). This is similar to the Tollmien solution for homogeneous jets into an infinite gas medium (see Figure 9). Different comparable measurements have been summarized by Yang [89]. From this summary two approaches to develop a universal velocity profile can be identified. Some authors converge there measurements into a Tollmien similarity, others into a Schlichting similarity.

For the latter, not only the velocity needs to be measured, but also the bed voidage needs to be known. Similar nondimensionalized profiles have been found also for the gas concentration profile of jets [109]. From this, it is concluded that gas mixing is primarily due to convection rather than diffusion. Moreover, it is found that gas from the emulsion phase is entrained into the jet right above the nozzle. At higher elevations, gas is released from the jet into the emulsion phase, thus the net-flux direction has changed with height. The height of the zone with a net flux into the jet is proportional to jet velocity and superficial gas velocity in the surrounding emulsion phase. Measurements on the amount of entrained gas into the jet are rare. However, Yang and Keairns [115] found that 50% of the original jet flow is entrained into the jet from the surrounding emulsion phase increasing its flow rate to 150%.

Jet penetration, jet angle and jet velocity profile will be discussed for the experimental work from Hensler et al. [116] in Chapter 6.4.1.

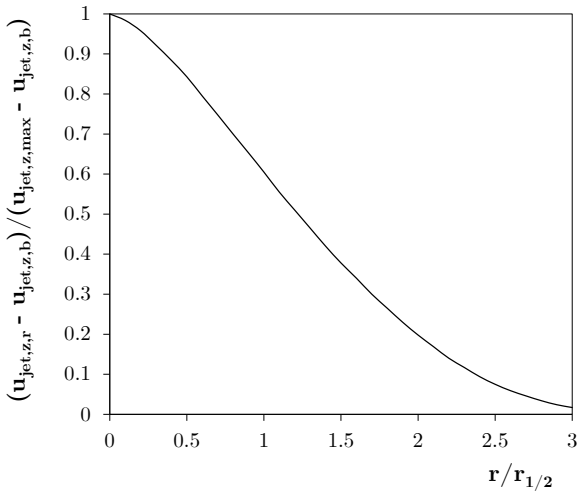

Figure 9 Universal jet velocity profile (Tollmien similarity)

Solids concentration in jetting beds

Another phenomenon, the solids mixing and circulation, is also of great importance for the gasifier under investigation. As Yang [110] has concluded, in fluidized-bed gasifiers, the solids mixing rate is in the same order of magnitude as the rates for devolatilization and fines conversion. Thus, mixing of feedstock and gasification agent becomes a controlling factor, not to say the limiting step. This is especially true for reactors with only one solids feeding point. The solids circulation pattern in jetting beds have been investigated e.g. by Yang and Hensler et al. [110,116]. It is shown that jets into fluidized beds will form a recirculation cell. This is comparable to the more frequent case of confined gas jets into a gaseous atmosphere. However, in this way a fast up-flowing, lean core and a dense, downflowing annulus is established. In between is a region of alternating flow

directions (compare Figure 10). As discussed in more detail in Chapter 4.1 for the investigated gasifier, the dense recirculation cell will protect the reactor wall from the high temperatures of the lean, flame-like, up-flowing jet.

Depending on the type of jet, the lean up-flowing core can usually be separated in the jet itself (sometimes called jetting region) and the bubble street above (compare left side of Figure 8). In the lower part of the jetting region, solids move from the surrounding emulsion phase into the jet. At a distinct height the net solids flux is from the jet to the emulsion phase [116]. For jets that develop into a bubble street, the main solid exchange occurs due to the solids-carrying capacity of the bubble wake and is a function of bubble frequency [110]. For permanent and more stable flame-like jets the solids mixing is dominated by solids entrainment into the lower region of the jet. Yang and Keairns [117] reported that the solids entrainment velocity into the jet in this lower region is proportional to jet velocity and increases with height but decreases with solids loading. In any case, the mixing of particles and gas in the jet and bubble street region is even more intense compared to spouted beds.

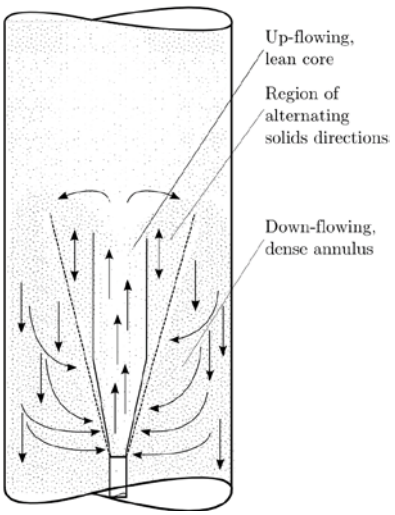

Figure 10 Solids flow pattern in jetting beds

2.2.5 Spouted Beds

All aforementioned fluidized-bed types are based on the assumption of a cylindrical vessel rather than a conical. Application of a conical reactor geometry will be introduced in Chapter 9 Outlook as a potential improvement for the investigated gasifier. A conical geometry is the typical feature of spouted beds and spout-fluid beds (see Figure 11). Thus, a short summary for this type of fluidized-bed is given below. An extended introduction is given elsewhere [37,118,119]. In contrast to conventional spouted beds, spout-fluid beds feature a secondary gas inlet into the annulus region. This is designated to reduce agglomeration tendencies, dead zones and adhesion to the wall, which is reported for conventional spouted beds [120]. The secondary gas inlet usually provides a base

fluidization of the bed material. Thus, it also called "background gas", which is introduced with a velocity of u_{bg}.

Spouted beds are applied e.g. for [37]:

- drying of agricultural granules
- drying of pastes or suspensions in spouted beds of inert solids
- solids blending
- coating, granulation
- gasification

They consist of a conical reactor or at least a conical bottom part of a cylindrical reactor. The spouting gas is injected centrally at the bottom through a small opening. If the superficial gas velocity is at least as high as the minimum spouting velocity (u_{msp}), the spouting phenomenon occurs. Comparable to the minimum fluidization velocity (u_{mf}), u_{msp} is a characteristic value for the applied bulk material and the given gas properties (density, viscosity). If a spouting bed is established, a lean and fast central gas jet (the spout) penetrates through the bed material. Compared to a jetting-fluidized bed, the spout velocity is one order of magnitude lower. Entrained particles leave this spout-jet at a height above the surrounding bed level in a fountain-like fashion (see Figure 12).

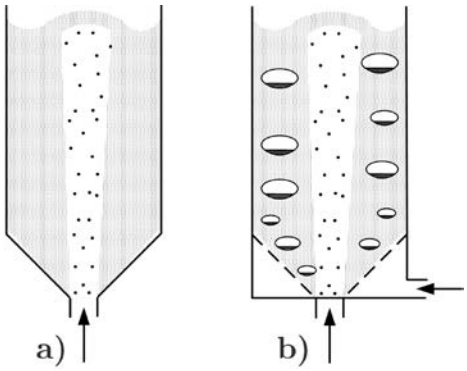

Figure 11 Spouted bed (a) and Spout-fluid bed (b)

The voidage in the fountain is smaller compared to the lean spout, whilst the voidage in the annulus is approx. that of a fixed bed. Thus, there are three distinct zones that differ at least in the effective gas velocity, particle velocity, and voidage. Whilst the particles in the lean spout are entrained upwards, they change their flow direction within the fountain and travel downwards in the annulus. After the particles reached the bottom, they are directed into the jet and are entrained again. Thus, a pronounced solids-recirculation is established. In the jet, gas and particles are in co-current flow, whilst the annulus exhibits a counter-current flow.

In spouted beds, particle erosion is low compared to conventional fluidized beds, as the particle motion is more directed and relative particle velocities are lower [37].

By far, the most spouted beds apply particles of Geldard class D. In fact, both Epstein et al. [37] and Mathur et al. [118] reported that the required minimum particle size for spouting is 1 mm. Mathur et al. indicated that spouting for finer solids is possible only on a lab scale. Sahoo et al. [121] summarized options to fluidize fines in spouted beds. They suggested to employ stirrers, field forces (magnetic, acoustic) or vibrational beds. Altzibar et al. [122] investigated how spouted-bed fluidization of fines is improved if special open-sided draft tubes are applied.

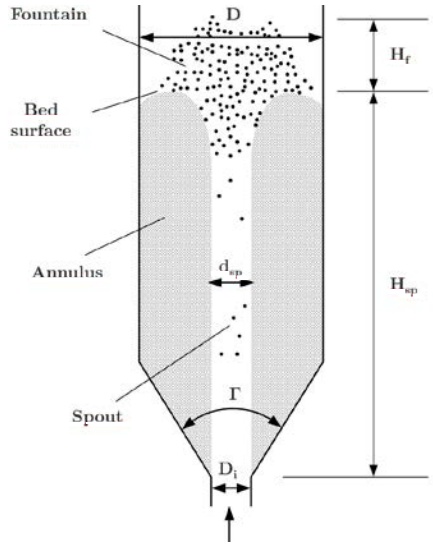

Figure 12 Details of spouted beds

Thus, the suggested improvement of the investigated gasifier, to apply a conical section in the middle of the reactor (compare Chapter 9 Outlook), will not necessarily result in a classical spouted-bed behavior as the particles are much smaller than 1 mm. For this reason, it is superfluous to derive and discuss key figures of spouted beds such as spout diameter, maximum spoutable bed height, pressure gradients or voidage distribution. Nevertheless, at least two empirical correlations for the minimum spouting velocity (u_{msp}) are shown in Table 6 for the sake of completeness.

Table 6 Empirical correlations for minimum spouting velocity

Reference	Comment	Equation
Mathur and Gishler [123]	widely accepted for cylindrical vessels of D<0.5 m	$u_{msp} = \left(\frac{d_p}{D}\right)\left(\frac{D_i}{D}\right)^{\frac{1}{3}}\left(\frac{2gH_{sp}(\rho_s-\rho_f)}{\rho_f}\right)^{0.5}$ (2.17)
King and Harrison [124]	modified version of Eq. (2.17) for elevated pressure	$u_{msp} = \left(\frac{\rho_f}{\rho_{air(p=1atm)}}\right)\left(\frac{d_p}{D}\right)\left(\frac{D_i}{D}\right)^{\frac{1}{3}}\left(\frac{2gH_{sp}(\rho_s-\rho_f)}{\rho_f}\right)^{0.5}$ (2.18)

The above introduction of fluidized beds and some special types of beds was conducted on a more generalistic level. In the subsequent chapter, tools will be introduced a) to evaluate which type of bed is most likely present in a certain experimental setup and b) to investigate the bed behavior on a computational basis.

2.2.6 Conclusion

There is a great variety of fluidized-bed types because there is an even greater variety in applications. Thus, different parameters are applied to characterize the fluidized bed and different key performance indicators are used to describe the success of the fluidized-bed operation. In addition, different (semi)-empirical correlations have been developed to calculate required input flows and expectable hydrodynamics. Moreover, the applied solids are characterized by size, density and Geldart class to estimate the fluidization behavior. The minimum fluidization velocity of a bulk material is another key measure. Different empirical correlations were suggested to calculate this value. Other frequently applied measures are the pressure drop and its fluctuation as well as the mean voidage and radial or axial profiles of the voidage or velocity profiles. Those measures will be used for validation of simulation setups in Chapter 6.3

The most common bed types are bubbling beds, turbulent beds and fast beds. The demarcation between them is defined by means of pressure drop fluctuation and characteristic velocities. Fast beds are characterized by a distinct core-annulus structure and the formation of particle strands and clusters.

Another group of fluidized beds are jetting beds and spouted beds. The demarcation between those two systems is depended on the Froude number. In addition to the aforementioned measures, jetting beds are described by different jet properties (jet-core length, jet length, jet half angle) as well as velocity and voidage profiles along the jet. Empirical correlations have been developed also for these measures. Those measures will be used for validation of simulation setups in Chapter 6.4.

The accuracy at which the different measures of the different bed types can be calculated with the different empirical equations is not very high. Deviations of up to 30–40% are common.

3 Approaches to Assess Fluidized Beds

Besides experimental investigations to assess the hydrodynamics of fluidized beds (which are summarized elsewhere [125–130]), modeling and simulation are meaningful tools to better understand a certain fluidized-bed application. Also, the scaling of fluidized-bed gasifiers is usually done by means of dimensionless groups and simulations [131–134]. The following chapter introduces options to assess fluidized-bed hydrodynamics by

a) zero-dimensional (0D) approaches such as dimensionless groups and their visualization in regime maps as
   → see Chapter 3.1 Empirical Simulation
b) 1D approaches assessing bed properties over the reactor height
   → see Chapter 3.2 Simulation with ASPEN Plus®
c) 2D and 3D approaches, such as CFD to investigate axial and radial property profiles and the transient behavior of fluidized beds.
   → see Chapter 3.3 CFD Simulation

The first approach is as mature as commercial fluidized-bed operation itself. It is a daily engineering tool with a comparable quick and easy setup, given that all required input data are available. The 1D approach usually requires a software packages and thus a "trained" user. However, it is much less complex compared to the third approach and can be found in daily commercial application, too. The last approach is a rather scientific tool. Nevertheless, CFD simulations of reacting multiphase flows become more and more viable, also in a commercial environment.

3.1 Empirical Simulation

In this thesis, empirical simulation refers to application of zero-dimensional modeling and simulation tools. In the most cases, the approaches are very simple. In this way, a first description and categorization of the hydrodynamics in a certain reactor can be accomplished. This can be done without computer assistance.

3.1.1 Nondimensional groups

As already introduced in Chapter 2.2.2, dimensionless groups are applied to describe fluidized beds as well as to calculate their key parameters. For the most applications, a set of four dimensionless quantities and combinations of those is enough to describe the hydrodynamics: Archimedes number (Ar=buoyancy force/internal viscous force),

Beranek number (Be=inertial force/buoyancy force), two-phase Froude number (Fr=inertial force/gravity force) which sometimes is corrected by buoyancy and Reynolds number (Re=inertial force/ internal viscous force).

$$\mathrm{Ar} = \frac{d_p^3 g}{\upsilon^2} \frac{\left(\rho_s - \rho_f\right)}{\rho_f} \tag{3.1}$$

$$\mathrm{Be} = \frac{u^3}{g\upsilon} \frac{\rho_f}{\left(\rho_s - \rho_f\right)} \tag{3.2}$$

$$\mathrm{Fr} = \frac{u^2}{g d_p} \frac{\rho_f}{\left(\rho_s - \rho_f\right)} \tag{3.3}$$

Please note that some authors would call Equation (3.3), the quadratic two-phase Froude number.

$$\mathrm{Re} = \frac{u d_p}{\nu} \tag{3.4}$$

If transfer of heat and mass, chemical reactions or the boundary layer around single particles need to be considered, an additional set of dimensionless quantities is required. This includes at least Lewis number (Le), Nusselt number (Nu), Prandtl number (Pr), Sherwood number (Sh), and Stokes number (St).

Dimensionless groups can easily be used to distinguish between or anticipate different types of fluidized beds. As early as 1948, Wilhelm and Kwauk [135], applied the Froude number to distinguish between aggregative and particulate fluidization. For $\mathrm{Fr} < 0.13$, particulate fluidization is likely. On the other hand, Doichev et al. [136] applied a corrected Archimedes number to anticipate whether fluidization will be of aggregative or particulate nature. A Froude number is also applied to estimate the jet penetration depth in jetting-fluidized beds (compare Table 5 and Equation(2.15)). Another example are the suggested correlation from Table 3 in conjunction with Equation (2.2). Based on the Reynolds number, it is possible to identify whether a bulk will be fluidized under certain conditions. In addition, calculation of the critical velocities u_{tr} and u_{se} is based on the Reynolds number (compare Table 4). From this, it is evident how dimensionless groups can help to easily categorize the type of bed. Even more meaningful is the application of several dimensionless groups in order to develop x-y-plots as operational regime diagrams.

Many examples of flow-regime diagrams have been developed since 1949 [137]. In his pioneering work, Zenz fluidized four materials (rape seeds, sand, salt, glass beads) in order to examine different types of fluidized beds. In his regime diagram he distinguished between dense beds, turbulent beds, slugging beds and entrained beds. However, he did

not apply dimensionless groups. His plot is based on the pressure drop gradient over superficial gas velocity. In some later regime diagrams, nondimensionalization of the axes was conducted by applying normalized velocities, diameters or loadings. An example is the widely applied flow regime diagram from Grace [84] (see Figure 13).

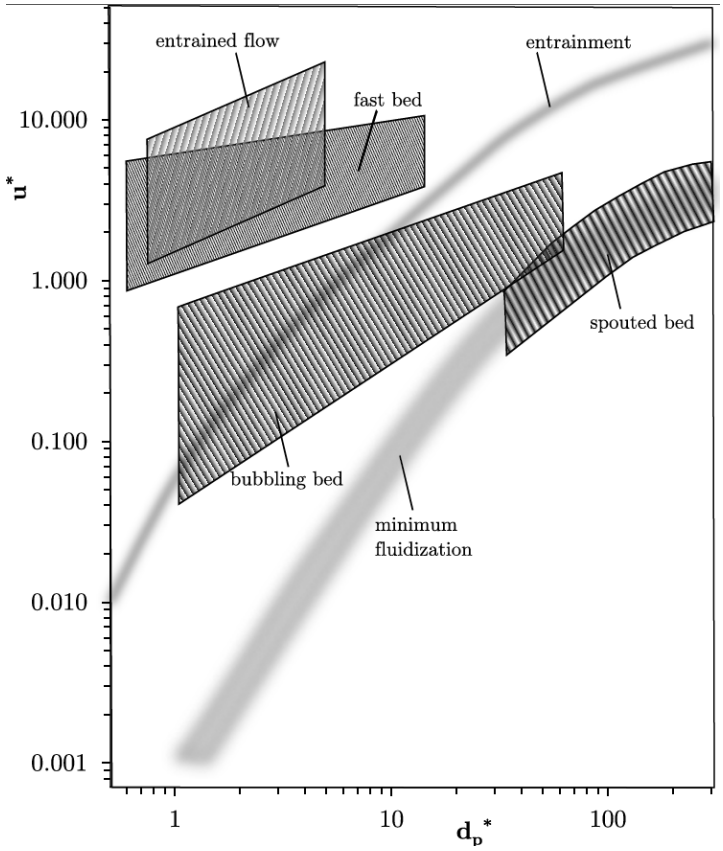

Figure 13 Flow regime diagram according to Grace [84]

For the ordinate, the normalized velocity is according to Equation (3.5). For the abscissa, the normalized diameter is according to Equation (3.6).

$$u^* = \frac{Re}{Ar^{1/3}} \tag{3.5}$$

$$d_p^* = Ar^{1/3} \tag{3.6}$$

Provision of the demarcation lines given by u_{mf} and u_t in Figure 13 is a first meaningful tool to decide whether operational conditions will result in a fixed bed, fluidized bed or entrained bed. In addition, three types of fluidized beds can be distinguished in Grace´ diagram: bubbling bed, fast bed and spouted bed. Later Bi and Grace [138] have extended this diagram by introducing u_c and u_{se}. Thus, in addition to the aforementioned types of beds, the turbulent bed can be seen in the updated version of the diagram. Chen [101] simplified the visualization of data given from Kunii [40] and Bi and Grace [138] in his

diagram (see Figure 14). Here, only two types of beds are distinguished. However, his diagram allows for a very quick distinction between bubbling and fast beds.

Chen defines d^* at the abscissa according to Equation (3.6). On the other hand, his ordinate uses another definition for the normalized velocity u^{**}, see Equation (3.7).

$$u^{**} = \frac{u - u_{mf}}{u_t - u_{mf}} \tag{3.7}$$

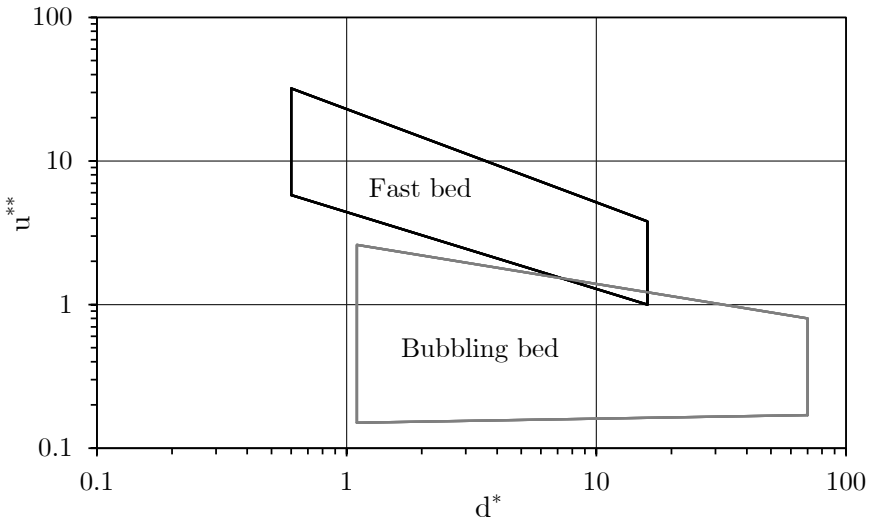

Figure 14 Regime diagram according to Chen [101]

Another approach was developed even earlier by Reh [24]. He also used Re and Ar to provide nondimensional axes for his plot (see Figure 15). In addition, he plotted auxiliary lines of constant Be and Ar in his diagram. They assist in the assessment of the direction in which an operational point will move if operation conditions or particle properties change. Other auxiliary lines in the Reh diagram show the bed voidage of a certain operational point. A more extended introduction of the Reh diagram and its application in industry is given in Gräbner [10] and Michel [139].

Comparable to the diagram by Grace, characteristic lines for minimum fluidization and single particle entrainment assist in a first evaluation whether a system will be a fixed bed, fluidized bed, or entrained bed. The left-sided zone between entrainment of single particles and strand entrainment is of special interest for the present work. As already discussed in Chapter 2.2.3, fines tend to travel in strands or clusters rather than isolated from each other. Reh applied the correlation from Martin for the single particle entrainment line. Martins approach is valid only for cases where the boundary layer around a particle does not interact with that of another particle. Thus, it cannot be applied to strands. To reflect that, Reh introduced an additional fluidization zone, called “CFB” in Figure 15.

In the "CFB" area, fines have already reached their single particle entrainment velocity but will not be entrained as they share the exerted drag force with other particles in the strand. Thus, the gas needs to exert an additional drag force to entrain a strand of particles compared to the required force for each individual particle. According to Reh's experiments, strands will be entrained if $3Re^2/4Ar$ approaches unity. For Re>100, the aforementioned quotient needs to be greater than one. For this situation, the correlation from Martin will be applied. Besides incorporation of the strands entrainment line, there are two other differences to the diagram from Grace.

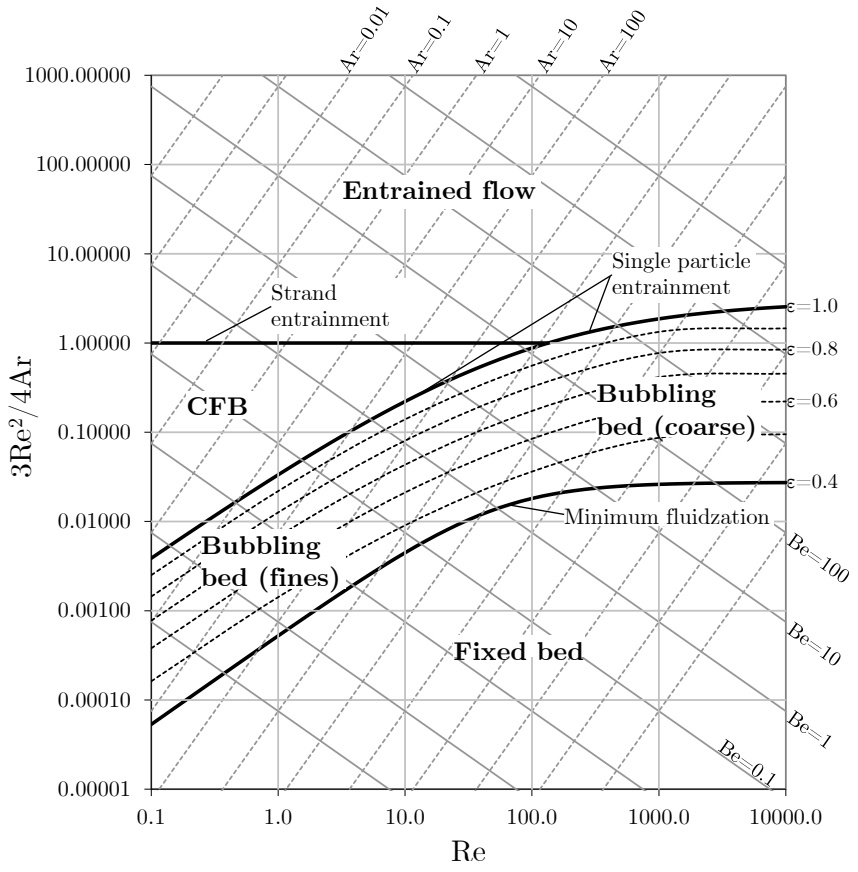

Figure 15 Flow regime diagram according to Reh [24]

The auxiliary lines (Ar, Be) in the Reh diagram are very useful to compare operational points (see Chapter 5.2 and 6.3.1). Reh´s abscissa is a function of particle size and superficial gas velocity. Grace abscissa is a function of Ar only and thus not a function of the gas velocity. This is rather unusual for such types of regime diagrams. Kunii and Levenspiel [40] have summarized the applied dimensional and nondimensional variables for the abscissa and ordinate for 11 different suggested flow regime maps. An excerpt is given in Table 7.

Table 7 Regime diagrams for fluidized beds; adapted from Kunii and Levenspiel [40]

Author	Year published	Abscissa	Ordinate
Grace [84]	1986	d_p^*	u^*
Horio	1986	Re_p	Ar
Li and Kwauk	1980	u	ε
Reh [24]	1961	Re_p	$3Re^2/4Ar$
Zenz [137]	1949	log(Δp/h)	log(u)

Figure 16 shows how the Reh diagram can be applied to discuss and compare different fluidized-bed reactors. The position of the operational point of different gasification technologies helps to identify e.g. which empirical correlation is most suitable to calculate performance characteristics such as voidage profiles or heat exchange coefficients. Figure 16 contains data from Gräbner [10] and Michel [139].

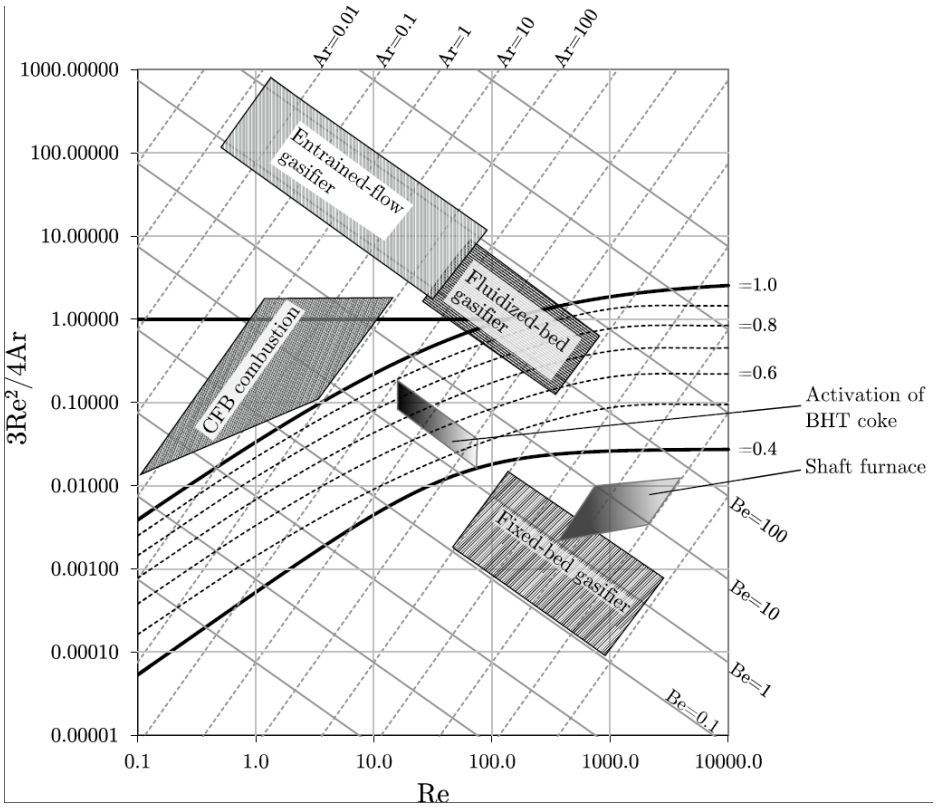

Figure 16 Operational areas for different technologies, contains data from Gräbner and Michel [10,139]

The regime diagrams mentioned so far allow for the distinction between fixed beds, bubbling-fluidized beds, turbulent beds, circulating-fluidized beds, and entrained beds. Jetting and spouting phenomena cannot be reflected in these diagrams.

A first example for a regime diagram designated to spouted beds is presented in Epstein and Grace [37]. Figure 17 shows their experimentally derived regime map for wheat spheroids (3.2x6.4 mm; ρ_s=1376 kg/m^3).

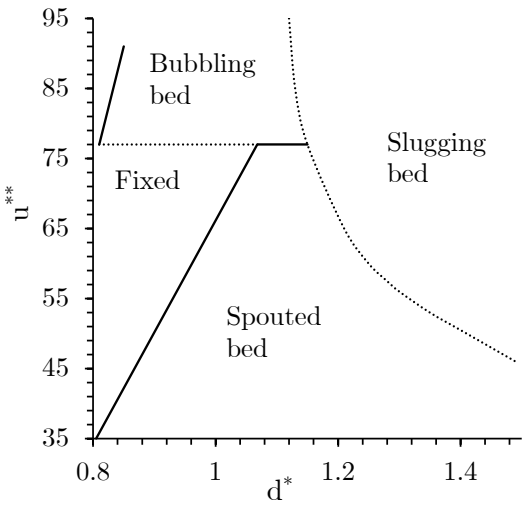

Figure 17 Regime diagram for a Geldart D spouted bed, adapted from Epstein and Grace [37]

As dimensional properties are applied for the axes, this diagram can hardly be transferred to any other boundary conditions. Comparable plots are summarized elsewhere [118]. To the authors best knowledge there is no such generalized and nondimensional diagram for spouted beds as there is for fluidized beds (e.g. Reh diagram). In the recent literature [120,140,141], the flow rates (or velocities) of spouting gas and base fluidization gas (for spout-fluid-beds) are used for the axes.

If those values are nondimensionalized by the minimum fluidization flow rate, a regime diagram can be developed as shown by Sutkar et al. [142]. However, this diagram is only a summary of possible spouted bed types rather than a tool to identify operational points. A comparable situation can be found for regime maps of jetting beds. As both, spouted beds and jetting beds have seen less scientific attention compared to conventional fluidized beds, the development of generalized and nondimensional flow regime diagrams lacks behind. Approaches with limited transferability to other systems are presented in Guo et al. [143].

Figure 18 shows the demarcation between spouting and jetting for a Geldart D bulk material. The ordinate shows the quotient of static bed height (H_0) and hydraulic nozzle diameter ($D_{0,hydr}$), whilst the abscissa shows a two-phase jet Froude number (Fr_{jet}) corrected by nozzle diameter D_0 and particle diameter (d_p).

Another diagram to distinguish spouted beds from jetting beds is given in Link et al [144]. Even though it is valid only for the conducted experiments, it will provide a very good first idea of the type of bed that has to be expected for other boundary conditions. Figure 19 shows the respective plot. The quotient applied at the ordinate is based on the

spout gas velocity (u_{sp}) and the minimum fluidization velocity (u_{mf}). The quotient applied at the abscissa is based on the background gas velocity (u_{bg}, see Chapter 2.2.5) and the minimum fluidization velocity (u_{mf}).

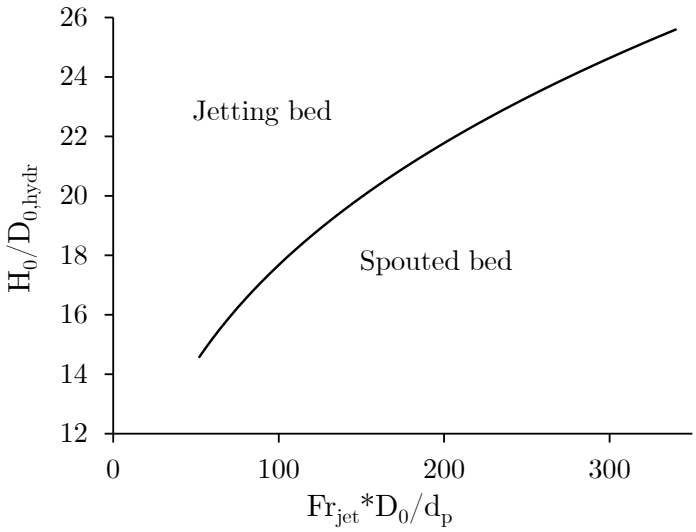

Figure 18 Demarcation between spouted bed and jetting bed, adapted from Guo et al. [143]

It is interesting to note for their experiments that the reactor size and applied material did not allow for a conventional fluidized bed. For spouting velocity being zero, and a fluidization number being unity ($u_{bg}/u_{mf} = 1$), one would expect the onset of fluidization and a fluidized bed for increasing background gas velocities. However, the experimental setup provoked a slugging bed, rather than a fluidized bed.

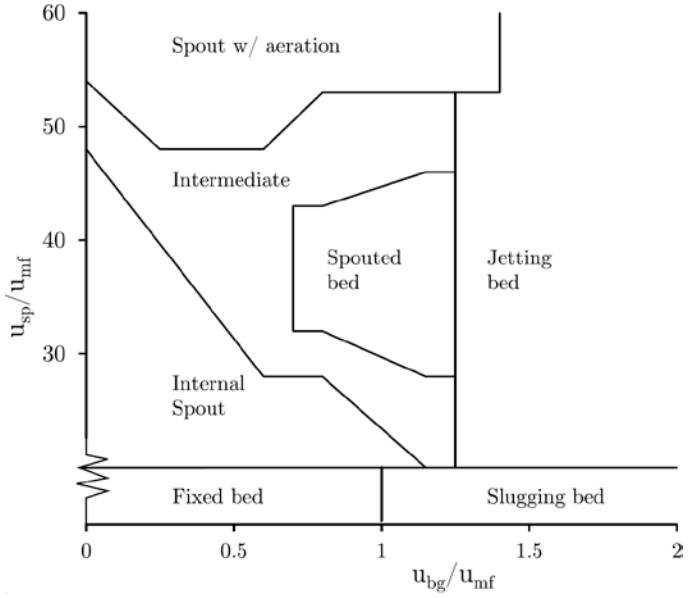

Figure 19 Regime diagram according to Link et al.[144]

3.1.2 Conclusion

It was found that several approaches have been published to identify the demarcation of different types of fluidized beds by means of dimensionless groups. In addition, visualization of different bed types in regime diagrams was discussed. Much more diagrams have been developed for conventional fluidized beds (e.g. bubbling, turbulent, circulating, ...) compared to spouted beds and jetting beds. The regime maps from Grace [84] and Reh [24] are especially suitable to a) visualize operational areas for a certain fluidized-bed application (also a priori) and b) distinguish bubbling beds from circulating/fast beds. The retrieved results from such a diagram are always of 0D nature. Thus, these diagrams are not capable to capture axial or radial profiles of e.g. the bed voidage.

A generally applicable regime diagram for spouted beds and jetting beds over a wide range of boundary conditions is missing.

3.2 Simulation with ASPEN Plus®

A few commercial tools and much more in-house developments are applied to conduct one dimensional simulations of the hydrodynamics and potentially chemical reactions in fluidized beds. Those tools are usually based on empirical correlations such as introduced in Chapter 2.2. The results from those calculations are manifold (e.g. bed height, axial profiles of voidage and velocity, voidage in the gas distributor region, particle entrainment, transport disengagement height, pressure drop, minimum fluidization velocity, bubble diameter, bubble rise velocity). In a second step those information are used to calculate residence times, progress of physical and chemical conversion and so forth. Depending on the software package, this second step of calculations can be done within the same tool or in an external tool. An example of the first type would be the software package ASPEN Plus®. An example for the latter type would be ERGUN Fluidization Software tool distributed by Uteam-Divergent S.A. In this chapter, only ASPEN Plus® is introduced.

Aspentec enhanced its widely applied software package by a solids modeling environment in 2012, after acquisition of SolidSim Engineering GmbH in the same year [145]. Usually, ASPEN Plus® is used for thermodynamic evaluation of different types of reactors such as gasifiers, gas cleaning units and many others. This common application of ASPEN Plus® was also used to investigate the present gasifier as shown in Laugwitz et al. [2] and Gräbner et al. [23]. In their work, the applied approach was zero-dimensional and balances for mass, species and energy were solved. The calculated thermodynamical equilibrium was adjusted to the expected non-equilibrium conditions by approach temperatures. In the work from Laugwitz et al. [2] and Gräbner et al. [23], the potential industrial scale unit of the investigated gasifier was shown to be superior to competing gasifiers in terms of cold gas efficiency and syngas yield especially for high-ash coals.

Several publication can be found that show how the hydrodynamics are incorporated in thermodynamical simulations in ASPEN Plus ® [146–149]. Nevertheless, these authors still use external Fortran routines to link their set of equations for the hydrodynamics to the thermodynamic properties of ASPEN Plus®. The current chapter is not designated to thermodynamical calculations but to hydrodynamic simulations within ASPEN Plus®.

Some aspects of the ASPEN Plus software package will be highlighted in the following. An extended introduction is provided in the documentation of the software package [150]. The widely accepted materials properties database and superior models for mixture properties allow for an accurate estimation of gas properties (e.g. density and viscosity) for mixtures at high temperatures and pressures. These values are crucial to predict hydrodynamic figures based on empirical equations (see Chapter 2.2).

The implemented hydrodynamic model in ASPEN Plus® is based on the Two-Phase Theory. It is assumed that the bed can be divided into an emulsion phase containing all the solids and a bubble phase containing only gas bubbles [35]. The basic idea is that a certain amount of gas is required for minimum fluidization conditions. Any surplus gas will rise as solids-free bubble through the bed. The emulsion phase remains at the state of incipient fluidization regardless the total gas flow through the bed. Thus, the emulsion phase has always a voidage of ε_{mf}. The bubbles capture a volume of ε_{b}. Some approaches allow the emulsion phase to have a different voidage than ε_{mf} by empirical correction factors [35]. The results from the ASPEN Plus® simulation approach include axial voidage profiles. Those can be compared to experimental results, CFD results or results from the evaluation of the Reh diagram (see Chapter 7).

3.3 CFD Simulation

Numerical simulation of gas-solid-flows in the methods applied today, trace back to the 1960´s and ´70´s when the theoretical basis was developed [151–153]. First applications for fluidized beds were published in the 1980´s [154–156]. Since then different simulation approaches have been developed. Still, the modeling is in its infancy and depending on the investigated type of fluidized bed and evaluated measures deviations above 30% between simulation and experiment are common [157]. Both Syamlal [157] and Gidaspow [158] agree that the trends predicted by simulations are more useful than the absolute values of various quantities. On remarkable example for this is the work from Sinclair and Jackson [159]. They have shown under which conditions formation of strands and particle clusters occur in riser gas-solid flows. This phenomenon of particle segregation has been only assumed so far from experimental indicators. Experimental work was far from proving and understanding this behavior. The simulations from Sinclair and Jackson were a break through in understanding riser flows better. At this stage, it was not necessary to accurately predict the size of a cluster or its fluctuating velocity (quantative values). To show the pure existence under different flow conditions (qualitative values) was enough to improve reactor design in the future.

3.3.1 Modelling Approaches for Numerical Simulation of Fluidized Beds

Van der Hoef et al. [153] attempted to classify modeling approaches according to the treatment of continuous phase and dispersed phase (see Table 8). In Table 8, “Lagrange” means, a parcel (e.g. particle or discrete gas entity) is followed over time and space. The parcel obeys Newton´s laws of motion. On the other hand, “Eulerian” is to consider the phase (gas or solid) as a continuum governed by Navier-Stokes equations in a fixed-in-space coordinate system.

However, some approaches cannot be categorized in such a way. For example, Klimanek et al. [160] applied a Multi-Phase Particle-In-Cell (MP-PIC) method (which is called Dense DPM - DDPM in the applied ANSYS Fluent software) to calculate a fluidized-bed gasifier. This approach falls in between Unresolved DPM and TFM. Nevertheless, van der Hoef’s classification is used here to explain advantages and disadvantages of the different approaches. From this, the applied method in Chapter 6 is derived.

The two approaches employing Lagrangian treatment of the gas phase are not further discussed. The Molecular Dynamic approach is seldom applied for investigation of particle-particle and gas-particle interaction in fluidized beds. The LBM approach is focused on investigation of bubble behavior in bubbling beds, which is not the focus of this work. As explained by Deen [161] and Dufty & Baskaran [162], the Resolved DPM approach is applied to derive closure terms that can be transferred to larger scale simulations, such as Unresolved DPM or even TFM. Today, it is not feasible to calculate a lab-scale or

large-scale fluidized bed with that approach. The unresolved DPM can be applied to small scale units to investigate more scientific questions rather than engineering ones.

Table 8 Approaches to calculate gas-solid-flow, adapted from van der Hoef [153]

Model	Gas Phase	Solids Phase	Phase Coupling	Comment / Investigated Scales
Molecular Dynamics	L	L	Elastic collisions at particle surface	Applied if thermal fluctuations of gas-phase molecules effect solids movements (not the case in fluidized-beds) / $<10^{-3}$ m
Resolved DPM	E	L	BC at resolved particle surface	Eulerian grid size is small compared to particle size; gas and particle see particle with finite volume; low modeling effort for gas-particle interaction; also know as DNS / 0.01 m
Unres. DPM	E	L	Drag closure between gas and particle	Eulerian grid size is large compared to particle size; gas sees particle as point source and sink; particle sees particle with a finite volume / 0.1 m
TFM	E	E	Drag closure between gas and solids	Concept of interpenetrating continua; applied in the present work / 1 m
DBM	L	E	Drag closure for bubbles	Discrete gas bubbles can shrink, grow, coalesce, break-up; E phase is not only for solids but for suspension phase surrounding the bubbles / 10 m

DPM – Discrete Particle Model; TFM – Two Fluid Model; DBM – Discrete Bubble Model; L – Lagrange; E – Euler; BC – Boundary Condition

The main advantage of a Lagrangian particle treatment in the two DPM approaches is that each parcel can have its own initial and time-dependent properties. Thus, polydispersity can be reflected. Moreover, individual tracking of parcels is possible over time and space. Thus, phenomena such as mixing, residence time distribution and individual progress in e.g. chemical reaction can be evaluated. The drawback is the unfeasibly high computational costs for systems with a lot of particles and particle-particle interaction (such as fluidized beds). This results in a limitation of feasible spatial and temporal extend of fluidized-bed simulations (see 5th column in Table 8).

Most bench-scale and industrial-scale fluidized beds are calculated according to a TFM approach [162].

3.3.2 Two Fluid Model (TFM)

The pioneering work from Ishii [152] and Ishii & Mishima [163] provided the basis for TFM models. However, their models are valid for fluid-fluid systems only. Balzer et al. [164] extended the early formulations that were based on kinetic gas theory to describe pure particle systems to gas-particle flow systems [154]. From that, different formulations of gas-solid TFM were developed. Summaries are given elsewhere [36,154,165,166].

In any case, in the TFM all defined phases are treated as interpenetrating continua described by Navier-Stokes equations. The comparably low computational effort of TFM allows for incorporation of e.g. chemical reactions into the lab-scale and large-scale simulations. Nevertheless, there is a larger modelling effort required compared to DPM, which is one of the main disadvantages. The other disadvantage is that all particulate matter is merged into a single continuous phase. With this, all information about an individual particle are neglected. Thus, e.g. polydispersity can hardly be considered. Each required particle size would need an own continuous phase. A drastically increase in computational time is to be expected. In addition, evaluation of simulation results cannot be based on single particle information. Particle mixing, residence time distribution, distribution of conversion progress or other single-particle-related information cannot be evaluated.

During the development of a two fluid model several steps need to be done stepwise as visualized by Enwald [154]. One of them is the averaging of local instantaneous equations for balances of mass, momentum, energy and species. This allows coarser grids and longer time steps for simulation [154]. However, averaging introduces more unknown than number of equations. Thus, closure laws need to be applied, which usually employ empirical expressions and are often dependent on experimental findings.

The three types of closure laws (topological, constitutive, transfer) are discussed elsewhere [36,154]. Usually, a fluid-solid drag relation (K_d) and equations for the solids phase stress (τ_s) are introduced for closure. The latter is usually based on solids pressure (p_s) as well as shear viscosity (μ_s) and bulk viscosity (λ_s). Until the mid 1990th an empirical derived viscosity was used and kept constant [153]. Here, the bulk viscosity was set to zero in the most cases because reliable measurements were missing [154]. This approach is known as the Constant Viscosity Model (CVM) [156]. In the 1990´s the CVM was successfully displaced by the kinetic theory of granular flow (KTGF). Today, KTGF is state-of-the-art in TFM fluidized-bed modeling [153]. Whilst the KTGF is applied to especially describe the solids phase stress (τ_s) and solids-solids momentum exchange (K_{ds}), still the interaction between gas and solid needs to be captured. The coupling between gas phase and solids phase is usually realized by means of a momentum exchange coefficient (K_d) which depends on the drag function (C_d).

Momentum exchange (K_d)

The momentum conservation of solid phase and gas phase are connected via K_d, which accounts for momentum transfer between the phases. Several mechanisms can cause an interaction force [157]:

- Drag caused by velocity difference
- Buoyancy (lift) caused by fluid pressure gradients
- Saffman force caused by fluid velocity gradients
- Virtual mass force caused by boundary layer effects resulting from relative acceleration
- Basset force caused by prolonged development of a boundary layer resulting from relative acceleration
- Magnus force caused by particle spin
- Other forces caused by relative acceleration or gradients in temperature or pressure

A concluding remark on the nature of momentum exchange is derived from the explanations by Syamlal [157] on reacting flows. In this situation, mass transfer (e.g. gas production from heterogeneous reactions) can also cause momentum transfer. It is usually assumed that gases leaving a particle, issue as jets uniformly in all directions. The result is a net-zero force on the particles.

In the cases present in Chapter 6, only the drag force is considered, as it is by far the most dominant one in the present systems [157]. Thus, the momentum exchange coefficient equals the drag coefficient. Here, different formulations of the drag force (Equation (3.8)) differ only in the applied drag function (C_D).

$$K_d = \frac{3}{4} C_D \frac{\varepsilon \rho_g \varepsilon_s}{d_p} \Delta u \tag{3.8}$$

Types of gas-solid drag function (C_D)

Several correlations for the drag function (C_D) in Equation (3.8) have been suggested as summarized by Yates [167], Lundberg [168] and Prabhansu [169]. Usually, the gas-solid drag is investigated for single particles. It is necessary to correct empirically derived values from single particle investigations to account for multi-particle systems. Two types can be distinguished leading to two slightly different final formulations for K_d. Some approaches apply a drag function being a function of the local voidage (ε) to account for multi-particle effects (e.g. the Wen and Yu model [92]), see Equation (3.9).

$$C_D = \frac{24}{Re_s \varepsilon} \left[1 + 0.15 \left(Re_s \varepsilon \right)^{0.687} \right] \tag{3.9}$$

For this cases, Equation (3.8) will be corrected by the voidage giving Equation (3.10) for application of the Wen & Yu model. The Wen & Yu model is valid for dilute systems of $\varepsilon > 0.8$.

$$K_d = \frac{3}{4} C_D \frac{\varepsilon \rho_g \varepsilon_s}{d_p} \Delta u \varepsilon^{-2.56} \tag{3.10}$$

For dense systems ($\varepsilon < 0.8$), often the Ergun expression [91] is applied, Equation (3.11)

$$K_d = 150 \frac{(1-\varepsilon)\varepsilon_s \nu}{\varepsilon d_p^2} + 1.75 \frac{\Delta u \varepsilon_s \rho}{d} \tag{3.11}$$

A famous combination of the Wen & Yu model and the Ergun expression is known as Gidaspow model [170].

The alternative are drag functions being a function of relative settling velocities ($u_{t,rel}$) to account for multi-particle effects. A famous example is the model from Syamlal et al. [171]. They, apply a drag function from 1948, suggested in the book from DallaValle [172]), see Equation (3.12)

$$C_D = \left(0.63 + \frac{4.8}{\sqrt{Re_s / u_{t,rel}}} \right) \tag{3.12}$$

Where $u_{t,rel}$ is the ratio of terminal velocity of a multi particle system compared to a single particle. Typical correlations for $u_{t,rel}$ are given by Richardson & Zaki [173] or Garside & Al-Dibouni [174]. Applying Equation (3.12), results in a formulation for the drag force according to Equation (3.13)

$$K_d = \frac{3}{4} C_D \frac{\varepsilon \rho_g \varepsilon_s}{d_p} \frac{\Delta u}{u_{t,rel}^2} \frac{Re_s}{u_{t,rel}} \tag{3.13}$$

A new, third type of drag function has been developed since the 1990´s. The Energy Minimization Multi Scale Method (EMMS) was first comprehensively described by Li & Kwauk [175]. Since then, the EMMS group at the State Key Laboratory of Multiphase Complex Systems developed that approach further. Today it has gained wide acceptance and is especially applied to FCC riser flow simulations.

CFD results for different gas solid drag functions (C_D)

Table 9 summarizes results for fluidized-bed simulations applying and comparing different drag functions.

Table 9 Literature review – drag functions

Ref.	Geldart type	u/u_{mf}	Drag Model	Other setting	Results
Ghadirian [176]	A; B	10-13	Syamlal; Wen-Yu; EMMS	2D;	a) Bed expansion and voidage for EMMS case much smaller, which fits better to exp. results; b) pressure drop fluctuation for EMMS higher
Lundberg [168]	B	13	Syamlal, Gidaspow,	2D,	Both Syamlal and Gidaspow fail to predict the bubble frequency to be high in bed center an lower near the walls
Benzarti [177]	A		Syamlal; Gidaspow; EMMS	2D; e=0.7;	Bed expansion and voidage for EMMS case much smaller
Benzarti [178]	B	66.-81	Syamlal; Gidaspow; McKeen	2D	Gidaspow gives better agreement with experiments than Syamlal and McKeen for most measure
Du [179]	B	2.3-2.8	Syamlal; Gidaspow; Di Felice; Richardson-Zaki	2D; e=0.9; spout bed	Most models show good qualitative agreement with exp. Gidaspow gave usually better resutls
Loha [180]	B	2.2	Syamlal; Gidaspow; McKeen; EMMS	2D; e=0.99; k-ε-model	EMMS and McKeen failed to predict particle velocity and bed height
Min [181]	B	2	Syamlal; Gidaspow; Wen-Yu	2D/3D; e=0.9	Gidaspow and Syamlal gave better results compared to Wen-Yu
Li [182]	A	76-132	Syamlal; Gidaspow; McKeen	2D	Syamlal &Gidaspow overestimate drag force
Hernández-Jiménez [183]	B	1-2	Syamlal; Gidaspow	2D; e=0.95-0.99	Gidaspow gives better agreement with experiment for most measures
Lungu [184]	B	5	Gidaspow; EMMS	2D	Bed height and voidage predicted better by EMMS, other measures doesn´t show EMMS to be a superior model

3.3.3 Kinetic Theory of Granular Flow (KTGF)

Jenkins & Savage [185] and Lun et al. [186] adopted modeling assumptions from ideal gases in order to describe the rheology of the continuous solid phase. That is, the solids movement can be described by statistical physics just as the movement of ideal gas molecules. A detailed derivation of the Kinetic Theory of Granular Flow is given by Gidaspow [36]. In the following, only a short abstract is presented.

KTGF assumes that particle stresses (τ_s) – which are, according to TFM, a function of viscosity (μ_s, λ_s) – result from two reasons: a) translatory particle movement ($\mu_{s,kin}$) and b) particle-particle collisions ($\mu_{s,col}$).

Early models from Jenkins & Savage [185], neglect stresses induced by particle movement. Thus, they can be applied to very dense fluidized beds only. Lun et al. [186] extended the models by reflecting the influence of gas flow on the particle stress tensor. In some publications a third mechanism effecting the stress tensor is introduced. Solid-solid friction ($\mu_{s,fr}$) was considered e.g. by Huilin et al [187], Patil et al. [188] or Lindborg et al [189]. Considering all three contributors, the solid shear viscosity is defined according to Equation (3.14)

$$\mu_s = \mu_{s,kin} + \mu_{s,col} + \mu_{s,fr} \tag{3.14}$$

In the cases present in Chapter 6, the kinetic part is modeled according to either Syamlal et al. [157] or Gidaspow et al. [190]. The collisional part is modeled according to Gidaspow et al. [190] and the frictional part according to Schaeffer [191]. Huilin et al. [187] mention that the frictional effect is especially important for dense systems with slow shear velocities such as spouted beds. If the model from Schaeffer is applied, some more empirical quantities need to be defined, as discussed below.

Angle of internal friction (Φ)

The angle of internal friction (Φ) is a material property describing particle-particle contacts, rather than particle-wall contacts. It is related to dissipation in dense regions with enduring contacts. For non-cohesive solids it can be taken from experimentally observed angle of response [192]. Usually, Φ ranges for different particles from 10° to 40°. Most of the published simulation results assumed a value of 30°. Reuge et al. [192], investigated a bubbling bed of Geldard group B particles at low gas velocities. The angle of internal friction was varied from 10° to 40°. They found that the bed height is not sensitive to Φ, whereas there is a proportional and linear dependency of height fluctuations. A higher values for Φ implies more friction between the particles which in turn accounts for larger heterogeneities in the flow [192]. In the cases present in Chapter 6, Φ is set to the commonly applied value of 30° [157].

Frictional pressure (p_{fr}) and modulus (G_{fr})

The frictional pressure (sometimes misinterpreted as critical state pressure [193]) is discussed in more detail by Arastoopour et al. [193]. Commonly applied models for p_{fr} were suggested by Syamlal [157] and Johnson & Jackson [194]. If the latter model is applied, the frictional part of the shear viscosity is calculated according to Equation (3.15)

$$\mu_{s,kin} = p_{fr} \sin \Phi \tag{3.15}$$

The cases present in Chapter 6 use a formulation for the frictional pressure and frictional modulus as suggested by Gidaspow and Ding that is based on the KTGF [36].

Friction packing limit ($\varepsilon_{s,fr,max}$)

The friction packing limit defines the threshold at which the frictional contribution ($\mu_{s,fr}$) to the solids shear viscosity (μ_s) will be included. Usually, the threshold value is chosen in conjunction with the expected maximum packing limit of the bed ($\varepsilon_{s,max}$) [157]. For typical cases of $\varepsilon_{s,max}$=0.63, the frictional regime is set to start at $\varepsilon_{s,fr,max}$=0.55.

Apart from the frictional contribution to solids shear viscosity, some important aspects for the calculation of the other contributor to solids stress tensor shall be given below.

In KTGF two new properties to calculate the bulk viscosity and the kinetic part as well as the collisional part of the shear viscosity are introduced. Those are the coefficient of restitution (e) and the granular temperature (Θ).

Coefficient of restitution (e)

The coefficient of restitution is a measure for the loss of kinetic energy during particle-particle collision. It varies between unity and zero. The case e=1 represents a fully elastic collision where no kinetic energy dissipates. If e=0, all kinetic energy dissipates under collision (inelastic). The coefficient of restitution is one of the few empirical values in a KTGF model set [154] and is the key parameter in describing the solid-solid momentum transfer. Virtually all publications use values between 0.7 and 1 for this coefficient [195]. Results from dense fluidized beds (e.g. bubbling beds) show a larger sensitivity to the coefficient compared to leaner systems as summarized in Laugwitz et al. [196], Reza, Laugwitz et al [197] and Enwald [154]. An increase in e results in increased granular temperature and a decreased particle pressure for dense beds [195]. Consequently, viscosity and diffusion increase which decreases gradients over the bed [154]. As a result, simulations with e approaching unity show a drastically reduced bubble formation, a homogenized bed comparable to "particulate" fluidization cases (see Yang [89]) and a less diffuse bed surface as well as lower pressure drop fluctuations [195,198–200]. Reuge et al. [192] have summarized the influence of the coefficient of restitution as reported from several

authors. It should be noted that the coefficient has a physical meaning and could be argued to be a material property with a constant and measurable value [154]. On the other hand, Lun et al. [201] show that e is also a function of impact velocity, which makes it even more complicated to define this value. It is obvious that the nature of a TFM model does not allow for calculating the individual impact velocities between two single particles as all particles are merged into a joint phase. However, the overwhelming majority of publications use a value between 0.9 and 0.99 without any reference to an experimentally determined value.

It should be mentioned that solid-solid momentum transfer (K_{ds}) is (in addition to the coefficient of restitution) also a function of the coefficient of friction (c_{fr}) and the radial distribution function at contact (g_0). In the most cases, momentum exchange by friction is neglected giving $c_{fr}=0$. The radial distribution function is a dimensionless distance between particles. It is meant to correct the probability of particle collision for dense beds. In dense systems g_0 approaches infinity whilst in dilute systems it approaches unity.

Granular temperature (Θ)

The granular temperature is a measure for random oscillation of particles [158]. It reflects the kinetic energy of a fluctuating dispersed phase. In kinetic gas theory, the Boltzmann constant is used to convert thermal energy (fluctuation) to thermal temperature. In KTGF this conversion factor is unity. It can be shown that Θ equals the average of the three variances of the particle velocity [158]. This relation is exploited when measuring Θ via optical techniques.

Two approaches can be found to model Θ. First option is to solve the complete set of partial differential equations (PDE) for Θ. This is computational expensive. The alternative is to neglect transport of Θ by advection, putting emphasis on local dissipation only [157]. This assumptions allows for an algebraic formulation of the conservation equation for Θ, which can be computed much faster. In some cases this simplified model causes higher velocity fluctuations and predicts higher granular temperatures compared to the PDE case. Unfortunately, this trend depends on the resolution of the numerical grid and the applied discretization scheme (e.g. first order or second order) [157]. Thus, it is difficult to tell if a present case should be calculated with the costly PDE approach or if the differences to the simplified algebraic model are negligible.

3.3.4 Conclusion

Different model approaches can be found to calculate multi-phase flow. The distinguishing feature is whether the solid phase is treated in a Lagrangian or Eulerian manner and whether the gas phase is treated in a Lagrangian or Eulerian manner. Computational expensive approaches such as molecular dynamics and resolved DPM approaches can be

feasibly applied to small systems only. However, these approaches are applied to derive closure terms that can be transferred to larger scale simulations, such as Unresolved DPM or TFM.

Even though application of Euler-Euler simulation in conjunction with the KTGF is state-of-the-art in lab-scale and large-scale fluidized-bed modeling, there is a considerable uncertainty in the choice of adequate models and model parameters. There is a lot of research in developing improved models that are more physically sound and applicable to a wider range of fluidized beds. On the other hand, there are a lot of publications that investigate a certain type of fluidized bed reactor by means of CFD. Often, the latter group of publications seems to apply an arbitrary set of models and parameters that has been successfully used before, without showing whether a transfer of these models and parameters to their type of fluidized bed is reasonable. In other words, the validation of a certain CFD setup to be suitable to the present type of fluidization is often missing. Here, it is believed that a numerical setup needs to be verified and validated under fluidization conditions comparable to the actual system under investigation (here COORVED gasifier). There will be a discussion in Chapter 6, about the identification of suitable validation experiments from literature and simulation of these experiments.

4 COORVED Gasification Concept

This chapter is designated to introduce the basic concept of the investigated gasifier. Because this gasifier has been already introduced by Meyer et al. [22], Laugwitz and co-workers [2,196,202,203], Gräbner and co-workers [10,23,80] and others [204–208], only some facts will be repeated here. In addition, some hydrodynamic features will be explained in more detail. For this, a perspective is chosen that allows for a straightforward linkage of the gasifier´s expected characteristics and the evaluation tools introduced in Chapter 3.

4.1 Concept of Staged Conversion

As already mentioned in Chapter 2.1.4 Technology Development Trends, several approaches for improved gasifiers have been presented. A few of them apply the concept of staging [51–54,79,209,210]. “Staging” can refer to different methods:

- solids feeding at different heights,
- applying primary and secondary gasification agents,
- demerging of the conversion zones in fixed-bed gasifiers,
- cascades of fluidized beds
- staging the flow velocity by means of variable diameters
- staging the temperature profile
- presence of catalysts over a certain height

In any case, the degree of freedom during design and operation of such a gasifier is increased. All concepts are unified by the overall goal to completely convert the feedstock and to produce a high quality syngas (usually “high-quality” refers to “free of higher hydrocarbons”). This is especially difficult if low quality feedstocks need to be converted, as entrained-flow gasification is unfeasible (see Chapter 2.1.3).

4.1.1 Drawbacks of Conventional Fluidized-Bed Gasifiers

The investigated COORVED gasifier is derived from HTW-like fluidized bed gasification. The superior heat and mass transfer in fluidized beds is especially advantageous for high-reactive and low quality feedstocks. The two major drawbacks of fluidized-bed gasifiers are the incomplete carbon conversion and the lower syngas yield compared to entrained-flow gasifiers (see Chapter 2.1.2). Carbon is lost in the fly ash and mainly via the solid bottom product. This results in the necessity to combust the bottom ash in an external furnace because it must not be disposed having such a high carbon content. The methane content is around 5 $wt\%_{dry}$ owing to the operation temperatures being 850-950°C. Both issues, conversion and syngas quality, shall be improved in the new, staged gasifier. In the most simplified description, there are two differences to the HTW-type gasifier:

1. The unconverted carbon in the bottom ash is internally post-gasified
2. Injection of the (primary) gasification agent is no longer distributed over many nozzles, but a single central jet is introduced.

To decrease the carbon content of the bottom ash below 5 $wt\%_{dry}$ would allow for its disposal. In addition, it improves thermodynamic key performance indicators (e.g. cold gas efficiency, syngas yield) of the gasifier.

4.1.2 Basic Concept COORVED Gasifier

Figure 20 shows the four different hydrodynamic zones of the COORVED gasifier. Those zones encompass a fixed bed and a fluidized bed area. The fluidized bed area can be subdivided on a bubbling-bed zone, a jetting-bed zone and a fast-bed zone. Their occurrence and function of each zone is explained in the following.

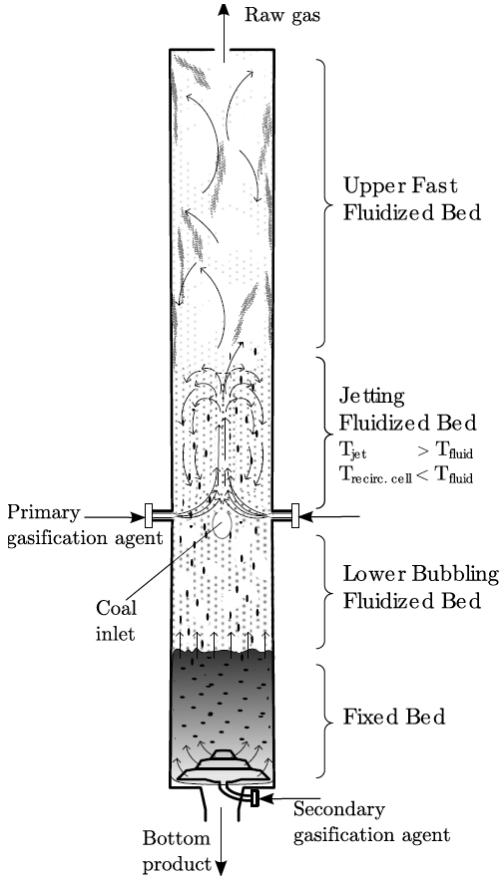

Figure 20 Hydrodynamic zones of the COORVED gasifier, adapted from Laugwitz [196]

4.1.3 COORVED – Fixed-Bed Zone

Internal post-gasification of the bottom ash is achieved by collecting the carbon containing ash as ash agglomerates at the bottom of the gasifier. Secondary gasification agent is injected through a rotary grate (comparable to rotary grates from Lurgi-FBDB gasifiers).

In this way, a fixed-bed gasification is established at the bottom. The fixed bed is formed by ash agglomerates and oversized grains from the fresh feedstock. The possibility to gasify large feedstock particles in the bottom fixed bed results in simplified feedstock preparation. A broad feedstock size distribution can be fed to the gasifier. Both crushing and sieving is not as important anymore. The produced gas from the fixed bed is composed of post-gasification syngas and surplus secondary gasification agent. The composition of the secondary gasification agent is chosen to avoid hotspots in the fixed bed. Its flowrate is chosen to cause a certain gas velocity above the fixed bed. This fixed-bed gas will induce a bubbling-fluidized bed above.

4.1.4 COORVED – Bubbling-Bed Zone

The bubbling bed is the second stage of the gasifier. It is extended from the top of the fixed bed up to the height of primary gasification agent injection. The bubbling bed is composed of particles of a certain size range, depending on the preset gas velocity from the fixed bed. Fines are entrained to the zone above, whilst larger agglomerates and oversized fresh feedstock will fall down onto the fixed bed. In so far, the bubbling bed has the functionality of an air classifier. In the upper region of the bubbling bed, the fresh feedstock is injected by means of a gravitational chute. This is done right below the injection nozzle for the primary gasification agent for safety reasons. It must be avoided that oxygen can travel in a short circuit right into the feedstock chute. Thus, primary oxygen is fed above the coal chute.

4.1.5 COORVED – Jetting-Bed Zone

The primary gasification agent (mixture of pre-heated oxygen and steam) is injected through single nozzle(s) as fast gas jet(s). Depending on the unit size, a single central nozzle can be applied (e.g. the investigated lab-scale unit) or up to 4 nozzles can be distributed around the circumference in a boxer arrangement (e.g. a large scale, industrial unit). In the latter case, the jets will conjoin in the reactor centre and form a single up-flowing jet. In each case the jet will cause a jetting fluidized bed. The oxygen will induce a hot, flame-like region. Here, temperatures above 2000°C can be found. Nevertheless, the particle residence time in this flame-like region is short. Thus, particles will not be liquefied. However, it is known from other jetting fluidized-bed gasifiers that coal particles can partially melt at the surface if a certain degree of carbon conversion was reached [211,212]. In most cases, particle agglomeration is unintentionally and should be avoided [213]. In the present case, agglomeration is a desired phenomenon. Produced agglomerates are too heavy to be fluidized. They will fall down and build up the bottom fixed bed. Due to the nature of the mechanics and chemistry of a char-ash structure [214,215] the agglomerates will have a carbon content below 25% [75,211,216]. As a result an ash-rich fraction is permanently extracted from the jetting zone and the zone above. Thus, the carbon concentration is high in those main reaction zones, which improves efficiency. As

already discussed in Chapter 2.2.4, the jet will induce a recirculation cell. Figure 10 shows that the solids concentration in the descending annulus region is comparably high. In this way, the reactor walls are protected from flame radiation and thermal stresses. Thus, clinkering at the wall is reduced and refractory stand time is increased. Moreover, the recirculation cell increases the residence time of gas and solids in this hottest reactor zone. This is especially advantageous for the solids conversion progress and the syngas quality. The latter fact has not been discussed in the aforementioned publications. It can be expected that the pyrolysis gases that are released in the bubbling bed and jetting bed will travel through the hot flame zone. Even methane will be thermically decomposed at those flame temperatures (>2000°C). Heterogeneous methane formation in the upmost zone (see below) is unlikely as residence times are short and temperatures moderate. Finally, the methane content of the produced raw gas is expected to be very low, resulting in a very high syngas yield. In the jetting zone, particles are converted to gas. The gas travels upwards whilst the jet vanishes. As particle conversion progresses, the gas flow rate and thus the gas velocity increases. After the jet dissipated into the overall gas flow, the fourth zone is established (fast bed).

4.1.6 COORVED – Fast-Bed Zone

Due to the comparable high superficial gas velocities, a fast bed is present. Here, only endothermic heterogeneous reactions and gas-phase reforming reactions can be found. The temperature will be reduced to approx. 1100°C. If the temperature decrease is insufficient, water spraying might be provisioned. The raw gas and fly ash leave the reactor at the top. On the one hand, fly ash entrainment causes a small carbon loss. On the other hand, it is known from HTW operation that fly ash serves as adsorption surface for condensing compounds (e.g. alkali and earth-alkali species). In this way, fly ash decreases fouling tendencies in subsequent raw gas coolers (heat exchangers). Fly-ash recycling might be an option, but would increase the complexity and thus costs of the gasifier.

To summarize, four stages can be found in the cylindrical gasifier. From bottom to top there is a fixed bed, a bubbling fluidized bed, a jetting-fluidized bed and a fast bed. The zones interact by means of particle and gas exchange. From bottom to top the particle size decreases whilst the gas velocity increases due to gas production. Secondary gasification agent is added at the very bottom. Primary gasification agent is added right above the feedstock injection.

4.1.7 Conclusion

The new, staged gasifier allows for complete carbon conversion and a high syngas yield at moderate outlet temperatures. Thus, the system overcomes the drawbacks of fluidized-bed gasifiers (carbon loss via bottom ash) and fixed-bed gasifiers (tar-oil-dust-mixture in the raw gas) by combining these two gasifier types. Apart from a superior thermodynamic

performance (cold-gas efficiency, syngas-yield), the COORVED gasifier requires less feedstock preparation as a wide particle size distribution can be fed. The thermodynamic advantage allows for efficient conversion of low-quality feedstock, especially high-ash coal fines. As discussed in Chapter 2.1.4, this is highly attractive for the international market. The wide particle size distribution allows for application of feedstock-mixtures such as waste-coal mixtures, which is highly attractive for both the German market and the international market.

4.2 Test Facility and Reactor Design

The concept of the gasifier, introduced in the chapter above, was successfully demonstrated in an atmospheric lab-scale unit at the IEC at the Technische Universität Bergakademie Freiberg. A detailed technical description of the gasifier, peripheral units and operational results will be given in the PhD thesis of Martin Schurz, 2017. Parts of that have been published elsewhere [205–207]. The tools described in Chapter 3 will be applied to this lab-scale unit. Thus, a required minimal amount of information on that unit will be provided here.

Its parameters are [205]:

- 15 cm inner diameter (D)
- Height of the reaction tube 4.8 m (H)
- 3 mm nozzle diameter (D_0)
- pressure 10 mbarg
- feedstock particle size max 500 µm
- thermal input of 60–125 kW; 10–15 kg/h
- prim. gasification agent max. 8 m^3(STP)/h
- sec. gasification agent max. 20 m^3(STP)/h
- gasification agents allow for an adjustable composition of oxygen, steam, carbon dioxide, nitrogen, argon

Compared to the potential industrial-size reactor there are several simplifications. The secondary gasification agent is added through a lance at the bottom rather than a rotating grate (see Figure 21). The slim design will assist the equal distribution of secondary gasification agent. The solid bottom product is discharged discontinuously via a cone valve sluice. The primary gasification agent is fed through a single lance made from aluminum oxide rather than through several nozzles in boxer arrangement. Thus, a vertical jet is directly induced. Finally, the pressure and thermal capacity are much lower compared to an industrial gasifier. Due to the height-to-diameter ratio, high heat losses are expected (15-25% of thermal input). Electrical heaters are installed to maintain the wall temperatures at 900°C.

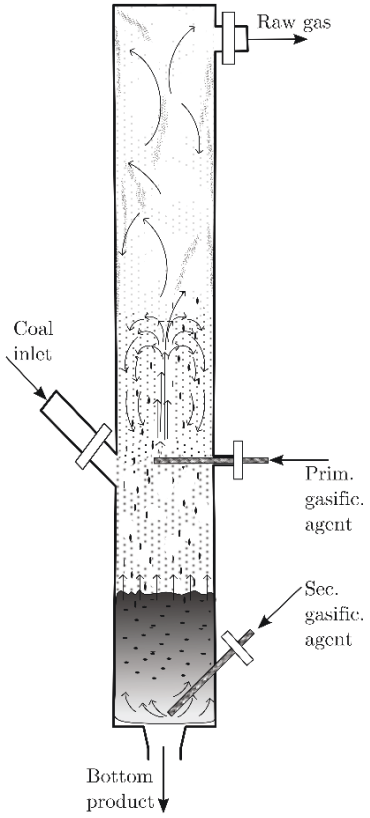

Figure 21 Geometry of lab-scale unit

The lab-scale unit is equipped with several measurements for temperature and pressure over height. Moreover, gas analytics by means of gas chromatography (Agilent G2802A Mikro-GC) and Fourier-Transform-Infrared-Spectrometer (Ansyco CX-4000 FT-IR) are applied. However, no measures for the hydrodynamics are monitored. Thus, too little information to validate numerical models are supplied. This is why a certain effort is required to identify suitable other validation experiments, as will be discussed in Chapter 6.3.

4.3 Cold Flow Test Unit

In order to gain optical access to the jetting region of the gasifier, a cold flow test unit was developed as presented in Schimpke et al. [205]. It is composed of an acrylic glass tube. The cold flow unit has an inner diameter of 15 cm. The original primary gasification lance from the lab-scale reactor is applied in the cold flow unit to facilitate the jet region. The cold-flow unit is applied to investigate the jetting phenomenon and to provide measurement data for validation purposes regarding the CFD setup as will be discussed in Chapter 6.5.2. In addition, the setup was exploited to investigate the development and dimensions of the recirculation cell for different reactor diameters (see Chapter 9.2).

4.4 Reference Cases

The following set of operational parameters, resulting gas properties, as well as particle properties and the resulting nondimensional groups shall be the basis for all simulation activities in the course of this thesis.

4.4.1 Solids Characterization

During the design and engineering phase of the lab-scale gasifier, four project coals have been defined. Later, two of them (Rhenish lignite and Lusatian lignite) have been gasified in several campaigns. For hydrodynamic investigations, only physical properties need to be defined, rather than chemical composition or ash properties. The main challenge in defining the solids properties is to condense the distributed properties of a polydisperse bulk into mean values. Moreover, sampling and analyses of the delivered feedstock would be a chapter for its own. Another type of complication results from the development of physical particle properties during the gasification process. Thus, properties of the fresh feedstock may differ from the relevant properties within the fluidized bed. Changing density, size and shape can be expected. Table 10 shows the mean properties of the fluidized material as assumed. Most important are the assumption that a) the density of agglomerates and of the fluidized bed material are the same and b) that agglomerates grow to a mean diameter of 5 mm and the fluidized bed material is of a size of 95 µm. It should be noted that the properties from Table 10 have a noticeable variance in reality.

Table 10 Solids properties for COORVED reference case

Solid	d_p (mm)	ρ_p (kg/m³)	Geldart class
Reference feedstock	0.095	1052	A
Reference agglomerate	5.0	1052	D

4.4.2 Gas Phase Properties

This section summarizes the properties of the gas phase in each hydrodynamic zone of the fluidized bed. Important properties are the density and viscosity of the gas. Those are a function of composition, temperature, and pressure. The volume flow in each zone will result in a certain superficial gas velocity. From those measures, nondimensional groups that are required e.g. in the Reh diagram can be calculated.

A series of thermodynamic calculations have been conducted during the course of design and development of the lab-scale unit. Here, 4 different potential feedstocks and different

compositions for the secondary gasification agent have been assumed (see 10.1). The calculations resulted in different gas compositions and temperatures in the different fluidized-bed zones. The results were used to calculate nondimensional groups under the assumption of constant particle properties for each feedstock (see Table 10). The maximum and minimum values were identified for each zone. Thus, the lab-scale gasifier is expected to be operated only in this range of hydrodynamic regimes. The bottom fixed bed has Re>5.56 and Ar>3.41e+05. The bubbling bed is fluidized at least with Re=0.18 and Ar=8.43, whilst the upper fast bed exhibits Re<1.07 and Ar<0.90. Those values are visualized in Figure 22 in the following chapter. The jetting bed cannot be visualized in the Reh diagram because of the large radial gradients for temperature and velocity.

Applying the correlations from Table 4, the transition to fast beds starts between 3 m/s and 4 m/s. The reference case and the other cases listed in Table 12 have superficial gas velocities in the fast-bed zone between 1 m/s and 2 m/s. This is a little below the calculated values but still the characterization as fast-bed is very reasonable.

5 COORVED Reactor in Flow Regime Diagrams

The Reh diagram was introduced in Chapter 3.1. Here it is used to demonstrate that the designed operation cases are likely to result in the expected fluidization regimes. The Reh diagram can be applied to discuss three out of four hydrodynamic zones (fixed bed, bubbling bed, fast bed) of the staged gasifier. The fourth zone (jetting bed) required another regime diagram (see Chapter 5.3).

In the Reh diagram, it is possible to visualize achieved operational results and to assess differences in the expected fluidization regimes and the actually realized ones.

It will be shown that there are limitations when the jetting zone is investigated by means of available regime diagrams. However, there is strong evidences, based on those diagrams that a jetting-bed is much more likely than a spouted bed.

5.1 Reh Diagram for the Reference Case

The variety of design cases lead to a variety in operational points in the Reh diagram. For the sake of lucidity, not all potential operational points are shown, as e.g. in Gräbner [10]. In Figure 22, only the outer boundary points are given. Thus, all designed cases are expected to lie within those values. In so far, the data shown in Figure 22, and summarized in Table 11 are the reference case for this thesis.

Table 11 Coordinates for the Reh diagram (reference case)

Zone	Re	$3Re^2/4Ar$	Comment
Fixed bed	5.56	6.78e-05	Calculated for reference agglomerates (compare Table 10)
Bubbling bed	0.18	2.71e-03	Reference feedstock is fluidized in the "fines bubbling regime" (compare Figure 15)
Fast bed	0.99	8.10e-01	Reference feedstock is fluidized at the boundary to entrainment

It can be seen that the reference agglomerates in the fixed-bed regime have a safe distance to the point of incipient fluidization. The bubbling bed zone is located in the "fines bubbling regime" (compare Figure 15). However, the distance to the "CFB" region is small. It can be expected that the bubbling bed is highly expanded and that there won´t be a distinct bed surface, even under this theoretical monodispersed conditions. This is advantageous, because injected feedstock will be easily fluidized up to the primary gas

injection. The fast-bed zone is located on the boarder to the entrained-flow regime. Formation of strands and a core-annulus structure is likely and the relative velocity can be expected to be high.

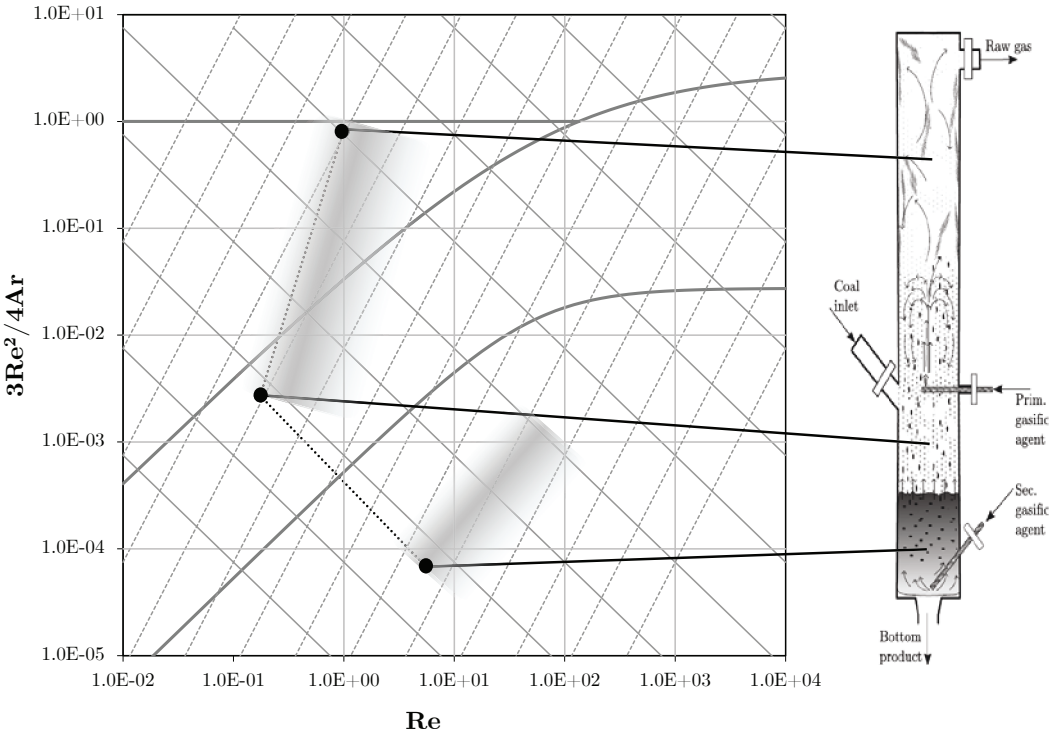

Figure 22 Operational regime, COORVED lab-scale unit

5.2 Reh Diagram for Experimental Campaigns and CFD Case

A few experimental campaigns (EC) have been analyzed towards realized hydrodynamics. Again, the assumptions for material properties according to Table 10 have been employed. Four data sets are discussed in the following. Table 12 summarizes the retrieved information. It should be noted that EC2 and EC3 have been conducted in an adapted reactor geometry (see Chapter 9.2 and Appendix 10.2). However, different geometries can be compared in the Reh diagram as the applied nondimensional groups to not reflect reactor geometries. That is the main advantage of flow regime diagrams. On the other hand, different reactor diameters might result in different superficial gas velocities, which could be seen in the Reh diagram. In any case, the operational point from EC1 can be compared to EC2 and EC3 in the diagram.

In addition, a CFD case was developed. Here, the defined boundary conditions are based on the respective patent [22]. The main difference to the reference case and experimental campaigns is the application of slightly larger particles of d_p=150 µm rather than 95 µm. A more detailed description of the results from the CFD case is given in Chapter 6.4.4.

Table 12 Reh diagram coordinates for experimental campaigns and CFD case

Exp. Campaign (EC)	Date of campaign	Bottom zone	Bubbling-bed zone	Fast-bed zone	Comment
EC1	20.06.14	Re=47.4 $3Re^2/4Ar$=5.2e-04	Re=0.33 $3Re^2/4Ar$=2.5e-02	Re=0.61 $3Re^2/4Ar$=0.31	
EC2	18.02.16	Re=27.2 $3Re^2/4Ar$=3.3e-04	Re=0.55 $3Re^2/4Ar$=0.10	Re=0.53 $3Re^2/4Ar$=0.16	
EC3	24.05.16	Re=41.3 $3Re^2/4Ar$=7.2e-04	Re=0.45 $3Re^2/4Ar$=8.6e-02	Re=0.56 $3Re^2/4Ar$=0.17	
CFD	-/-	-/-	Re=0.59 $3Re^2/4Ar$=1.6e-02	Re=1.67 $3Re^2/4Ar$=0.13	Agglom. neglected

Figure 23 shows the operational points for EC1, EC2, EC3 and the CFD simulation. It can be seen that all points lie within the expected range of operational parameters, as identified in thermodynamic simulations (compare Figure 22). In addition, it can be seen that the three experimental points (EC1–EC3) and especially EC2 and EC3 are close to each other from a hydrodynamic perspective. It is obvious that the expected bubbling bed zone (zone between the bottom fixed bed and the jetting bed) is not operated in the bubbling-bed regime. Comparably high gas velocities resulted in high Reynolds numbers and a CFB-like behavior.

In the following paragraph it is explained, why elevated gas velocities have been adjusted.

The high gas velocities were adjusted with the secondary gasification agent (injected at the bottom) on purpose for safety reasons. In this way, it was additionally ensured during the experiments that fresh feedstock will be transported up to the oxygen-rich zone (jetting bed). Under any circumstances it must be ensured that carbon rich material is present in this zone. Thus, particles with a size of 95 µm are fluidized under CFB conditions. Nevertheless, a bubbling bed will still be present because also larger particles are fed into the gasifier. For example, for the case EC1, particles above 210 µm are fluidized under bubbling-bed conditions. From this perspective, the disadvantage of reflecting monodispersed particles only, becomes evident. On the other hand, it is straight forward to show which particle sizes will be fluidized under bubbling-bed conditions and which under fast-

bed conditions. This has been extensively done for the present gasifier in Gräbner [10] and Schurz [217].

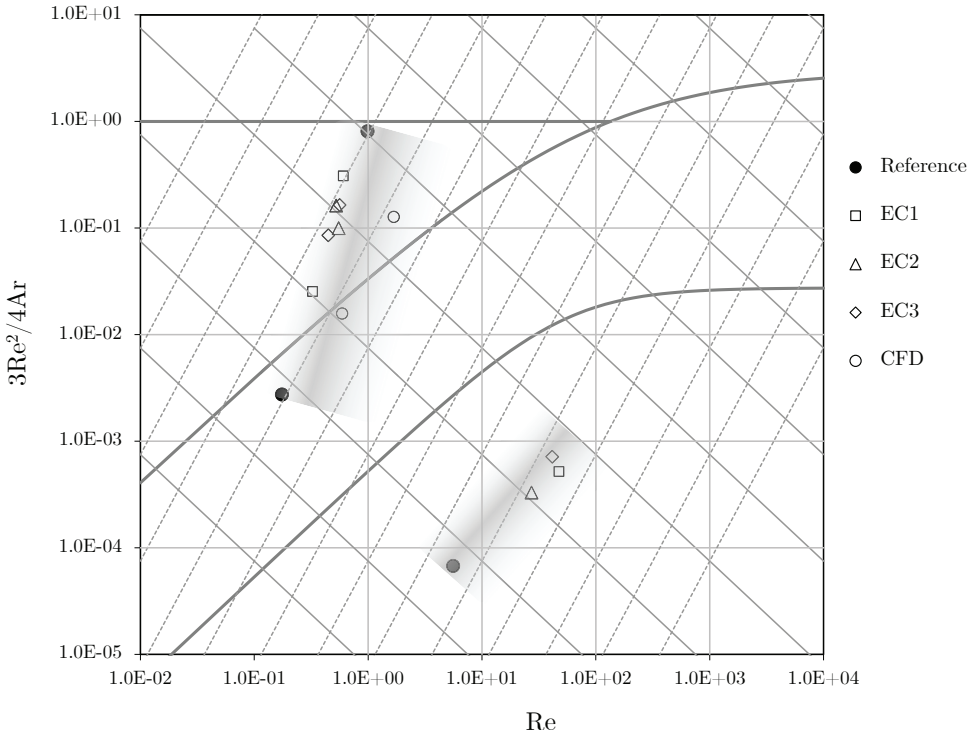

Figure 23 Operational points for experiments and CFD simulation in Reh diagram

The comparable high inlet gas velocity in the bottom region results also in high Reynolds numbers for the fixed bed. The fixed bed point for EC1–EC3 are on the upper right hand side of the reference point. Still, a fixed bed is formed for particles of 5 mm. For the CFD case there is no point in the fixed bed region because the simulations focused on the fluidized bed part. Agglomeration and fixed-bed formation are neglected. For the CFD case, the bubbling-bed zone and fast-bed zone are on the right side of the reference case and the experimental campaigns (EC1–EC3). The reason is the larger particle size of 150 µm. In addition, the early design, which resulted in the CFD case, featured a lower velocity in the bubbling-bed zone compared to the experimental campaigns. Consequently, the zone is located in the bubbling-bed regime in the Reh diagram. The fast-bed zone of the CFD case is located in the CFD regime, just as found also for the experimental campaigns.

It is interesting to note that there is a much smaller spread between bubbling bed and fast bed for CFD, EC2 and EC3 compared to EC1 and the Reference case. This is caused by the fact that the gas velocity does not change very much between these two zones in the new geometry (EC2 and EC3). Here, both the volume flow and the diameter increase from bubbling zone to fast-bed zone (see Appendix 10.2, Figure 63), resulting in comparable Reynolds numbers (see Table 12). For the CFD case, the velocity difference from

bubbling bed to fast bed is small as well. This is because the simulations neglected chemical reactions and thus neglected the produced additional gas volume from particle conversion. The temperature increase from the bubbling-bed zone to the fast-bed zone was captured within the simulations but does not sufficiently increase the gas velocity and Reynolds number. Finally, it can be seen that the fast-fluidized bed zone from EC2 and EC3 are less intensely fluidized compared to EC1 and the reference cases. This is indicated in the Re diagram because their points are below that of EC1 and reference cases. Thus, a lower voidage can be expected for EC2 and EC3.

5.3 Regime Diagrams for the Jetting-Bed Zone

The regime diagrams from Guo [143] and Link [144] are promising to capture the jetting-bed phenomenon in the COORVED process. However, these diagrams are only valid for the set of experiments, conducted during their development. There, both the applied solids (Geldart group D) and the background fluidization velocity ($u_{bg}/u_{mf} = 1..2$) differ from the present case (Geldart A, $u_{bg}/u_{mf} = 50..300$). Nevertheless, their diagrams can potentially be extrapolated and can be used to show that the investigated gasifier is located in the jetting regime. Figure 24 shows the extrapolated diagram from Guo [143] (compare also Figure 18). Extrapolation (dotted line) is based on their equation, given for the demarcation line between spouted bed and jetting bed.

The cases EC2 and EC3 are assumed to have a smaller voidage (ε=0,95) compared to EC1 and the reference case (ε=0,975) because they are less intensively fluidized (see above). In addition, the nozzle diameter is increased from 3 mm (EC1, CFD, reference) to 8 mm in the new reactor design (EC2, EC3) as shown in Appendix 10.2. Both differences will result in lower values for the abscissa and ordinate in Figure 24 for EC2 and EC3. However, it can be seen that all cases are way above the demarcation line between spouted bed and jetting bed, as expected. The CFD case is not shown in this diagram, because the jet velocity is comparably high (125 m/s). This results in an abscissa value of 3030, which is out of the range of Figure 24.

The applicability of the diagram as proposed by Link [144] (see Figure 19) is even more questionable as the underlying experimental conditions are further away from the present cases. The main difference is the comparable low background fluidization. The present COORVED cases would result in ordinate values from 11,000 up to 48,000 (compared to 2..48 [144]). Abscissa values range from 90 to 620 (compared to 1..2). The operational points for the COORVED cases would be located in the far up-right area ("Jetting bed") of the diagram (see Figure 19). However, an extrapolation of the diagram into such regions is not reliable and cannot be recommended.

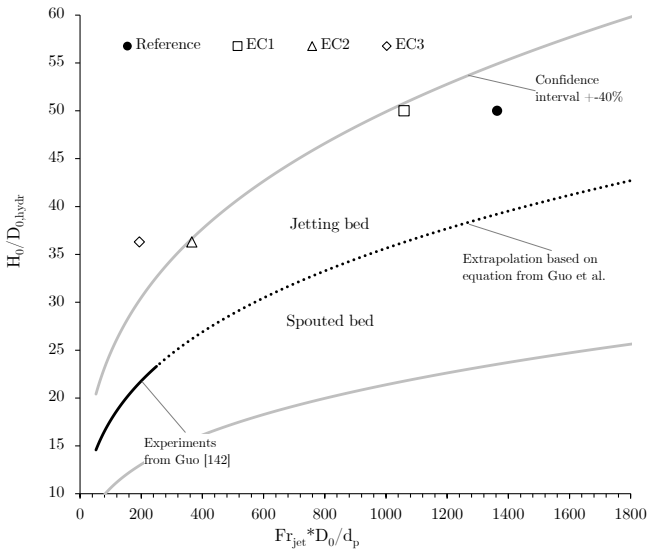

Figure 24 Operational points for jetting zone in Guo diagram, adapted from Guo [143]

5.4 Conclusion

In general it was shown, how the Reh diagram assists in comparing different operational points and different boundary conditions. All the defined points in Table 11 and Table 12 are examples of potential and realized boundary conditions for the staged fluidized-bed gasifier under investigation. All of them are operable and result in the desired staging. The main disadvantage during application of the Reh diagram is the negligence of the bulk polydispersity. This might lead to misinterpretation e.g. regarding the presence of a bubbling bed. It is not a question of –will there be a bubbling-fluidized bed?– it´s a question of –what is the mean particle size in the bubbling bed?–. As an example, the mean particle size within the fluidized bed for the case EC1 is 0.21 .. 1.35 mm. Of course, the reference particle (0.095mm) is already in the CFB regime.

It is more difficult to locate the jetting-bed zone of the presented cases in regime diagrams. It seems that the application of Geldart A particles and a high background velocity has not been intensively investigated before. Thus, meaningful regime diagrams are missing. The diagram from Guo [143] can be extrapolated to COORVED conditions and shows that a jetting bed is very likely. The diagram from Link [144], can hardly be extrapolated to the required conditions. If one would extrapolate though, the present cases would be located in the jetting bed area.

6 CFD Simulation of COORVED Reactor

Before being able to accurately calculate and evaluate the transfer of heat and mass as well as chemical reactions in a gasifier, a sound basis for simulating the hydrodynamics must be provided. This thesis focuses only on the hydrodynamics inside the gasifier. In Chapter 3.3, it was deduced that the present lab-scale gasifier can be efficiently calculated with an Euler-Euler approach in conjunction with the kinetic theory of granular flow (KTGF). The commercial code ANSYS Fluent 14 was used to solve the resulting set of governing equations. This chapter is structured as follows. First, the applied numerical setup is verified in Chapter 6.1. After that the required grid resolution is discussed in Chapter 6.2. The applied models are validated in Chapter 6.3 and Chapter 6.4, respectively. This is essential in gaining trust in the CFD setup. A validation against experimental values from the COORVED gasifier was not possible as hydrodynamic measures are missing. Thus, comparable experiments from literature were considered for validation purposes. After validation, the COORVED gasifier itself was numerically studied. The results are presented in Chapter 6.4.4.

6.1 Verification of Multiphase CFD Setup

Before any numerical setup (CFD or others) can be applied to predict the behavior of a certain system, its reliability has to be proven. For this, usually two steps need to be done: verification and validation. As discussed by Grace and Taghipour [218], too little attention is paid to this, especially in numerical simulation of fluidized beds. Verification involves the comparison of results against known solutions. The main purpose of the verification is to demonstrate that the models and solution procedures have been implemented correctly. This is important for in-house codes as well as for commercial software packages like ANSYS Fluent. According to Grace and Taghipour [218], for fluidized-bed cases, this can be done only for trivial cases. Thus, the pressure drop and minimum fluidization velocity in very simple setups are investigated in Chapter 6.1.2. As TFM simulations are usually transient, computational costs are high. Therefore, the effect of parallelization on the numerical results is investigated in Chapter 6.1.1.

For the following verification procedure as well as for the grid study (Chapter 6.2) the following generic setup was applied (Table 13).

Table 13 Model and parameter setting for verification and grid study

Name	Model/Scheme name
Turbulence model	Unsteady, laminar
Drag force model	Gidaspow (Ergun, Wen&Yu) [190]
Granular temperature	Simplified algebraic form [219]
Granular viscosity	Gidaspow [190]
Granular bulk viscosity	Lun et al. [186]
Frictional viscosity	Schaeffer [191]
Frictional pressure	Syamlal [219]
Solids pressure	Lun et al. [186]
Radial distribution function	Lun et al. [186]
Coeff. of restitution	0.9
Angle of friction	30°
Maximum packing limit	0.55
Frictional packing limit	0.51

The most critical models and parameters will be validated and discussed in subsequent chapters.

The numerical settings are summarized in Table 14.

Table 14 Numerical setting for verification and grid study

Name	Scheme
Pressure-velocity coupling	Phase-coupled, SIMPLE [220]
Spatial discretization gradient	Least squares cell based
Spatial discretization momentum	Second order upwind
Spatial discretization volume frac-	Quick
Transient formulation	First order
Time step size	1e-03 s
Iterations per time step	35

6.1.1 Parallelization

From previous work, it is known that the inconsistent data transfer in HPC calculations can result in a modified solution.

For the verification of the parallelization procedure, a generic numerical test case was constructed. A three-dimensional cylinder of H=1.0 m and D=0.15 m was discretized with an O-grid of 24.700 cells. Initially, solids of d_p=220 µm were defined. The initial bed reached from the bottom (h=0) to h=0.75 with a voidage of ε_{patch}=0.6. Three measurement heights are defined (h_1=0.1 m, h_2=0.5 m, h_3=0.75 m), at which mass-flow weighted averages of the solids volume fraction are captured. The fluidization agent was injected at the bottom at gas velocities just above the minimum fluidization velocity (u/u_{mf}=1.1). The maximum packing limit was defined to be $\varepsilon_{s,max}$=0.63.

Before the effect of parallelization is discussed, the present hydrodynamic situation is explained to understand the curve progression in Figure 25. After the simulation was started, the voidage and bed height decreased due to gravitation. The effective gas velocity at ε>0.57 was not sufficient to counteract the gravitational force. Hence, there is a first period with increasing solids volume fractions at h_1 and h_2 (see Figure 25) until the maximum allowable value of $\varepsilon_{s,max}$=0.63 is reached. The solids volume fraction at h_3 rapidly falls down from 0.4 to 0 for obvious reasons. After approx. 0.8 s, h_2 experiences a decreasing solids volume fraction because more solids leave this zone downwards compared to solids coming from above. A comparable transition point can be found for h_1 after 2.5 s. After 3.0 s a quasi-steady-state is reached. After this, the solids volume fraction at h_1 remains constant at 0.6 whilst there are no more solids at h_3. The solids concentration at h_2 fluctuates between zero and 0.1 with a mean of 0.035. Thus, the final fluidized-bed height can be assumed to be at 0.5 m.

However, the comparison between single core calculation and parallel calculation over 10 cores, shows essentially the same curve progression. Both the final quasi-steady-state situation as well as the required time to reach the quasi-steady-state at the different heights are the same. It is found that the parallelization procedure does not effect the results significantly.

The same agreement between single core and parallel simulations was found for a thermal measure. Isothermal reactor walls (1200 K) were defined to heat the rising gases of a fluidized bed (other boundary conditions were similar to the conditions above). The time to reach a quasi-steady-state (5 s) as well as the resulting gas outlet temperature (1170 K) are the same for both cases (see Appendix 10.3.1). Thus, simulation results for both the hydrodynamics as well as gas heating processes are not affected be the parallelization.

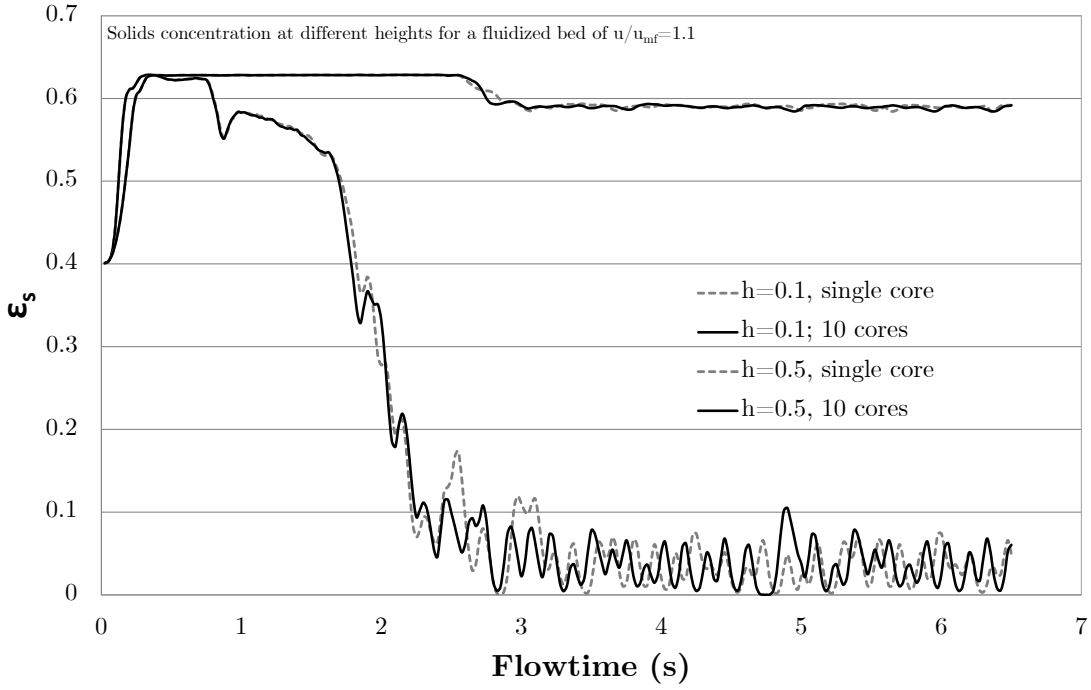

Figure 25 Verification of the parallelization procedure

6.1.2 Pressure Drop and Minimum Fluidization Velocity

The verification for the applied TFM and KTGF are conducted by comparing numerical results against well-known solutions. The pressure drop as a function of gas velocity (compare Chapter 2.2.2) is a feasible measure for this task. Adequate implementation of the models can be assumed if the pressure drop is correctly predicted for fixed-bed cases, fluidized-bed cases and the transition between them. This was evaluated for two different particle sizes (220 µm and 5 mm, compare Table 10) and different velocities in a 2D mesh. In addition, two different gas temperatures were defined to see if a change in density and viscosity of the gas will affect the results in the expected way. The gas velocity was increased stepwise with smaller steps close to the expected point of incipient fluidization. In this way, it is possible to detect the numerically predicted point of incipient fluidization. The comparison of the calculated minimum fluidization velocity against the prediction from empirical equations, such as given in Table 3, is both verification and validation.

However, the pressure drop in a fixed bed is exemplarily calculated with two empirical correlations according to Ergun [91] and Brauer [221]. In fixed beds, the pressure drop is proportional to the velocity until the point of incipient fluidization. After that, in the fluidized bed regime, the pressure drop is constant and equals the specific lifted mass for any velocity (see Equation(2.1)). Thus, there is an analytical solution for the fluidized-

bed regime, which predestines this measure for a verification. Figure 26 show the results for the four different cases.

In general, the numerically predicted pressure drops show a very good agreement with the empirical and analytical solutions for both particle sizes and both temperatures. The increase of pressure drop under fixed-bed conditions is captured with the same high accuracy as the constant value in the fluidized-bed regime. According to Table 15, the numerically predicted fluidized-bed pressure drop differs from the analytical results between 0.6% and 2.2%. Table 15 shows that there is also a high comparability of numerically derived minimum fluidization velocities and the predictions by different empirical correlations. Results from CFD are very close to the results according to the empirical equation from Ergun but little less comparable to that from Chitester. The results according to the empirical equation from Babu [93] lie between the results from the two aforementioned solutions.

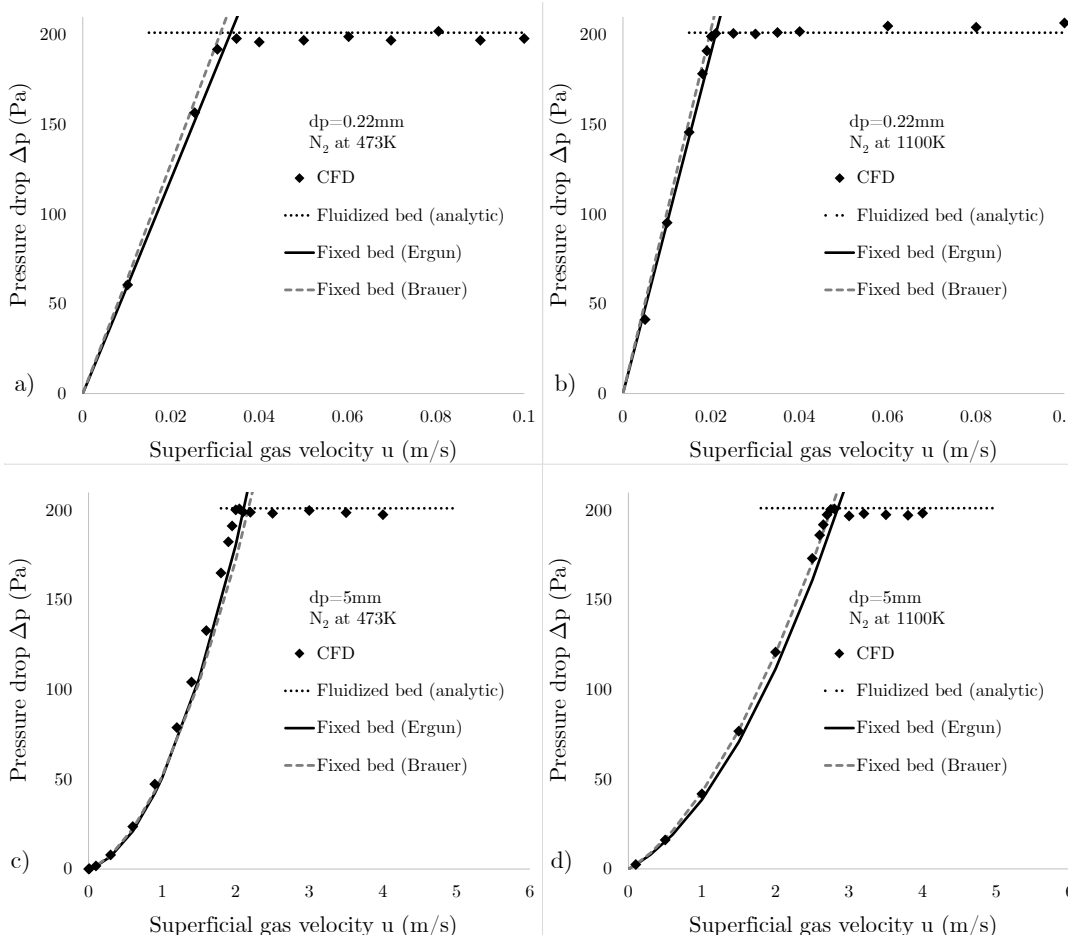

Figure 26 Verification of TFM and KTGF models

Another well know effect becomes evident from the data in Table 15 that is the shift of the point of incipient fluidization with increasing temperature. The tendency, if increasing temperatures will result in an increased or decreased minimum fluidization velocity (u_{mf})

depends on the particle size. To be more precisely: for laminar cases (small particles) u_{mf} will decrease with increasing temperature and for turbulent cases (large particles) u_{mf} will increase with increasing temperature. If the flow around the particle is laminar, the viscous forces dominate over the inertial forces. Thus, u_{mf} is indirect proportional to the dynamic viscosity (η) resulting in u_{mf} being also indirect proportional to temperature. For turbulent flow around particles the inertial forces dominate. Thus, u_{mf} is proportional to gas density and hence, to temperature. The consequence is that $u_{mf,5mm,473K} < u_{mf,5mm,1100K}$ but $u_{mf,0.22mm,473K} > u_{mf,0.22mm,1100K}$

Both the empirical correlations as well as the CFD simulation capture the effect of temperature dependent viscosity and density correctly.

Table 15 Pressure drop and umf – comparison between CFD and empirical correlations

Results	**5 mm; 473 K**	**5 mm; 1100 K**	**0.22 mm; 473 K**	**0.22 mm; 1100 K**
		Pressure drop in fluidized-bed regime Δp (Pa)		
Analytical	201.1	201.2	201.1	201.2
CFD	199.4	198.5	196.7	202.4
Deviation	0.85%	1.36%	2.23%	0.59%
		Minimum fluidization velocity u_{mf} (m/s)		
Ergun [91]	2.10	2.87	0.034	0.019
Babu [93]	1.98	2.63	0.026	0.014
Chitester [94]	1.68	2.15	0.017	0.010
CFD	2.00	2.75	0.035	0.020

6.1.3 Conclusion

The applied CFD tool was successfully verified. Both the parallelization procedure as well as the implementation of the employed models were demonstrated to operate properly. Voidage profiles are the same for simulations on a single computational core and a distributed simulation over 10 cores. The calculated pressure drop profile in a fixed bed and fluidized bed with increasing gas velocities is in accordance with empirical and analytical solutions. Consequently, verification as a first precondition for the application of a simulation tool was successfully conducted.

In general it was found that well-known solutions in simple generic test cases can be retrieved by means of the employed CFD tool very accurately. Thus, the verification was successfully achieved.

6.2 Grid Study

Numerical results should be in general independent from the resolution of the employed computational grid. Usually, the grid resolution is defined according to the applied particle size as cell size (L_c) to particle size (d_p). The required grid resolution (L_z/d_p) is obviously dependent on the applied particle size. Moreover, the required resolution to achieve grid independency is strongly dependent on the evaluated measure. Guenther and Syamlal [222] investigated the shape of a rising bubble under different grid resolutions. They found that for $L_z/d_p<10$ the evaluated measure did not change anymore. Others [192,223,224] confirmed the required resolution of $L_z/d_p=10$. On the other hand, Wang et al. [225], found grid independency at $L_z/d_p=20$ and Chalermsinsuwan et al. [226] achieved grid independent solutions of the fluidized-bed height at $L_z/d_p=100$. The same poor sensitivity from bed expansion to grid resolution was found by Sande and Ray [227]. However, they found a strong sensitivity of the initial bubbling velocity from grid resolution. Grid independent results were achieved at $L_z/d_p<6$. Others report of required resolutions of $L_z/d_p=2$ to achieve independency. Assuming a cylinder with a height of H=1 m and a diameter of D=0.15 m that is used for fluidization of fine particles (d_p=95 μm), a grid resolution of $L_z/d_p=10$ would require 20.6 million cells. If the particles would be 5 mm in size, $L_z/d_p=10$ would require only 142 cells. The computational costs for grid independent solutions are not feasible if fine particle are considered. Thus, in the following it is not the goal to prove grid independency of the results, but to show the sensitivity and the deviations from one grid resolution to another.

The grid study was done with four grids as listed in Table 16 and shown in Figure 27.

Table 16 Grid resolutions for grid study

Grid number	Cell number	L_z/d_p for 95 μm particle
1	7,000	144
2	12,000	120
3	24,700	94
4	100,000	59

In the following, different measures are evaluated to investigate the dependency of the results on the grid resolution. Those include pressure drop, radial voidage profile, bed expansion, radial profiles of the axial components of gas velocity and solids velocity.

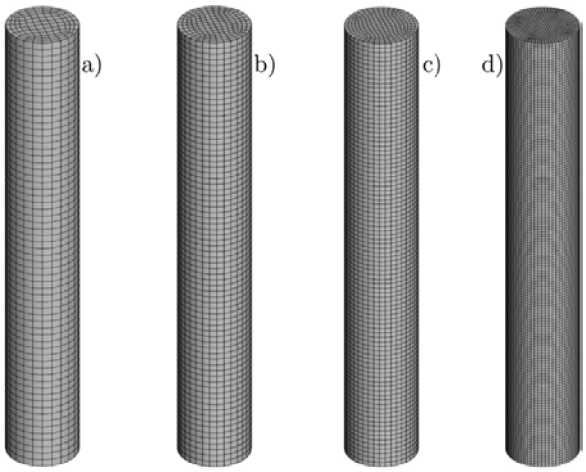

Figure 27 Meshes for sensitivity study a) 7,000 cells; b) 12,000 cells; c) 24,700 cells; d) 100,000 cells

6.2.1 Pressure Drop

First the pressure drop was evaluated for this 3D mesh and d_p=95 μm. From Figure 28 it can be seen that the pressure drop is not sensitive to the grid resolution. The simulation with the highest resolution (100 k cells) was not conducted, because no difference was expected.

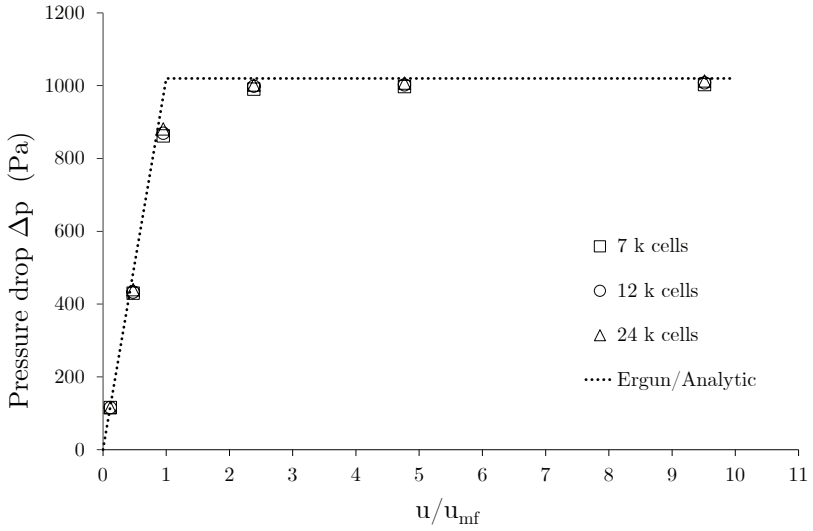

Figure 28 Sensitivity of pressure drop to grid resolution

6.2.2 Voidage Profiles

Radial profiles of the voidage (ε) have been analyzed for three different fluidization numbers at a height h = 0.15 m above the gas inlet. The results for fine particles (d_p = 95 μm) are shown in Figure 29 for u/u_{mf} = 2.4 and 9.5 respectively. The results for u/u_{mf} = 4.8 are shown in Appendix 10.3.2. It can be seen that the sensitivity of the voidage to grid resolution depends on the fluidization number. For slowly fluidized beds the voidage is

almost the same for the three grids. Thus, the computationally expensive high-resolution grid (100 k cells) was not applied here. For increased fluidization velocity ($u/u_{mf} = 9.5$), there is noticeable difference in the computed voidage. Here, the 100 k cells grid was applied to compare the deviations to the coarser grids. The mean voidage differs by 10% from 7 k grid to 100 k grid. The 24 k grid shows a deviation of only 5%. Slightly larger deviations were found for the bed height. For slowly fluidized beds ($u/u_{mf} = 2.4$) the results for the different grids were essentially the same, with errors below 3%. At $u/u_{mf} = 9.5$ the differences become noticeable. Compared to the 100 k grid, the 7 k grid has a deviation in bed height of 18% and the 24 k grid deviates by 13%.

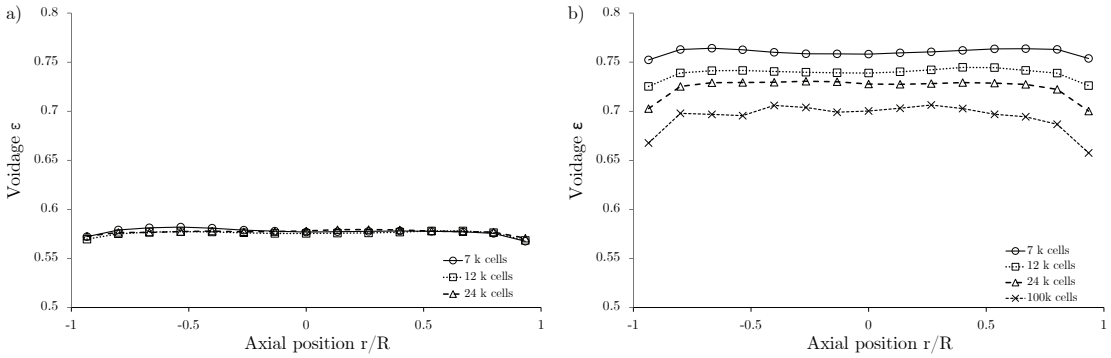

Figure 29 Radial voidage profile for different grid resolutions and fluidization numbers a) u/umf=2.4 and b) u/umf=9.5

Besides the grid resolution study, also a study about the required averaging time was done by means of evaluating voidage profiles. From initialization studies it was found that, the first 5 s must not be considered for averaging. As one example the reader is referred to Figure 25. In the following, it is evaluated for how long the simulation needs to be run in addition to the first five seconds to retrieve independent results.

Figure 30 shows the voidage profile from the 7 k grid for 95 µm particles with u=0.008 m/s. It can be seen that an averaging time of 5 s (period from 5 to 10 s) will deliver noticeably different results compared to longer averaging times. It is found that 20 s of averaging time (period from 5 to 25 s) is sufficient. The averaging period for all following simulations was at least 20 s.

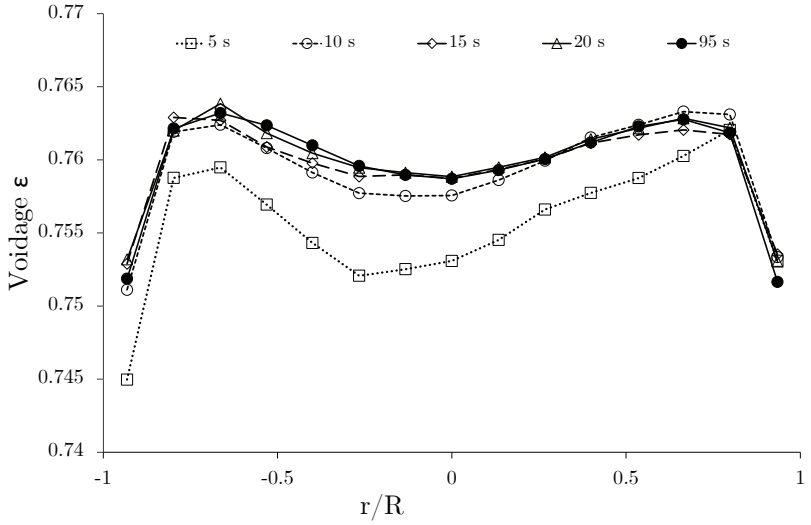

Figure 30 Voidage profile for different averaging periods (7 k grid, dp=95 µm, u=0.08 m/s)

6.2.3 Velocity Profiles

The gas velocity and particle velocity has been investigated also for the three aforementioned fluidization numbers. The deviations for the slowly fluidized beds are negligible and not shown here. Figure 31 shows the result for the highest fluidization number $u/u_{mf} = 9.5$.

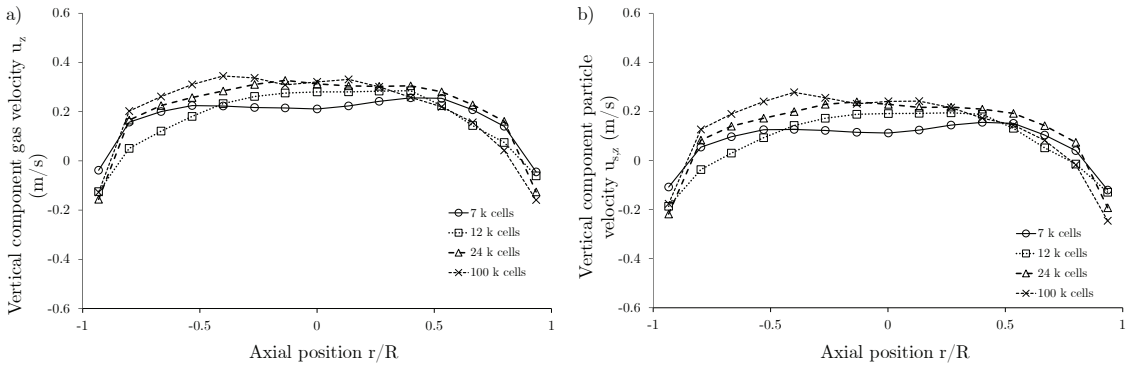

Figure 31 Velocity profiles for different grid resolutions a) gas velocity and b) particle velocity

The deviation of mean gas velocity is 10% and 17%, respectively for the 2 coarsest grids, compared to the 100 k grid. The 24 k grids has a low deviation of only 5%. The deviation of mean particle velocity compared to the 100 k grid comparably high for the two coarsest grids (35–39%). The 24 k grid deviates by 2% only. Apart from the small deviation for the mean velocity, there are larger differences for local velocities close to the wall. The higher the grid resolution, the smaller is the velocity near the walls.

In general, the results gained with the 24 k grid are close to the results from the 100 k grid. Of course, applying the 24 k grid cannot be considered as grid independent simulation, but the error is comparably small and the saved computational time outweighs the

negative aspects. Nevertheless, it is important to be aware of the fact that feasible grid resolutions (L_c/d_p=100) will show some deviations in hydrodynamic measures. The deviations depend on the evaluated measure and vary from 2% to 5% for most of the investigated measures compared to a grid of L_c/d_p=59. The bed expansion is the only measure with a higher deviation of 13%.

6.2.4 Conclusion

Based on the presented results, it is considered that fluidization of 95 µm particles can be calculated on a grid resolution around L_c/d_p=100 feasibly. Several measures do not change significantly (usually below 6%) for higher grid resolutions. However, for the validation phase (Chapter 6.3 and Chapter 6.4), also grids of L_c/d_p=50 have been used.

The required time for averaging was shown to be at least 20 s. For the following validation studies, averaging times of 25 s were applied. The first 5 s of a simulation are not used for averaging. Thus, each simulation was run for 30 s.

6.3 Validation Experiment Bubbling Bed and Fast Bed

After the numerical framework was successfully verified and a feasible grid resolution was identified, it is necessary to validate the models and parameters that can potentially be used to study the COORVED gasifier numerically.

As extensively discussed in Laugwitz et al. (Powder Tech, 2017, under review), there is no model setup available that has already been validated for the different bed types present in the COORVED gasifier. Often, reactive fluidized-bed simulations apply certain models and grid resolutions, without even mentioning if those have been validated for their flow conditions. This thesis, intents to develop a sound basis for the modeling of hydrodynamic phenomenon as a prerequisite for subsequent reactive flow simulations. On the other hand, there is a second type of publications focusing on fluidized-bed hydrodynamics only. Here, developed models and sets of parameters are comprehensively validate against non-reactive flow experiments. Unfortunately, in the overwhelming majority of publications, only one type of fluidized bed (e.g. bubbling or turbulent) is investigated. A prove of the applicability of a certain numerical setup to several bed types is missing. This is usually not an issue as the investigated reactors are usually well defined to operate under e.g. bubbling-bed conditions or circulating-bed conditions. In so far, there is usually no need to calculate different bed types at once. However, for the COORVED gasifier it is. Thus, the applied numerical setup should be valid over a broader range of bed types. The quality of different models and parameters will be tested for bubbling-bed and fast-bed cases in Chapter 6.3 and for jetting beds in Chapter 6.4.

6.3.1 Experimental Setup Holland

The following chapters are designated to identify a suitable reference experiment from literature (Chapter 6.3.1) and consequently to identify a suitable numerical setup (Chapter 6.3.2) to calculate this reference experiment (Chapter 6.3.3).

It is not straightforward to identify a suitable reference experiment for validation purposes. Usually, one tries to find an experiment with particles of the same Geldart class being fluidized in the same bed type. Here, it is believed that this matching procedure is way to crude. The identification of a suitable reference experiment should be based on comparison of dimensionless groups. This can be achieved by plotting the operation condition of potential experiments in a Reh regime diagram (see Figure 15). In the present case, this is complicated by the need to find a reference experiment that investigates both a bubbling bed and a fast fluidized bed. In addition, hydrodynamic measures of high significance should be evaluated. Thus, pressure drop measurements should be accompanied by more complex measures such as voidage and velocity profiles. The latter types of measurements from fluidization experiments of Geldart A particles have been found in only a few publications (see Table 17).

Table 17 Literature survey on potential reference experiments

Literature	Geldart	Regime	Measures
Samuelsberg et al. [228]	A	CFB	Radial profile of particle velocity
v.d. Moortel et al. [229]	B	CFB	Velocity profile; voidage profile
Zhu et al. [130]	A	CFB	Solids velocity
Xu et al. [129]	A-B	CFB	Pressure drop, voidage profile
McKeen et al. [230]	A	BFB	Bed height, bubble diameter bubble velocity
Weber et al. [231]	A-B	BFB	Profile and contour of voidage, bubble diameter
Holland et al. [126]	A	BFB-CFB	Pressure drop, pressure drop fluctuation, contour plots of solids velocity, voidage profiles

Only one experiment could be found that investigated several fluidization regimes with a promising bulk material. Moreover, this potential reference experiment from Holland et al. [126] features highly significant measures, such as contour plots of the axial solids

velocity component. Table 18 lists the most important characteristics of the experiments. Measurements included pressure tapping at 100 Hz to retrieve both the pressure drop as well as its fluctuation. In addition, magnetic resonance was used to measure voidage and velocities on a 2D radial plane. In the experiments from Hensler et al., fluidizing agent was feed through a porous glass frit with a pore size range of 100-160 µm and a pressure drop of 100-3000 Pa over the frit, depending on gas velocity. Three different fluidization velocities (u=0.05, 0.45 and 0.70 m/s) have been used with a very wide spread of the fluidization number (u/u_{mf}=25..350). The same spread can be found for the COORVED gasifier comparing its bubbling-bed zone and fast-bed zone.

Table 18 Experimental conditions from Holland et al. [126]

Property	**Value**
Material	silica-alumina catalyst
Geldart class	A
d_p	70 µm
ρ_p	1530 kg/m^3
ε_{mf}	0.51
$u_{mf,experimental}$	0.002 m/s
Fluidizing conditions	air, ambient
u	0.05/0.45/0.70 m/s
u/u_{mf}	25/225/350
D	50 mm

Both the particle properties as well as the fluidization velocities seem comparable to the COORVED gasifier. As the next step, adequate dimensionless groups need to be compared in order to prove the comparability of the two systems. Figure 32 shows the Reh diagram for the Holland et al. experiment and the reference point of the COORVED lab-scale gasifier (compare to Figure 23). It can be seen that both systems are very comparable to each other from a hydrodynamic point of view. The bubbling-bed zone in the COORVED lab-scale unit (COORVED Reference) is very close to the low velocity experiment (u=0.05 m/s) from Holland et al., as both have almost the same nondimensional groups (Re, Ar, Be, Fr). A voidage around ε=0.7 can be expected for this points. However, the auxiliary lines for the voidage have been left out in Figure 32, for optical convenience. The high velocity experiment (u=0.70 m/s) from Holland et al. compares well

with the fast-bed zone in the COORVED gasifier. The ordinate values are very close to each other (0.8 and 0.5). The Archimedes and Reynolds numbers differ:

$Ar_{COORVED,Fast\text{-}Bed}$=0.9 and $Ar_{Holland,u=0.7}$=13 and

$Re_{COORVED,Fast\text{-}Bed}$=1 and $Re_{Holland,u=0.7}$=3

Nevertheless, the comparability is high enough to identify the experimental series from Holland et al. as validation experiment. Because a particle size of d_p=150 µm was employed in the CFD simulation (compare Chapter 5.2) with an associated increase in base fluidization velocity, the CFD case (COORVED CFD in Figure 32) is even closer to the hydrodynamics of the experimental series from Holland et al.

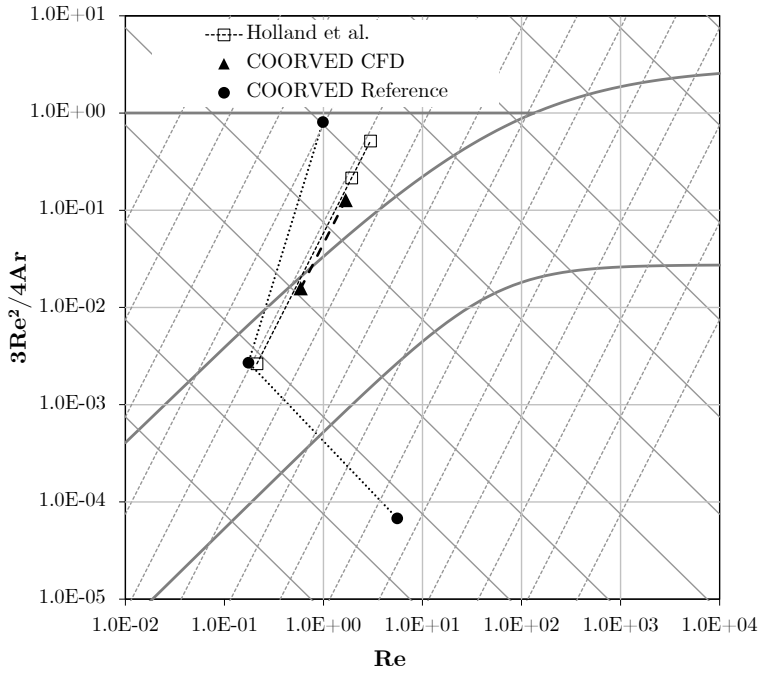

Figure 32 Reh diagram for comparison of COORVED and Holland et al. [126] experiments

6.3.2 Simulation Setup

The experimental geometry (cylinder, 0.05x2.0 m) was discretized with a 3D O-grid of 64 k cells, resulting in L_c/d_p=50 (compare Chapter 6.2). Refinement in the wall regions was conducted as suggested by Pita et al. [232]. The computational grid is shown in Figure 33

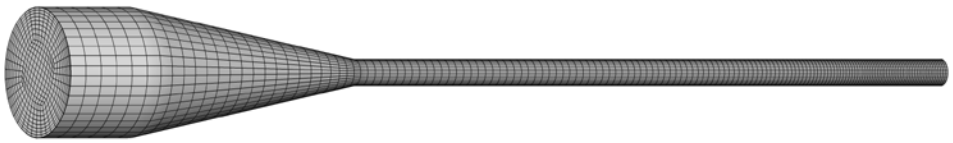

Figure 33 Computational grid for simulation of experiments from Holland et al. [126], adapted from Porter [233]

The applied models, parameters, and numerical settings are mostly the same as listed in Table 13 and Table 14. Table 19 lists the varied models and parameters. Compared to Table 14, the time step size was reduced to 5e-05 s. in order to improve the convergence.

All radial profiles and 2D planes were evaluated at a position of h=50 mm. This is in accordance with the experimental measurement position.

Table 19 Investigated parameters for the simulation of Holland et al. [126] experiments

Name	Model/Scheme standard	Model/Scheme tested
Viscous model	Unsteady, laminar	Unsteady, turbulent (k-ε)
Drag model	Gidaspow (G) [190]	Modified Gidaspow (G+)
Coeff. of restitution	0.9	0.8; 0.99
Granular temperature	Simplified algebraic form	Full set of part. diff. eq. (PDE)

The first step was to prove the experimentally determined point of incipient fluidization (u_{mf}=0.002 m/s; see Table 18). From Figure 34, it can be seen that the simulation setup underestimated the drag forces on the solids and predicted an u_{mf} three times higher compared to the experiments. As a consequence the Ergun part of the Gidaspow model (see Equation (3.11)) was adjusted via a user defined function (UDF) to account for higher drag forces.

A similar procedure to adjust the drag model to meet the experimentally determined point of incipient fluidization was suggested earlier by Syamlal and O´Brien [234] and also conducted successfully by others [226,230]. The drag coefficient calculated with the Ergun expression was increased by a factor of three to meet the experimentally determined u_{mf}. The small influence of that adaption on other measures (e.g. the voidage) is shown in Appendix 10.3.3.

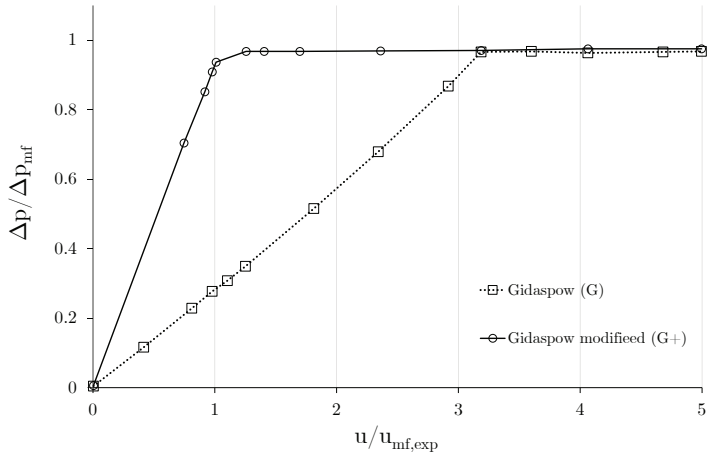

Figure 34 Effect of modified drag model on pressure drop

The turbulence model (k-ε) did not noticeably effect the results. This is in consistence with the findings from Gao et al. [235]. The omission of a turbulence model is common in fluidized bed simulations [198,227,230,236–243]. Thus, the following results were gained from laminar simulations only. However, it should be noted that the inclusion of a turbulence model would not affect the investigated measures in the bubbling-bed zone or fast-bed zone of the COORVED gasifier.

6.3.3 Results

In the following, four measures are evaluated: a) radial voidage profiles, b) axial voidage profiles, c) vertical component of the solids velocity ($u_{s,z}$) on a 2D radial plane, and d) pressure drop fluctuations as an indicator for the type of fluidization.

Radial voidage profiles

The voidage for three different fluidization velocities is compared to experimental findings in Figure 35.

First, it can be seen that there is a poor comparability between numerical and experimental results for u=0.05 m/s. Especially the profile itself and the mean voidage (0.59 vs. 0.77) are different. The simulations show a very flat voidage profile, whilst the experiment has a large gradient for $-0.5<r/R<0.5$. In the experiment, the region close to the wall has a voidage of approx. 0.5. This is around the voidage at minimum fluidization conditions $\varepsilon_{mf}=0.51$ as listed in Table 18. From the present nondimensional groups and the Reh diagram a value around $\varepsilon=0.7$ was expected (see Chapter 6.3.1). It is surprising that a part of the bed seems to be close to minimum fluidization conditions even though $u/u_{mf}=25$.

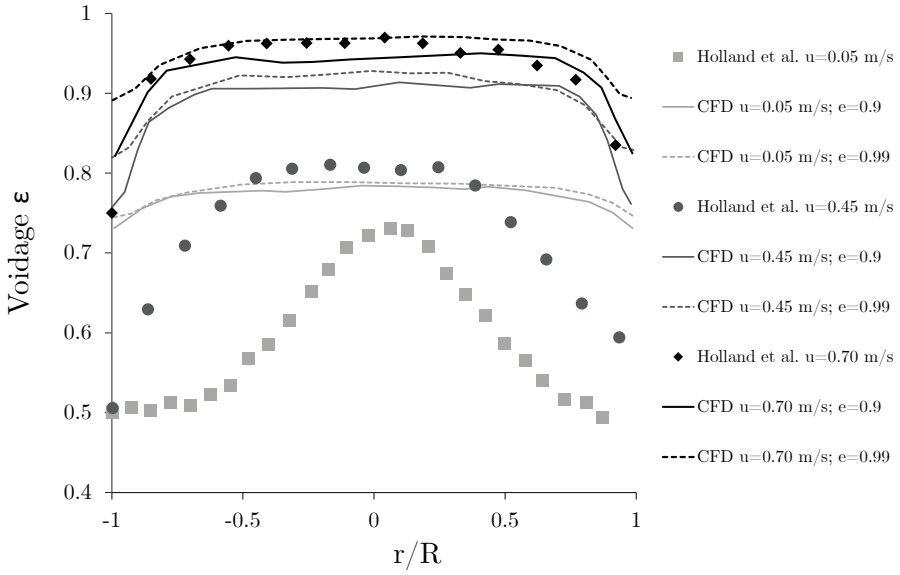

Figure 35 Radial voidage profiles for different gas velocities and restitution coefficients

Thus, the experimental voidage profile for u=0.05 m/s might indicate an issue with the gas distributor glass frit. Obviously, the fluidizing gas is not equally distributed. This becomes even more probable if the reported pressure drop of the frit is considered. For u=0.05 m/s a pressured drop of 100 Pa was given [126]. This is less than 10% of the pressure drop of the bed. Usually, values above 20–30% are required to ensure an equal gas distribution [244,245]. The improperly operating glass frit might result from the porosity of the frit. The pore size was given to be 100–160 µm [126]. With the particles being smaller (d_p=70 µm), plugging of pores is likely. Thus, the differences in the voidage profile between simulation and experiment result from differences in the gas distribution at the bottom. The simulation assumes an equal gas distribution, whilst the experiment might have a pronounced maldistribution. Nevertheless, the simulation shows a higher voidage also in the center of the bed. In so far, it is found that the applied simulation setup slightly overestimates the voidage for bubbling beds. This cannot be attributed to the drag model modification as shown in Appendix 10.3.3. Even though a voidage around ε=0.7 was expected from analyzing the Reh diagram, it must be noted that the numerically determined maximum voidage differs by 30% compared to the experiment (case u=0.05 m/s).

The comparison for u=0.45 m/s shows also deviations between simulation and experiment. Even though the profile is captured very well (qualitative agreement), the mean voidage differs by 17%. The applied numerical setup overestimates the voidage. Again, the adaption of the Ergun model part does not account for an overestimation of the voidage (see Appendix 10.3.3). The expected voidage based in the Reh diagram is 0.8. The same voidage was found during the experiments in the core region. However, considering the lower voidage in the annulus, a mean voidage of 0.76 is found.

The highest agreement between simulation and experiments is found for the highest velocity of u=0.70 m/s. Both the shape of the curve as well as the local voidage and mean voidage compare very well. The mean voidage differs by 1% as both the experiment and the simulation give ε=0.95. Also, from the Reh diagram a voidage around 0.93 can be expected.

Figure 35 shows also the effect of the coefficient of restitution (COR) (see Chapter 3.3.3). It can be seen that there is a negligible effect for low gas velocities and a small effect for higher velocities. For the highest velocity, an increase of COR from e=0.9 to e=0.99 causes the mean voidage to increase by 3%. Wang et al [246] also found a negligible effect of an increased COR for bubbling-bed cases. Also, the slight increase in voidage with an increasing COR has been shown before [198,235]. There seems to be a tendency to apply COR of e=0.9 for bubbling beds [195] and higher values (e=0.95–0.99) for turbulent beds. In general, it can be stated that there is a small sensitivity on COR for the presented simulation cases. It should be noted that other setups, e.g. spouted beds (compare Reza, Laugwitz et al. [197]), have shown to be much more sensitive to this parameter.

Axial voidage profiles and bed surface

In addition to the radial profiles, also axial profiles are evaluated to assess the effect of the COR. Figure 36 shows the voidage profiles for the three different gas velocities and CORs of e=0.9 and e=0.99, respectively. Unfortunately, the experiments did not investigate axial profiles. Again, it can be seen that COR has a negligible effect on the voidage for bubbling beds. Radial profiles were measured at h=0.15 m. At this location, the effect of COR is more pronounced for the case u=0.70 m/s compared to u=0.45 m/s. In the upstream direction, the difference from e=0.9 to e=0.99 becomes negligible for the case u=0.70 m/s. On the other hand, with increasing height there is an increasing deviation for the case u=0.45m/s. For all cases, the bed expansion increases for increased CORs. In addition, an increase in COR causes the bed surface to become more diffuse. This can be seen exemplarily especially well for the case u=0.45 m/s. For e=0.9 the bed surface can be defined somewhere between h=0.1 m and h=0.2 m. For e=0.99 the bed surface cannot be defined clearly anymore.

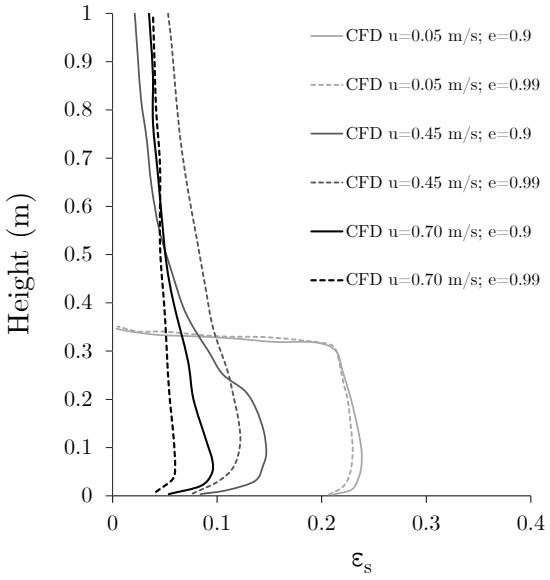

Figure 36 Axial voidage profiles for different gas velocities and restitution coefficients

Velocity profiles

The particle velocity is a very meaningful measure. The strength of the experimental series from Holland et al. [126] for the present validation is the availability of 2D contour plots for the vertical component of the solids velocity ($u_{s,z}$). Figure 37 illustrates the experimental results for the lowest and highest gas velocity. The intermediate velocity was left out for convenience, but can be seen in Appendix 10.3.4.

On the left hand side it can be seen that the particle flow profile is characterized by an up-flowing core and descending particles near the wall. There is a good qualitative agreement for the case u=0.05 m/s between simulation and experiment. However, there are quantitative differences in the dimension of the core region and the achieved velocities. The diameter of the calculated core is 14.8% larger than found in the experiment. The calculated maximum velocity in the core is 17% smaller compared to the experiment. The most significant deviation in all results can be found for the maximum descending velocity in the wall-near region. Here, the simulation predicts only 30% of the maximum velocity compared to the experiment. From the upper left-hand side in Figure 37 the poor gas distribution during the experiment (u=0.05 m/s) can be seen. As explained above, the improper gas inflow is assumed to cause the larger deviation between simulation and experiment for this case. The gas flow through the core is exaggerated in the experiments.

The calculated cases u=0.05 m/s and u=0.70 m/s show some deviations in the symmetry of the results (see lower left and lower middle contour plots in Figure 37). It can be assumed that an increase in averaging period will result in a more symmetric profile. Thus, the lower right hand side shows the numerical results for an averaging period of

40 s for the case u=0.70 m/s. In fact, the symmetry of the results is increased. After 40 s of averaging period, the symmetry is as high as for the experimental case. Comparing the upper and lower right hand side a good agreement between experiment and simulation can be seen. The pronounced core-annular structure agrees very well from a qualitative point of view. Evaluation of a core-annulus flow can be assumed at the high fluidization number of that case (u/u_{mf}=350). In addition the very good qualitative agreement there is also a god quantative agreement between experiment and simulation. The maximum up-flow velocity in the core is overestimated by only 8% in the simulation. The maximum descending velocity in the wall-near region differs also by only 8%. The diameter of the core region is overestimated by the simulation by 20%.

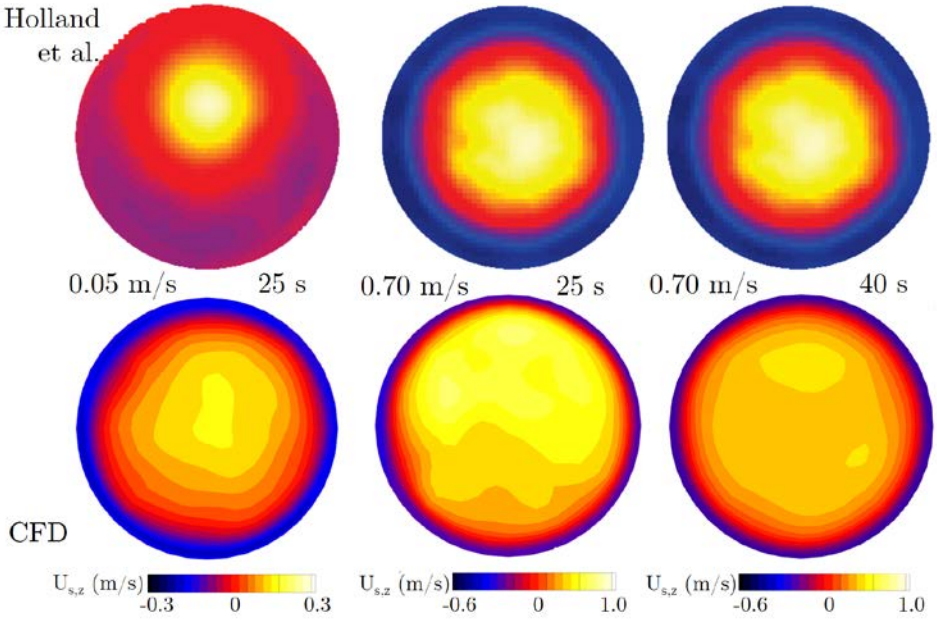

Figure 37 Profile of vertical solids velocity for different gas velocities and averaging periods

In general it was found that the solids velocity profile is a very meaningful measure as it reflects different fluidized-bed phenomenon (e.g. gas-solid drag, gas velocity profile, core-annular structures). The quantitative agreement between simulation and experiment is very good for both analyzed velocities. The quantitative agreement for the case u=0.07 m/s is very good, whilst the bubbling-bed case (u=0.05 m/s) shows larger deviations. Most of the deviations can be attributed to issues in the experimental setup causing an improper gas inflow. Nevertheless, the applied numerical setup is capable of capturing all presumed phenomena correctly at a sufficient accuracy.

Pressure drop fluctuation

So far, the analyzes was conducted at a distinct bubbling-bed case or a turbulent or fast-fluidized bed case. As a next step, the transition between those two shall be investigated. There are two frequently used measures to identify the transition from bubbling bed to

turbulent (compare Figure 7). The pressure drop fluctuation can be analyzed for increasing gas velocities, to identify the onset of turbulent fluidization at u_c and the point at which the turbulence is fully developed u_k (see, Chapter 2.2.2). A less well defined approach is to determine the transition by the onset of dispersion of the fluidized-bed surface. Whilst a bubbling bed exhibits a clear bed surface with a large gradient of solids concentration, the surface of turbulent beds is more diffuse with a smaller gradient. Fortunately, the experiments from Holland et al. [126], provide measurements of the pressure drop fluctuation. In addition, the bed height will be analyzed for different gas velocities in numerical experiments. Experimental measurements were not conducted for the latter approach.

Figure 38 shows the pressure drop fluctuation for different gas velocities. The experimentally determined curve (squares) shows the expected behavior. First, the fluctuations increase until a maximum value is reached at a velocity of $u=u_c=0.3$ m/s. The measured u_c is consistent with calculations from empirical approaches. According to Equation (2.6) and Equation (2.7) an u_c between 0.4 and 0.5 could be expected. After $u=u_c$ was reached, the fluctuations decrease until a constant value is reached at $u=u_k=0.6$ m/s. Thus, from the experiments it is found that the transition from bubbling to turbulent starts at u=0.3 m/s and fully turbulent fluidization is achieved at u=0.6 m/s. Comparing the simulation results, noticeable differences can be seen. Compared to all other evaluated measures, the pressure drop fluctuation is the only measure that shows both quantitative and qualitative differences. For velocities between 0.05 m/s and 0.25 m/s the simulations show a larger increase in p´ compared to the experiment. At u=0.25 m/s the mean calculated fluctuation is 2.4 times higher compared to the experiment

From here, the deviation increases with increasing velocity. In addition, it is difficult to identify a global maximum of the fluctuation followed by a decrease and a plateau as in the experiment. Most simulation cases show a local maximum followed by only a short decrease. After that, all cases show again an increasing fluctuation. The local maxima, however, lie in a feasible range between 0.3 m/s and 0.5 m/s, which is in line with experiments or empirical predictions (Equations (2.6) and (2.7)). Nevertheless, the absolute values of the fluctuation are too high. Moreover, the increase in p´ after u_c was reached is not comprehensible. This phenomenon is independent of the applied COR or formulation for the granular temperature. In addition, different boundary conditions at the gas outlet were tested. The false trend was found for the pressure outlet and the outflow boundary condition. Further work is required to investigate this impairment of the numerical setup in more detail.

To the author's best knowledge, there are no publications, that compare experimentally and numerically retrieved fluctuations of the pressure drop applying the KTGF.

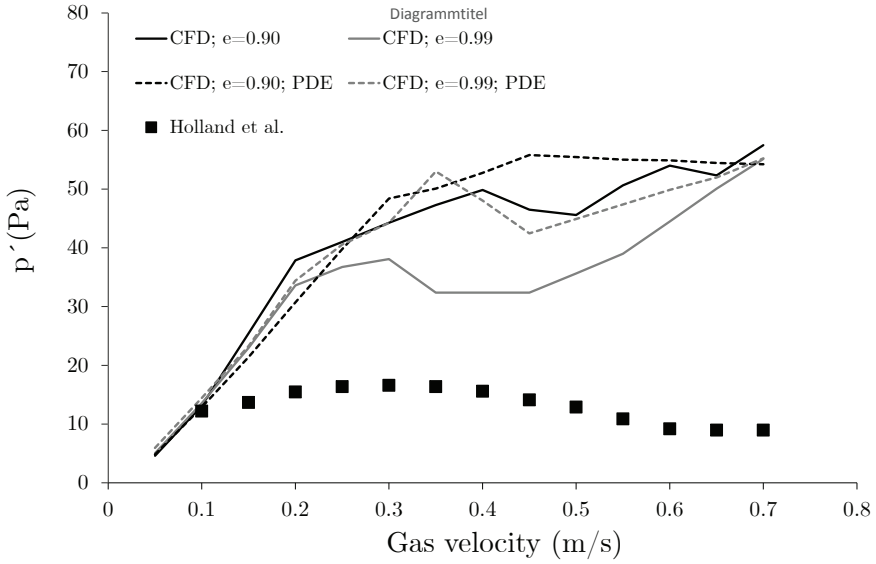

Figure 38 Pressure drop fluctuation as a function of gas velocity for Holland et al. [126] and different simulation settings

In addition, Figure 38 can be used to discuss the effect of COR and the effect of the formulation of the granular temperature (algebraic or PDE). The effect of the simplified algebraic form compared to the PDE calculation (see Chapter 3.3.3) is as expected. For the PDE cases the pressure drop is increased. At a first glance, this might be in contrast to the explanations in Chapter 3.3.3. There, it was stated that the PDE causes reduced granular temperatures and thus reduced velocity fluctuations and thus reduced pressure drop fluctuations. However, it was also mentioned that this trend depends on the applied grid resolution and discretization schemes. As shown by Syamlal and Pannala [157], this trend reverses for grid resolutions with $L_c/d_p>9$. In so far, the increase in pressure drop fluctuation with the PDE setup in the present simulations confirms the findings from Syamlal and Pannala [157].

An increase in COR causes a reduction in pressure drop fluctuations. This is caused by an increased homogeneity in the bed associated with suppressed bubble formation, as also found by others [195,198]. However, even the smaler fluctuations for e=0.99 are still too high to be comparable to the experiment.

After it was found that the numerically predicted pressure drop can hardly be applied to identify the transition from bubbling bed to turbulent bed, an alternative measure need to be found. As discussed above, the fluidized-bed height is a meaningful measure for this. Figure 39 shows the axial voidage profile for different gas velocities. For superficial gas velocities below u=0.30 m/s the bed surface is sharp. For increased velocities, the bed surface becomes more diffuse. At u=0.45, the bed surface can still be pointed between h=0.1 m and h=0.2 m but there is a gradually transition to the freeboard. Thus, from Figure 39 it can be found that the transition occurs between u=0.35 m/s and u=0.45 m/s, which compares very well with experimental and empirical findings.

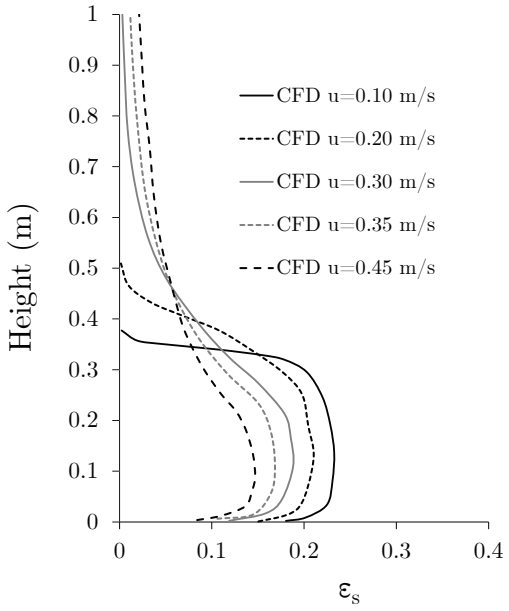

Figure 39 Axial voidage profile for velocities around the transition from bubbling to turbulent

6.3.4 Conclusion

A suitable reference experiment from literature was identified for the validation of the numerical setup for the COORVED simulation. Here, validation focuses on the bubbling-bed zone and fast-bed zone. The suitability of the experiment from Holland et al. [126] was proven by comparing dimensionless groups of the COORVED zones and the different experimental conditions. For this, the Reh diagram was employed. Besides similar hydrodynamic conditions, comprehensive measurement data are provided by the experiment from Holland et al. Thus, the comparison between numerical results and experiments could be based on radial voidage profiles, contour plots of solids velocities and pressure drop fluctuations. In addition, the effect of alternative models (drag model, granular temperature) and parameters (coefficient of restitution) was investigated.

The comparison of results for the bubbling bed case is hampered by a maldistribution of the inflowing gas during the experiment. This is the main reason for differences in the voidage and velocity profiles between simulation and experiments. Nevertheless, the applied setup enables good and very good comparability of numerical and experimental results. The mean voidage differs between 20% (low velocity cases) and 1% (high velocity case). An increase in the coefficient of restitution does barely affect the bubbling-bed case and slightly increases the voidage at higher velocities (3% increase for u=0.70 m/s). The simulation correctly predicts the core-annular structure in the velocity profiles. Larger quantitative differences to the experiments can be found only for the bubbling bed case. Again, the reason is the maldistribution of inflowing gas during the experiment. The diameter of the core is predicted with a deviation between 14.8% and 20% compared to the experiments. The vertical solids velocity in the core is predicted with a deviation

between 17% (bubbling bed case) and 8% (fast bed). The maximum descending velocity in the wall-near region (core) is predicted with a deviation of 8% for the fast-bed case. For the bubbling bed case the deviation is much higher.

Larger deviations were exhibited for the pressure drop fluctuation with increasing gas velocity. There is a large quantitative difference and a qualitative difference in the curve progression. Several modelling setups predicted the same improper behavior. Nevertheless, the numerical setup is capable to identify the transition from bubbling to turbulent correctly, if vertical voidage profiles are analyzed.

The suggested numerical setup can calculate bubbling beds and fast beds with a sufficient accuracy.

6.4 Validation Experiment Jetting Bed

After the numerical setup was validated for bubbling beds and fast beds (Chapter 6.3) the accuracy of the simulation of a jetting bed needs to be investigated. Finally, the numerical setup must be validated for all three fluidized-bed zones (see Figure 20) of the COORVED gasifier. According to a literature survey, only the work from Hensler et al. [116], investigated a hydrodynamic situation comparable to the COORVED lab-scale unit. This refers mainly to the employed jet velocity (compare Chapter 5.3). The background fluidization and the particle properties are different to the COORVED case. The extend of the difference is visualized in Figure 40, by means of the regime diagram from Guo [143] (see Chapter 3.1 and 5.3).

6.4.1 Experimental Setup

In their work, Hensler et al. [116], employ positron emission particle tracking (PEPT) measurement technique to investigate a jetting bed. Results from this non-invasive method are compared to results from a conventional invasive (capacitance probes) method. The presented measures include radial profiles of solids concentration (1-ε) at different heights and an axial 2D contour plot of the solids concentration. From the latter, the jet properties (jet half angle and jet penetration depth) are evaluated and compared to results from empirical correlations.

The most important experimental characteristics are summarized in Table 20.

Table 20 Experimental conditions from Hensler et al. [116]

Property	Value
Material	glass beads
Geldart class	B
d_p	732 µm; a particle of 700 µm was radio-actively labeled as a tracer
ρ_p	2480 kg/m^3
ε_{mf}	not mentioned
$u_{mf,experimental}$	0.31 m/s
Fluidizing conditions	air, ambient
u_{jet}	60 m/s
u_{bg}	0.5 m/s
u_{bg}/u_{mf}	1.6
u_{jet}/u_{mf}	194
D	19.0 cm
D_0	1.0 cm
m_s	30 kg
H_0	0.85 m

From Figure 40, it can be seen that the jet-Froude number (Fr_{jet}) differs by one order of magnitude comparing the Hensler et al. experiment and the COORVED CFD case (see Figure 23 and Table 12). On the other hand, for the other cases (EC1, EC2, EC3, and Reference) there is good comparability of Fr_{jet} with the experiment.

However, the combination of all experimental features as well as the quality of presented measures makes this experiment a suitable reference experiment for validation purposes. For the future, one might identify a jetting-bed experiment with an even more comparable Fr_{jet}, or conduct own experiments.

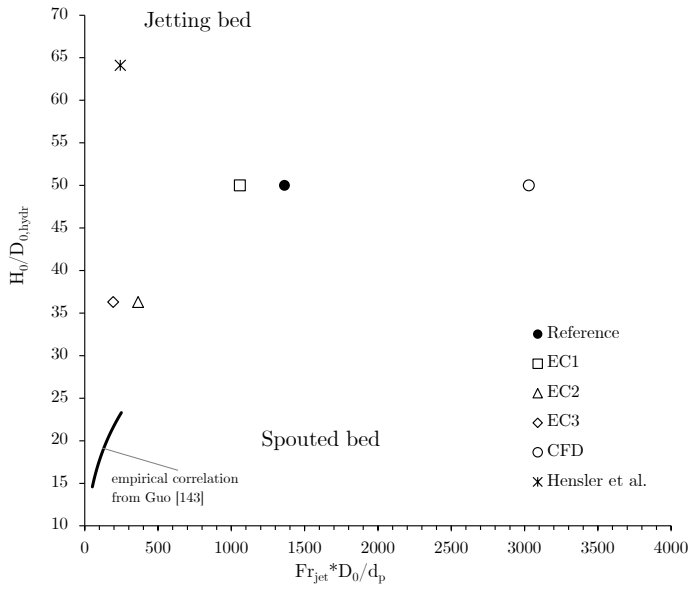

Figure 40 Regime diagram for the COORVED jetting bed and the experiment from Hensler et al. [116].

6.4.2 Simulation Setup

The numerical setup is similar to earlier simulations of the bubbling bed and fast bed (see Table 13 and Table 14). In contrast to the laminar simulations above, here a turbulence model (k-ε) was applied because of the high jet velocity. Moreover, compared to Table 14, the time step size was reduced to 5e-05 s to improve convergence. The computational grid is shown in Figure 41.

It is comprised of 175 k cells with a high resolution in the fast jet region. The mesh features an increasing cell size with increasing reactor height. Thus, the size ratio is between L_z/d_p=10 in the lower section and L_z/d_p=20 in the upper section. This ration is low compared to the ratios applied in Chapter 6.2 and Chapter 6.3. The reason is that a) the particle size (d_p) is noticeably increased and b) the required grid resolution is dominated by the very high gas velocities of the jet rather than the needs in the surrounding bubbling bed.

The simulation was conducted for 40 s of physical time. The last 30 s were used for time averaging and evaluation. After that period the results did not change anymore.

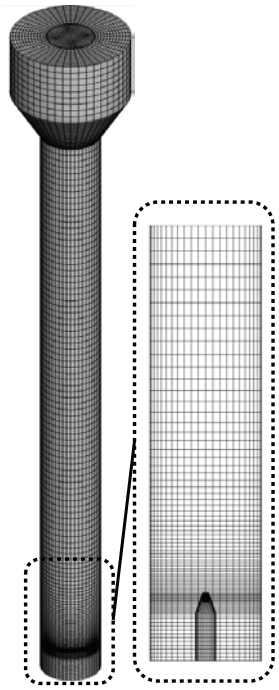

Figure 41 Computational grid for simulation of experiments from Hensler et al. [116], adapted from Schwarzer [247]

6.4.3 Results

Figure 42 shows time averaged contour plots of the mean solids concentration (1-ε) from the experiment (left side) and the simulation (right side). It can be seen that there is a good qualitative agreement. Jet half angle (γ_{jet}) and jet core length ($l_{jet\text{-}core}$) are the first measures to determine quantitative agreement (compare Chapter 2.2.4).

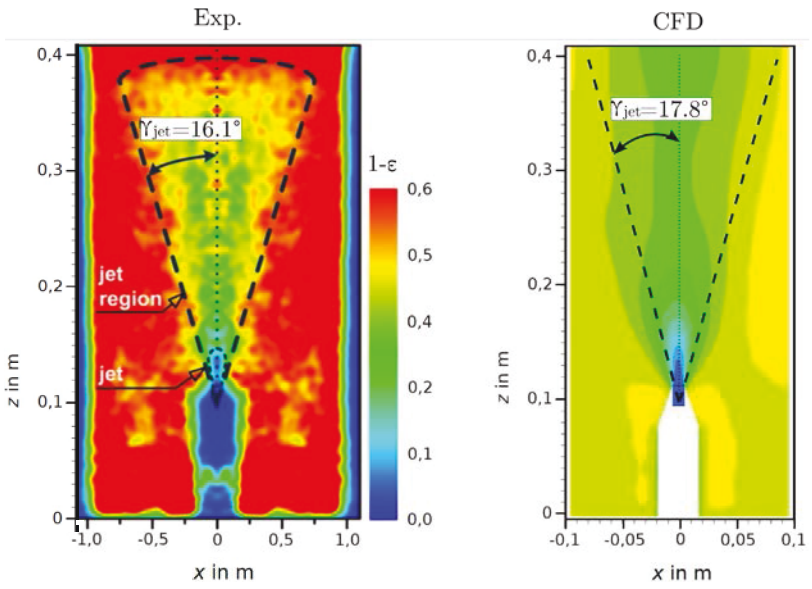

Figure 42 Solids concentration profile from Hensler et al. [116] (left) and CFD (right)

Jet half angle

In Figure 42, the jet half angle is shown to be 17.8°. This value was retrieved from analyzes of the radial gradients of the solids concentration over height. From Figure 43 it can be seen that the jet is not perfectly in line with the axial symmetry line of the reactor. The jet has a slight skewness. Hence, the jet half angle is the mean value from 16.7° and 18.9°. It is expected that the symmetry of the jet can be increased if a longer period would be used for averaging. However, the expected increase in accuracy for this measure is negligible.

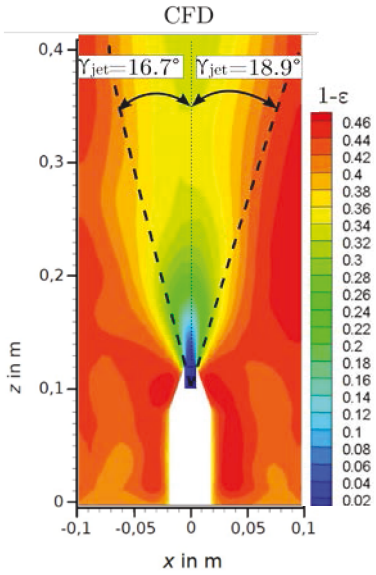

Figure 43 Jet half angle from CFD simulation

The jet half angle of the simulation (17.8) agrees very well with the experimentally determined value (16.1). It should be noted that both values differ noticeably from the empirically derived value of 23.4° according to Merry [113] (compare Table 21).

Jet core length

A poor agreement between simulation and experiment can be found for the length of the particle free jet core ($l_{jet\text{-}core}$). From Figure 44 it can be seen that the simulation predicts a jet core with a length of approx. 14 mm.

In the experiment this value was found to be 25 mm. It should be noted that there is a very fine grid resolution in the jet region (L_z/d_p=1.6). Thus, it is the KTGF models and parameters that cause this large deviation, rather than the grid resolution. On the other hand it can be expected that this deviation does not noticeably effect the remaining hydrodynamic measures. Moreover, this deviation would most certainly not affect the thermo-chemical processes in a respective reactive simulation.

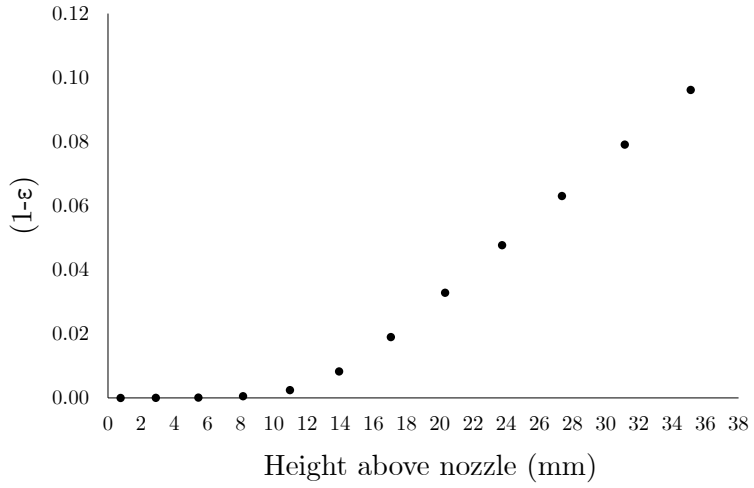

Figure 44 Axial solids concentration profile as a measure for $l_{jet\text{-}core}$

Jet length

Next, the comparability of the jet length (l_{jet}) is investigated. The identification of the jet length from time averaged data might be misleading. From the time averaged CFD results in Figure 42, it seems that the jet penetrates through the surrounding bubbling bed. In the experiment, the jet length is much more clearly defined. From Figure 42 it can be see that the jet does not penetrate through the bubbling bed surface in the experiment. At the upper end of the contour plot, there is a high solids concentration, just as high as in the surrounding bed. It is not clear if the high solids concentration at the upper boarder of the measurement area is a matter of fact or a biased view due to limitation of the measurement technique at the outer rims.

Wang et al. [248] have shown for jetting beds that the jet penetrates through the bed surface for $u_{jet}/u_{mf}>112$. From Table 18, it can be seen that for the experiment from Holland et al. this ratio is 194. Also, Zhong et al. [249] investigated jetting beds of Geldart D particles. They found that the surrounding bed of 3.6 m in height was penetrated by the jet for $u_{jet}/u_{mf}>70$. For the Hensler et al. case, the static bed height was only 0.85 m. Thus, it is likely that the jet could also penetrate the bubbling bed in the setup from Hensler et al.. From this, one might deduce that a more detailed discussion of the upmost part of the measurement area would have been necessary in their publication.

At least for the CFD simulation it can be shown that bubbles are detached from the jet at a certain height ($l_{jet,CFD}$). Those bubbles frequently rise through the bubbling bed, causing a reduced mean voidage over time. Thus, it is not the jet penetrating through the bed in Figure 42 (right side) but frequently rising gas bubbles. Figure 45 shows snapshots from the jetting bed with 0.5 s time increments. From this series it can be seen that the jet flickers around in the bed. In addition it can be seen that the detached bubbles are large and cause a slugging bed above. In their publication, Hensler et al. do

not mentioned if the same phenomenon was observed as well. From Figure 45 it can be seen that the bubbles detach at heights between 0.23 m and 0.27 m. Taking this as the jet length (l_{jet}) gives a good agreement with the experimental findings.

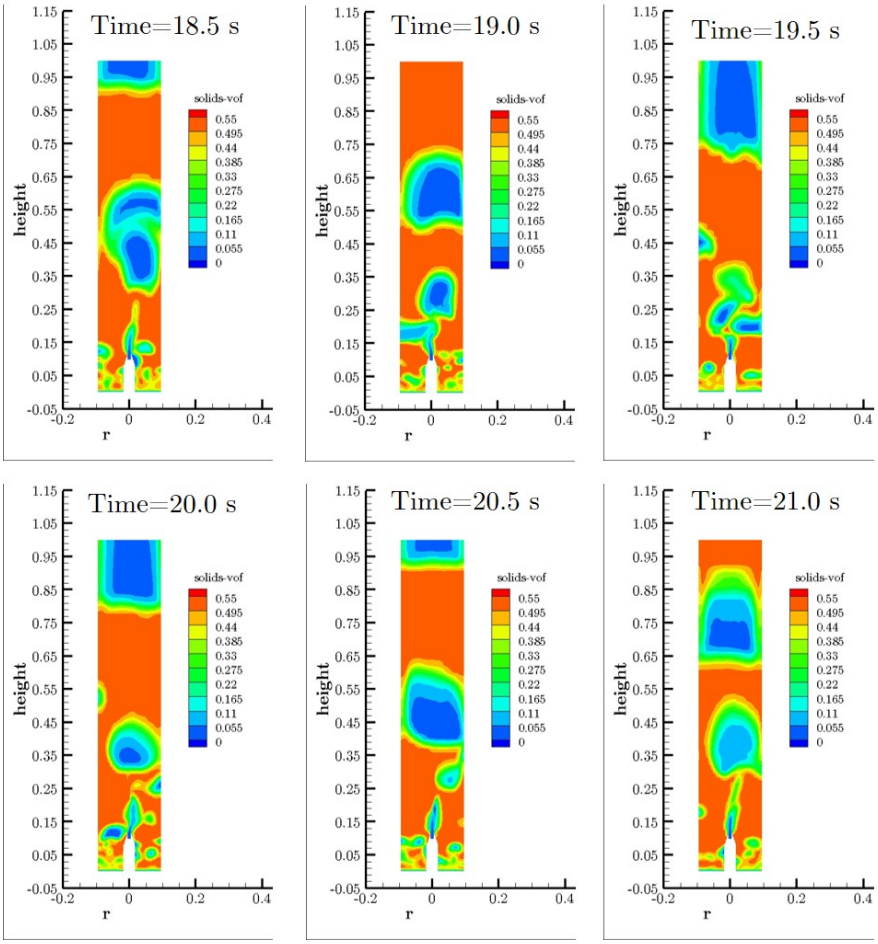

Figure 45 Bubble detachment from gas jet

Table 21 Summary of jet characteristics

Measure	Emp. Correlation, Merry [113]	Exp. Hensler et al. [116]	CFD	Difference Exp. & CFD
Jet half angle (γ_{jet})	23.4°	16.1°	17.8°	10%
Jet core length (l_{jet-}	-	25 mm	14 mm	56%
Jet length (l_{jet})	111 mm	275 mm	225 mm	22%

Solids concentration

As already found in Chapter 6.3.3, the numerical setup tends to slightly overestimate the voidage, especially for low gas velocities (compare Figure 35). This can be seen in the present case as well. The voidage in the surrounding bubbling bed is higher compared to the experiment. From Figure 42, it can be seen that the surrounding bed has a voidage around 0.4, which is comparable to the fixed-bed voidage or the expected voidage at minimum fluidization conditions. This is comprehensible, as the fluidization number is low (u_{bg}/u_{mf}=1.6). In the CFD simulation the voidage in the surrounding ranges from ε=0.5 to ε=0.6. The deviation can be seen even more pronouncedly in radial plots as shown in Figure 46. Here, radial profiles of the solids volume fraction are presented for three different heights above the nozzle (h). It should be noted that the PEPT measurement techniques (Figure 46 a)) shows higher maximum solids concentration in the bubbling bed, compared to the conventional measurement employing capacitive probes (Figure 46 b)). However, the voidage profile does fluctuate much more compared to the profile from capacitive probes. Thus, the mean voidage in the surrounding bed is slightly lower.

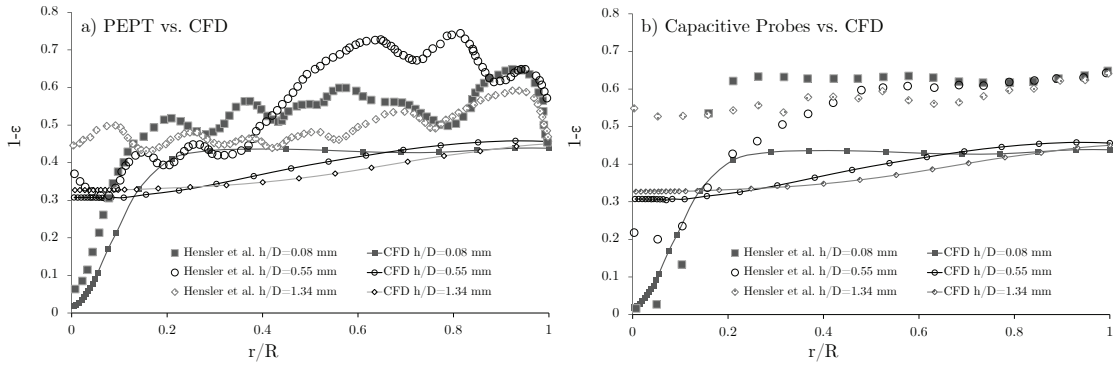

Figure 46 Radial profiles of solids concentration for a) PEPT and b) capacitive probes compared to CFD

However, for h/D=0.08, there is a very good agreement between CFD and both experiments in the jet region. In addition, the jet is captured accurately at a height of h/D=0.55 as well, if compared to PEPT measurements (6% difference). Compared to the capacitive probe measurements, the solids concentration in the jet is overestimated by CFD by 30%. On the other hand, the simulation underestimates the solids concentration in the jet at h/D=1.34 compared to both experiments by 30% and 40% respectively.

The mean solids concentration in the surrounding bubbling bed is underestimated compared to PEPT (25% difference) and capacitive probes (30% difference). A comparable

difference was found earlier for the experiment from Holland et al. [126] as discussed in Chapter 6.3.3. Nevertheless, the applied numerical setup results in a good qualitative agreement with the experimental findings with a sufficient quantitative agreement.

Gas velocity profile

An additional measure to show the reliability of the numerical setup is the development of the gas velocity along the radius. This measure was not investigated experimentally, but the trend should be in accordance with the Tollmien solution (compare Figure 9). The generalizable Tollmien plot shows the gas velocity over radius with a cunning non-dimensionalization. In this way, for ideal cases, the same curve progression can be found for each height. Figure 47 shows the nondimensionalized gas velocity for three measurement heights in the lower part of the jet. It can be seen that the numerical results show the same curve progression at each height. Thus, the first criterion is met very well. For radial positions r/R<0.8, there is a very high comparability between the numerical results and the ideal case. For r/R>0.8 deviations can be seen.

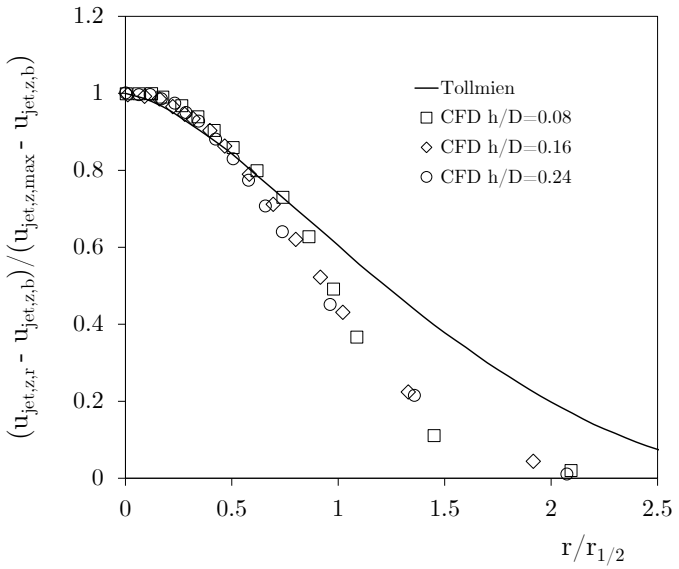

Figure 47 Comparison of ideal Tollmien solution and numerical results

The velocity decreases faster when moving towards the jet boundary compared to the ideal solution. Of course, this measure is sensitive to the chosen jet half angle and the resulting gas velocity at the jet boundary. In addition, this curve is affected by the radial voidage profile. Compared to the experiments, the simulation predicts slightly higher solids concentrations for h/D=0.08 and h/d=0.24 (h/D=0.16 was not regarded in the experimental measurements). This, of course, causes a faster decrease in velocity. In so far, the comparison with the Tollmien solution, reveals that for high velocity jets, a

negligible difference in solids concentration in the jet, might cause larger deviation in the radial velocity profile.

Recirculation cell

The last measure to characterize the jetting bed is the height of the jet-induced recirculation cell. During the course of their work, Hensler et al. evaluated the height and width of the recirculation cell by directional solids flux measurements. From this, it was found that the recirculation cell ranges from the nozzle mouth up to h=27.5 cm above the nozzle mouth. Thus, the height of the recirculation cell is the same as the jet length (l_{jet}) for their experimental configuration. Figure 48 shows the time averaged radial component of the solids velocity.

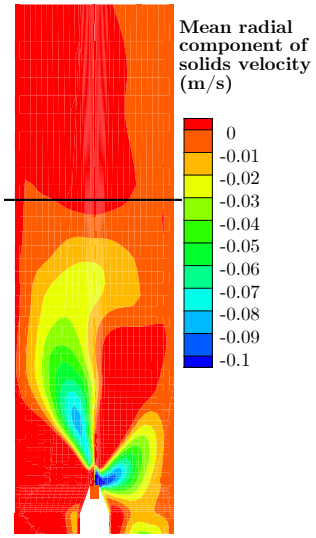

Figure 48 Visualization of numerically predicted recirculation cell in jetting bed experiment

It can be seen that the jet shows an asymmetry. This indicates that an averaging period of 30 s might be too short. The lateral particle movements is also a feasible measure to detect the height of the recirculation cell. It can be seen that from a height of approx. 28.5 cm above the nozzle tip (black horizontal line in Figure 48) there is no lateral solids movement (time-averaged basis). This compares very well with the experimentally determined height.

A last comment is designated to the comparison of the calculated recirculation cell (see above) and the results from a numerical experiment. The latter case neglects the particles in the reactor. It is meant to evaluate the jet and recirculation cell from pure gas phase hydrodynamics. From Figure 49 it can be seen that the gas jet would cause a larger recirculation cell if it was not choked by solids. Without the solids, the recirculation cell would couple back into the lower part of the jet at a height of approx. 100 mm above the nozzle tip. In the jetting bed experiment, the recirculation cell coupled back into the

jet right in front of the nozzle tip. The recirculation cell reaches a height of 515 mm (approx. 2.7 times the reactor diameter) in this numerical experiment.

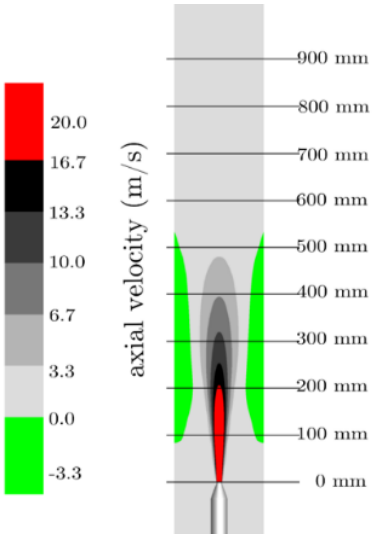

Figure 49 Recirculation cell for gas-phase-only hydrodynamics

6.4.4 Conclusion

The suitability of the experiment from Hensler et al. [116] as a validation case was proven by comparing the Froude number of the COORVED jetting-bed zone and the experimental conditions from Hensler et al. [116]. The comparison between numerical results and experiments could be based on radial profiles of the solids concentration at different heights, 2D contour plots of the solids concentration and the jet geometry (jet height, jet half angle). In addition, profiles of the axial gas velocity along the radius could be compared against the Tollmien solution.

The geometry of the jet is captured accurately. The jet half angle is 10% larger compared to the experiment. The calculated length of the particle free jet core is in poor agreement with the experiment (56% deviation). The calculated jet length deviates by 22% compared to the experiment. The half angle and the jet length from the experiment and the simulation show large deviations to empirically calculated values employing the formula from Merry [113]. Thus, the often-applied correlation from Merry should be used carefully for jetting beds comparable to those from Hensler et al..

The height of the recirculation cell was defined according to the profile of the lateral solids movement. From this measure a cell height of 28.5 cm was deduced. This compares very well with the experimental value of 27.5 cm.

The numerically predicted solids concentration in the lower section of the jet (h/D=0.08) shows very good agreement with results from PEPT measurements and capacitive probe measurements. In the middle section of the jet (h/D=0.55), the CFD results differ by

only 6% compared to the PEPT experiment. The measurements employing capacitive probes show a larger (+30%) solids concentrations in the middle section of the jet. On the other hand, the simulation underestimates the solids concentration in the jet at h/D=1.34 compared to both experiments by 30% and 40% respectively The mean solids concentration in the surrounding bubbling bed is underestimated compared to PEPT (25% difference) and capacitive probes (30% difference). This underestimation was also found earlier for bubbling bed simulations (compare Figure 35).

The nondimensionalized vertical gas velocity shows the same progression at each analyzed height. This is in line with the predictions by the Tollmien solution. However, the velocity, decreases slightly faster compared to the ideal Tollmien solution. This might result from the slight overestimation of the solids concentration in the jet.

The suggested numerical setup can calculate the jetting bed with a sufficient accuracy.

6.5 CFD Simulation COORVED

After the numerical setup was validated for the fluidized-bed zones bubbling bed, fast-bed and jetting bed, it can be employed for a simulation of the COORVED gasifier. In this generic numerical experiment some simplifications are made:

a) Only one particle size is regarded. Thus, formation of agglomerates is neglected. Subsequently, the gas flow through a bottom fixed bed is neglected.
b) Chemical reactions (heterogeneous and homogeneous) are neglected. The axial temperature profile and associated change of gas density and gas viscosity are reflected by isothermal walls (1173 K). Thus, the gas phase temperature is gradually increased with height.
c) The secondary gas enters the domain equally distributed over the bottom, rather than through a secondary lance at the bottom. In the lab-scale unit, the secondary gas will be fanned out by the bottom fixed bed and thus discharge from the fixed bed also equally distributed into the bubbling bed. For this reason, the base fluidization of the bubbling bed is captured accurately with the applied boundary approach.

All simplifications are made to reduce the computational time. Each additionally incorporated phenomenon needs a model validation beforehand.

At this stage, the evaluation of the simulations focuses on phenomenological aspects. That is, to prove the existence of the different fluidization zones and to estimate voidage profiles, velocity profiles, and the shape of the recirculation cell.

6.5.1 Computational Grid

The lab-scale reactor is discretized by means of a hybrid mesh (see Figure 50 a)) with 800 k cells. Only a small area is discretized with tetrahedral cells. Most of the grid consist of an O-grid structure. Details of the mesh can be seen on a axial and radial slice from Figure 50 b) and c).

In the bubbling bed region the grid is coarser compared to the fast-bed region. The finest grid can be found in the jet region. With respect to a particle of d_p=95 µm, the following cell size ratios (L_z/d_p) are achieved: 14, 37 and 64 respectively. Hence, the quality of the mesh is designated to the needs in the fast jet area.

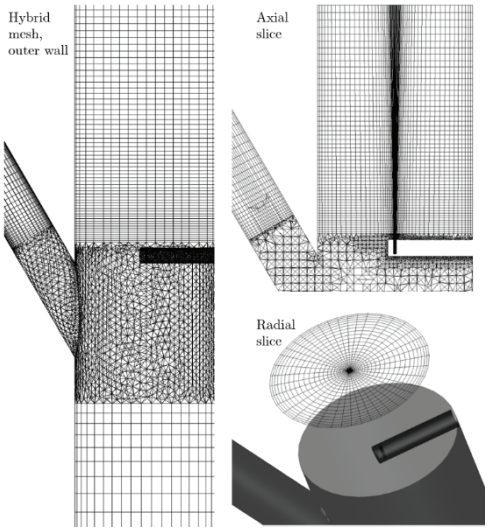

Figure 50 Details of the COORVED mesh, a) outer wall, b) axial slice, c) radial slice

6.5.2 Cold Flow, Single Phase Jet

The gas phase flow was experimentally investigated by means of PIV measurements. As explained in Schimpke et al. [205], the original lance from the lab-scale COORVED gasifier, was applied in an acrylic glass cylinder. The gas flow boundary conditions were set according to the CFD case from Table 12 and Figure 23. The experiment was designated to investigate the gas phase flow only. Thus, no solids were present in the experimental setup. Titanium monoxide was used as a tracer particle to visualize the gas velocity. The simulation was stationary with a second order spatial discretization and a SIMPLE algorithm for pressure-velocity-coupling [220]. Different turbulence models were tested (k-ε; realizable k-ε and k-ω SST). The differences between the results were small, thus results are shown for the k-ε simulation. Figure 51 shows axial profiles of the velocity magnitude at three radial positions (r=0.5 mm, r=14.8 mm and r=30.1 mm) There is a very good comparability to the experimentally determined velocity profile. Thus, the computational grid is of sufficient accuracy.

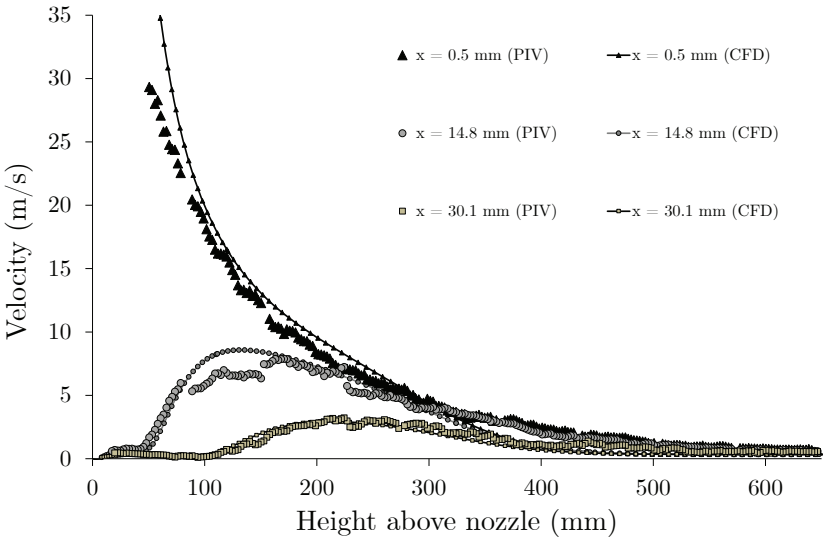

Figure 51 Velocity profiles in axial direction at different radial positions, adapted from Schimpke et al. [205]

If the gas jet is not affected by a solids phase, the recirculation cell would be developed according to Figure 52.

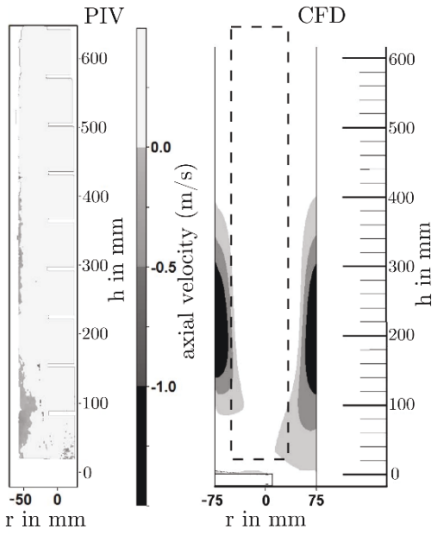

Figure 52 Recirculation cell for gas phase only flow, adapted from Schimpke et al. [205]

The cell would reach from the primary gas lance to a height of 400 mm, which is approx. 2.7 times the reactor diameter. A comparable ratio between cell height and reactor diameter was found in the numerical experiment for the jetting bed setup from Hensler et al. [116] (see Figure 48). Also for the shape and size of the recirculation cell, there is a very good agreement between simulation and experiment [205].

6.5.3 CFD setup

The simulation of the COORVED lab-scale gasifier was accomplished by means of the TFM and the KTGF. The numerical setup is the same as for earlier simulations in Chapter 6.3 and Chapter 6.4 (see Table 13 and Table 14). The grid was approved to be of adequate resolution by comparing velocity profiles of the fast gas jet with experimental PIV data (compare Chapter 6.5.2 and Schimpke et al. [205]). The model setup was validated against bubbling-bed and fast-bed experiments (compare Chapter 6.4), as well as jetting-bed experiments (compare Chapter 6.4). Time averaging started after a comparably long period that the system needed to be in quasi-steady-state. After that, averaging was conducted for 10 s

6.5.4 Results

First, the voidage and velocity profiles in the bubbling bed and the jetting bed are investigated. Subsequently, the jetting bed is investigated.

Bubbling bed and fast bed

The measurement positions can be seen from Figure 53. Radial profiles and contour plots of the bubbling bed are retrieved 60 cm above the bottom gas inlet. The fast bed is analyzed at a distance of 110 cm above the primary gas injection. For both areas it is assumed that they are not affected by the fast central gas jet. The voidage curves are gained along the lines shown in the contour plots from Figure 55.

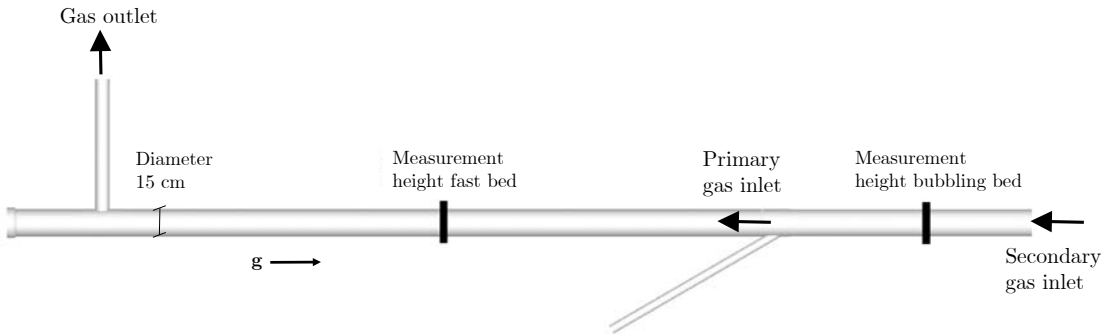

Figure 53 Measurement heights for the COORVED gasifier

The respective profiles show the expected behavior. As seen from Figure 54, the bubbling bed has a mean voidage of approx. 0.75. This compares very well with the expectations gained from the analyses of the Reh regime diagram (compare Figure 23). Moreover, it compares very well with the findings from the simulation of a hydrodynamically comparable setup in Chapter 6.3.3 (see Figure 35). With regard to a particle of 150 µm, the bubbling bed zone exhibits a high expended bubbling bed associated with a comparably high voidage. Of course the voidage is even higher in the fast-bed zone. Here, the mean

value is ε=0.96. As expected, both measurement heights feature an increase in solids concentration close to the wall.

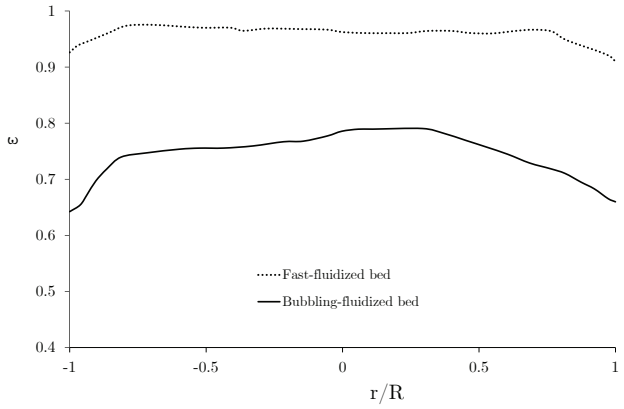

Figure 54 Time averaged radial voidage profile for two measurement heights from the COORVED CFD simulation

This behavior is closely related to the radial gas velocity profile with a no-slip condition at the wall. Another consequence from this conditions is the solids velocity profile. In line with the visualization approach from Figure 37, contour plots of the vertical component of the solids velocity are given in Figure 55. First, it can be seen that an averaging period of 10 s causes asymmetric profiles. In Chapter 6.3.3, it was already discussed that an averaging period of 40 s is required to gain symmetric results for this very measure. However, the trends can be seen. The bubbling-bed zone (left side) has an equally distributed velocity profile, with a thin annular region of descending particles. Descending velocities are small compared to the fast bed. In the fast-bed zone, there is a more pronouncedly core-annular structure. The annular region is wider with a width of approx. 2.5 cm. The velocity profile has a steeper increase compared to the bubbling bed.

From the solids volume fraction profiles in Figure 56 it can be seen that the solids are not equally distributed over the radius in the fast-bed zone (right-hand side). The solids tend to travel in strands or clusters, rather than isolated from each other. That phenomenon can be expected for fast-fluidized beds as explained in Chapter 2.2.3. Thus, the numerical setup is capable to predict the strand formation as a feature in the hydrodynamics of the COORVED reactor. In the bubbling-bed zone, the particles are more equally distributed, even though the formation of bubbles can be seen. Nevertheless, there is a certain homogeneity in the emulsion phase surrounding the bubbles.

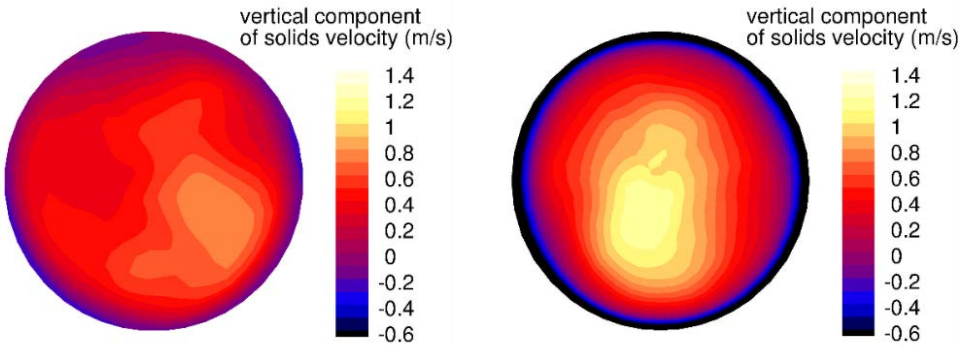

Figure 55 Time averaged velocity in bubbling-bed zone (left) and fast-bed zone (right)

The bubbling behavior was already anticipated from the position of the zone in the Reh diagram (see Figure 23) and from calculating the Froude number (Fr) at this zone to be approx. 42. In Chapter 3.1, it was explained that bubble formation is likely for Fr>0.13. In addition, it is possible to tell that the bubbling-bed zone is not under turbulent-bed conditions from analyzing the critical velocity (u_c) as explained in Chapter 2.2.2. Applying Equation (2.6), a critical velocity of 0.87 m/s can be calculated. This is more than three times the velocity found in the bubbling-bed zone.

In general, it was found that the CFD simulation of the bubbling-bed zone and the fast-bed zone shows reasonable and plausible results. Thus, the design and experimental boundary conditions fulfill the required and patented claims.

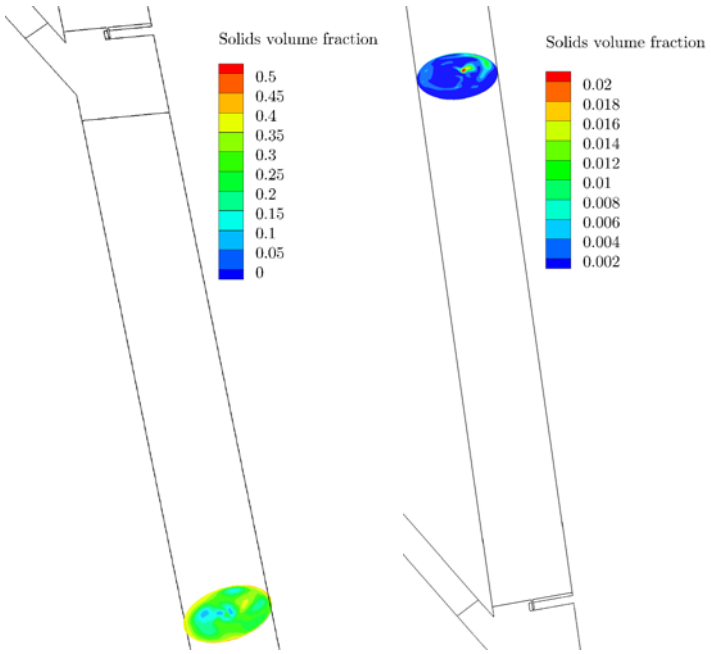

Figure 56 Snapshot of solids volume fraction in bubbling-bed (left) and fast-bed (right)

Jetting bed

The jetting-bed zone is the most complex zone in the gasifier from both a hydrodynamic perspective and a chemical perspective. The COORVED design claims a lean central jet surrounded by a denser annular zone of descending particles. From **Figure 57** it can be seen that the lean core (ε>0.9) is surrounded by a denser zone. The dense annular region features a higher solids volume fraction of ε_s>0.4 up to a height of 25 cm above the lance and ε_s>0.3 up to a height of 45 cm. The mean solids concentration in the annular region is even slightly increased compared to the bubbling-bed zone. From this, the protection of the wall from flame radiation (in a reactive case) by the solids can be expected. Thus, the numerical results provide evidence for the feasibility of the COORVED design.

The diameter of the region close to the wall in which the particles descend is as small as in the fast-bed zone (compare **Figure 58** to Figure 55 right). Thus, the solids backmixing in the jetting zone is not noticeably increased by the jet compared the fast bed or bubbling bed.

The height and shape of the recirculation cell cannot be evaluated after 10 s of averaging time. In **Figure 59**, the time averaged solids velocity in negative x-direction can be seen.

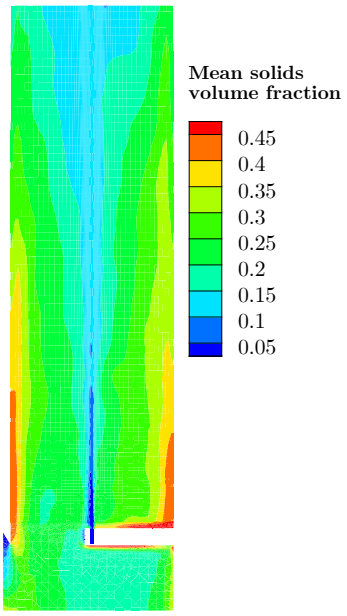

Figure 57 Time averaged solids volume fraction in the jetting zone of the COORVED gasifier

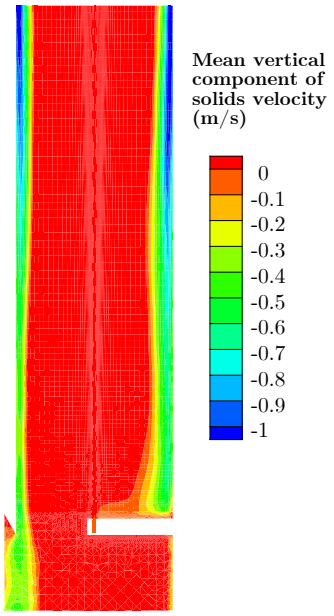

Figure 58 Time averaged area of descending solids in the jetting zone

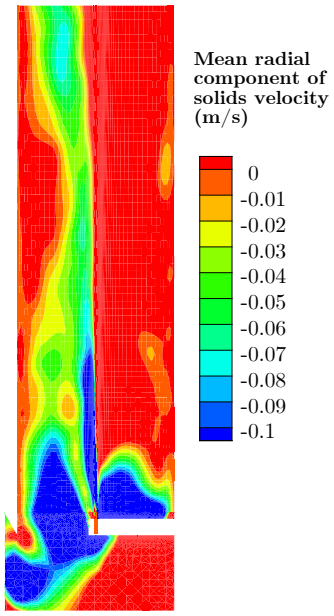

Figure 59 Time averaged solids recirculation pattern in jetting zone

It becomes obvious that there is no smoothly developed recirculation cell. Thus, solids recirculation is not as well defined as expected. Moreover, it can be seen how the primary

gas lance disturbs the recirculation noticeably. Theoretically, the height of the recirculation cell could be gained from the maximum height at which solids travel permanently (time-averaged) in radial direction.

Unfortunately, there is not a clear height at which the radial velocity component of the solids suddenly decreases. The radial velocity decreases only slowly with height. If one might use the position along the central axis with the highest gradient of the radial solids velocity (color change from dark blue to light blue in Figure 59) the identified height would be 17.6 cm. This value could be taken as the height of the recirculation cell.

6.5.5 Conclusion

The hydrodynamics of the COORVED gasifier have been calculated in a hybrid mesh of 800 k cell, providing the required cell-to-particle size ratio that has been identified in Chapter 6.2. The quality of the grid is especially critical in the central, fast jet area. The good quality of the grid was proved by simulating a particle free case. The predicted jet velocity profiles compares very well will the according experimental value from PIV measurements. Thus, the grid meets the requirements of both, TFM modelling and high velocity simulations.

For the simulation of the gas-particle hydrodynamics it was found that the bubbling bed and fast bed emerge just as expected. The calculated bubbling bed zone has a mean voidage of ε=0.8. This is in very good agreement with the findings from the Reh diagram. The mean voidage in the fast bed is approx. 0.96, which is a reasonable value for fast beds. Also, the voidage in both zones compares very well with the results from the simulations in Chapter 6.3 (experiment from Holland et al. [126]). Moreover, the core-annulus structure of the COORVED fast-bed zone is well comparable to the calculated case (u=0.7 m/s) from the Holland et al. experiment. This was already expected from comparing the two systems in the Reh diagram (see Figure 32). Finally, it was shown that the simulation setup can capture the formation of strands in fast beds.

In general, the results show that the design and defined inflow boundary conditions for experimental COORVED operation were done feasibly. It should be noted that the specification of a mean voidage (in radial direction) in the jetting bed and the fast bed might be misleading. By averaging one erases the distinct inhomogeneity in particle distribution (strands, core-annulus structure, lean jet).

The jetting zone features a lean core and denser annulus region. The simulation predicts a solids volume fraction in the area surrounding the jet of ε_s>0.4. From this, it can be expected that the wall will be protected from flame radiation. Again, the simulation reveals that the design of the COORVED unit is suitable. However, the height and shape of the recirculation cell could hardly be defined as the cell blurs out at its top.

Even though averaging might cause some loss of information, as explained above, the hydrodynamics can be summarized by visualizing the axial voidage profile of the COORVED CFD case in Figure 60. The lower part is under bubbling-bed conditions with a solids volume fraction around 0.25. The highest solids concentration can be found around the injection point of the primary gasification agent. Here, the solids volume fraction reaches 0.3. Finally, a lean fast bed can be seen in the upmost area.

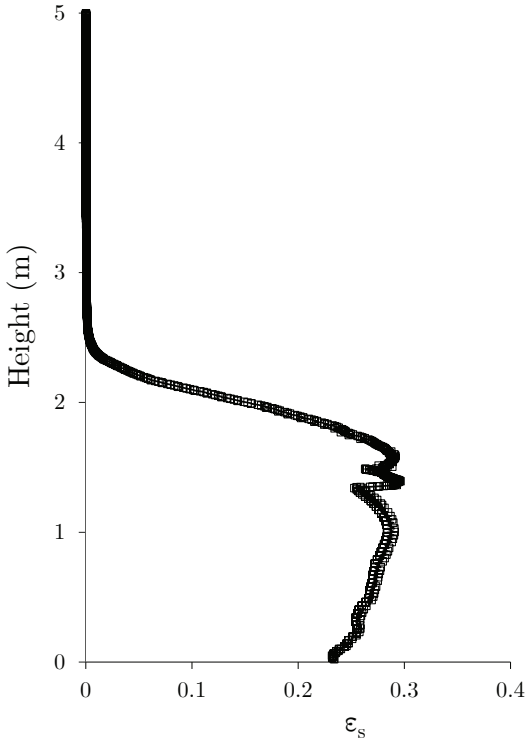

Figure 60 Axial voidage profile for COORVED CFD simulation

7 ASPEN Plus® Simulation of the COORVED Gasifier

As discussed in Chapter 3.2, one dimensional flow sheet simulations of the hydrodynamics can also provide insights into the flow conditions of the COORVED reactor. The development of the simulation setup requires less definitions for models and parameters compared to CFD simulations and computational times are in the order of seconds. Nevertheless, a validation of the retrieved results is mandatory. For this reason, again the experiment from Holland et al. [126] is calculated. Results are shown in Chapter 7.1. Subsequently, the COORVED reactor is calculated in Chapter 7.2.

The effort for simulation setup is much smaller compared to setting up a 3D simulation employing a TFM model and the KTGF. Besides the common boundary conditions (reactor geometry, properties of inflowing gases, solids properties) only a few additional information have to be defined in the ASPEN Plus® environment. Those are the solids holdup or the pressure drop of the fluidized bed, the pressure drop over the gas distributor, the voidage at the point of incipient fluidization (ε_{mf}) and the minimum fluidization velocity (u_{mf}). This information can be based on experimental findings or empirical correlations. Finally, only two models need to be defined. One for the transport disengagement height (zone above the dense bed with a decay in solids concentration until a constant concentration is reached) and an elutriation (solids entrainment) model.

It is interesting to note that the ASPEN Plus® calculation allows for investigating the "jetting" area above the gas distributor. As mentioned in Chapter 2.2.4, there is a small zone above the distributor (1-5 cm in height) that is governed by the tiny jets emerging from the gas distributor. Thus, this zone has a comparably high voidage. The axial voidage plots generated by ASPEN Plus® allow for the evaluation of this small zone. However, this measure is not of interest for this work and is omitted during the evaluation and discussion of the results.

7.1 Validation Experiment Bubbling Bed and Fast Bed

The experimental setup from Holland et al. [126] was employed for validation purposes. This experiment was already discussed in Chapter 6.3.1 and applied as a validation experiment for the CFD setup. Input values for the boundary conditions and minimum fluidization conditions are taken from Table 18 in Chapter 6.3.1.

It should be noted that the experiment focused on radial voidage profiles and 2D contour plots of the solids velocity. Both measures cannot be gained from the 1D approach in ASPEN Plus®. Thus, the only measure that can be compared between ASPEN Plus® and the experiment is the mean voidage for different velocities.

In a sensitivity analysis, the following parameters were evaluated whether they affect the results: applied values for ε_{mf} and u_{mf}, the applied model for transport disengagement height and elutriation. It was found that only the value for ε_{mf} affected the mean voidage at the measurement position. Other parameters affected only the "jetting" zone above the distributor and the decay of solids concentration in the transport disengaging height are affected. However, those areas are not in the focus of the present investigation.

Table 22 compares the mean voidage at the respective measurement height between the experiment, the expected value from the Reh diagram (see Figure 32), the CFD simulation (see Figure 35) and the ASPEN Plus® simulation. Two different values for ε_{mf} are shown in Table 22. The experimentally determined value of 0.51 and a more common value for FCC catalysts of 0.4

Table 22 Comparison of mean voidage between experiment and simulation approaches

Mean voidage	**Experiment [126]**	**Reh diagram**	**CFD**	**ASPEN Plus® ε_{mf}=0.51**	**ASPEN Plus® ε_{mf}=0.4**
u=0.05 m/s	0.59	0.7	0.77	0.65	0.57
u=0.45	0.76	0.8	0.89	0.84	0.81
u=0.70 m/s	0.95	0.93	0.95	0.90	0.87

It can be seen that the ASPEN Plus® simulation predicts a lower voidage compared to CFD and the Reh diagram. With decreasing ε_{mf}, the predicted voidage decreases as well. There is a qualitative agreement that an increase in superficial gas velocity results in an increased voidage. Compared to the CFD results, the deviation is between 6% and 18% for the different velocities and ε_{mf}=0.51. The largest deviation can be found for the case u=0.05 m/s. Compared to the experimental results, the deviation is between 7% and 11%. Again, the largest deviation is found for u=0.05 m/s. The doubts on this experimental point was already discussed in Chapter 6.3.3.

Besides the mean values, also axial plots of the solids concentration can be gained from the simulation approaches. Figure 61 compares the profiles retrieved from ASPEN Plus® simulations (applying ε_{mf}=0.51) and from CFD simulations.

There is very good quantitative agreement for the two higher velocities. For the lowest velocity, some deviations can be seen. The dense bottom region has a higher solids volume fraction and consequently the height of the dense bottom region is lower in the ASPEN Plus® calculation. Moreover, the bed surface is not as sharp as in the CFD case. Nevertheless, the results are reliable.

In general, it is found that the results from ASPEN Plus® are plausible and in a good quantitative agreement with the other approaches. The validation was successful. The ASPEN Plus® setup can be applied to the COORVED gasifier in the following.

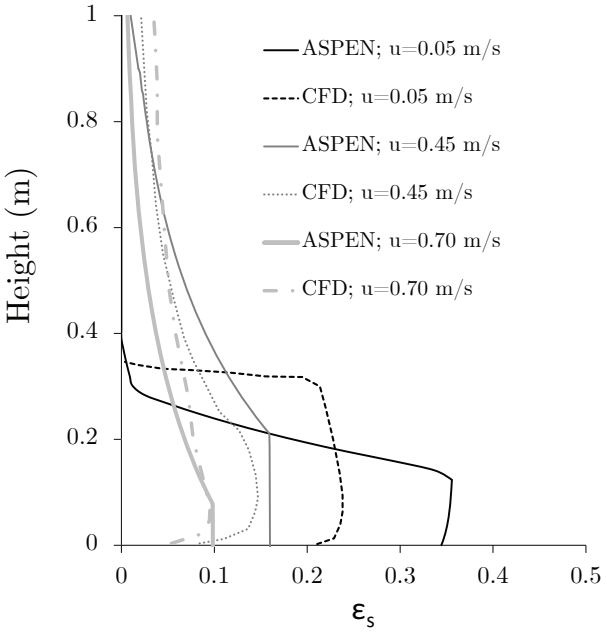

Figure 61 Solids volume fraction, comparison between CFD and ASPEN Plus®

7.2 COORVED Simulation

The validated setup from ASPEN Plus® is applied to calculate the COORVED CFD case (compare Table 12). From Figure 62 it can be seen that the secondary gas results in a bubbling bed in the bubbling-bed zone. The profiles of the solids volume fraction in the bubbling bed zone show a very high comparability between CFD and ASPEN Plus®. In both cases a mean value around ε_s=0.25 can be found. The CFD simulation predicts a slightly higher value. At the height of the primary gas injection, some deviations can be found.

The ASPEN Plus® simulation predicts a sudden decrease in solids volume fraction. This is because the 1D approach cannot capture the lean core and dense annulus region nor the development of the jet and jet angle. In a 1D approach the primary gas is instantaneously distributed equally over the reactor diameter. Above that injection, a short region of constant solids volume fraction (ε_s=0.10) can be seen, After that the solids volume fraction decays in the transport disengaging height. However, the decay is very similar to the decay predicted by the CFD simulation.

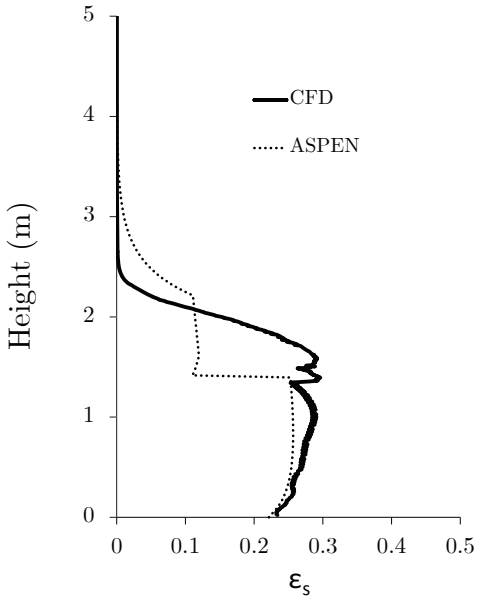

Figure 62 Comparison of results from ASPEN and CFD for the COORVED case

7.3 Conclusion

The ASPEN Plus® 1D approach was successfully validated against the experiments from Holland et al. [126]. The predicted mean voidage compares well with experimental results and results from CFD simulations. The deviation is between 7 % and 11% with respect to the experiments and between 6% and 18% with respect to CFD.

Subsequently, the validated setup was applied to calculate the COORVED reactor. The "CFD" case from Table 12 was chosen because for that case the results from ASPEN Plus® can be compared to results from the respective CFD simulation. The agreement is very good. The profiles of the solids volume fraction in both the bubbling-bed zone and the fast-bed zone differ by less than 10%. The only difference can be found in the jetting region. The 1D approach from ASPEN Plus® cannot capture the radial profile of velocity and voidage. Thus, a sudden decrease of solids concentration is predicted by the ASPEN Plus® simulation.

The ASPEN Plus® simulation tool allows a quick and reliable assessment of the hydrodynamics in the bubbling-bed zone and the fast-bed zone of the COORVED gasifier. The jetting-bed zone should not be evaluated by means of the underlying 1D approach.

8 Summary

Coal gasification

Coal gasification has seen a drastic increase in market volume over the last decade. A lot of R&D activities are designated to improve commercial gasifiers and to develop new reactors. On the one hand, production costs shall be reduced by e.g. increasing the single unit capacity, reduce equipment costs and operational costs. On the other hand, some developments are designated to enable low-quality fuels (e.g. waste, ash-rich coal) to be gasified. Currently, there is no gasifier available, that can convert high-ash coal fines into a high quality raw gas at feasible costs. Fixed-bed gasifier cannot apply fines in the feedstock. Fluidized-beds achieve an incomplete carbon conversion only and entrained flow gasifier have noticeable thermodynamic disadvantages if high-ash coals are fed.

In a thermodynamic analyses it was shown that process temperatures around 1100°C are most reasonable for gasification of high-ash coals [2,23]. From this, the task to develop a fluidized-bed gasifier with complete carbon conversion was deduced. The patented [22] COORVED staged fluidized-bed gasifier features an internal post gasification of ash agglomerates. Thus, complete carbon conversion is achieved in one reaction chamber at raw gas outlet temperatures between 1000°C and 1100°C.

New gasifier

The gasifier is composed of three stages of fluidized beds and a fixed bed at the bottom. The main reaction zone is in the middle section of the reactor. Primary gasification agent is fed via nozzles to form an oxygen-rich central, flame-like jet. Thus, a jetting fluidized bed emerges. Above, after the jet has vanished into the surrounding, a fast-fluidized bed emerges as additional gas from solids conversion causes a high gas flow rate. Below the jetting bed, the gas flow rate is moderate resulting in a bubbling bed.

In the main reaction zone (jetting bed and fast bed) temperatures allow for solids agglomeration if the particles have reached a certain carbon conversion. The agglomerates fall down to the bottom and form a fixed bed. Secondary gasification agent is fed from below in order to convert the remaining carbon in the agglomerates. Carbon-free ash agglomerates can be discharged at the very bottom. The raw gas leaves the reactor at the top.

Fluidized beds

The nature and appearance of bubbling beds and especially of fast beds and jetting beds was discussed in detail, based on an extended literature review. It was shown, which

types of measures need to be applied to describe different bed types. Commonly, pressure drop, pressure drop fluctuation, voidage (mean value and profiles), and particle velocity (mean value and profiles) are used to characterize bubbling beds and fast beds. Additionally applied measures for jetting beds are the jet half angle, the jet length and the velocity distribution along the jet.

Different empirical correlations can be found for each measure. It was analyzed that the accuracy at which the different measures of the different bed types can be calculated with the different empirical equations is low. Deviations of up to 30–40% are common.

Flow regime maps for fluidized beds

Different 0D flow regime maps were compared in their capabilities to capture the expected phenomena in the COORVED gasifier. The diagram from Reh [24] was identified to be most comprehensive to capture the bubbling-bed zone and fast-bed zone in the COORVED gasifier. The required nondimensional groups to set up the diagram were introduced. Consequently, the effect of different flow boundary conditions and particle size on the hydrodynamic behavior was visualized in the Reh diagram. It was found that the reference case (design case for the lab-scale unit) and the CFD case (boundary condition from the patent) are very likely to result in the desired hydrodynamics bubbling-bed and fast-bed in the respective zones.

Because the Reh diagram cannot reflect jetting behavior, other regime maps were introduced, that show the demarcation between spouting and jetting. Here, it was found that a comprehensive regime map that can be applied to different boundary conditions (gas velocity, particle properties) over a wide range is missing. Nevertheless, in the extrapolated diagram from Guo et al [143] it could be shown, that a jetting bed is much more likely than a spouted bed in the jetting-bed zone on the COORVED gasifier.

Comprehensive CFD modeling

The main part of the work was designated to develop a comprehensive CFD setup that can accurately capture the bubbling-bed zone, jetting zone, and fast-bed zone of the COORVED gasifier.

An extended literature review showed that, amongst the different potential numerical approaches, the Two-Fluid Model (TFM) in conjunction with the Kinetic Theory of Granular Flow (KTGF) is frequently applied to gas-solid multiphase flow. The so called Euler-Euler approach can feasibly calculate lab-scale-size equipment and industrial-scale equipment. Commonly applied models and parameters within the KTGF framework and their sensitivity have been discussed. From this, a promising model setup was suggested and applied.

Verification of the CFD setup

An extended verification and validation of the numerical setup was conducted.

Verification focused on prediction of the pressure drop at different gas velocities below and above minimum fluidization. For different mono-dispersed particle sizes and gas properties, the CFD solution compared very well with empirical and analytical solutions.

After that, the required minimal grid resolution was investigated. It was shown that cell size to particle size between 50 and 100 are enough to accurately predict the measures of interest (pressure drop, voidage profiles, and velocity profiles).

Furthermore, it was shown that the transient simulations should be averaged at least over 25 s for evaluation. The initial 5 s must not be considered for evaluation. Thus, at least 30 s of flow time need to be calculated.

Validation of the CFD setup

After verification, it was discussed how suitable validation experiments can be identified. It is necessary to compare nondimensional groups to prove that the systems are similar in their hydrodynamics. For this, flow regime diagrams have been employed. In addition, comprehensive measures should be evaluated in the validation experiment. Those could include, pressure drop fluctuations, radial and axial profiles of voidage or velocity. From a literature survey, two suitable validation experiments have been identified.

CFD simulation of bubbling beds and fast beds

The experiment from Holland et al. [126] investigated fluidization under both bubbling-bed conditions and fast-bed conditions. After simulating the respective three experimental points with different model setups, several measures could be compared.

The mean voidage differs between 20% and 1%. The coefficient of restitution had a minor effect (5-3%) on the voidage profile in each case. The calculated voidage is also in very good agreement with the predictions in the Reh diagram.

The simulation could correctly predict the distinct core-annulus structure of the flow. Thus, the qualitative agreement with the experiment is very good. Core diameter and solids velocity profile deviated by approx. 18% and 12%, respectively as averages over the three cases. The case with the lowest gas velocity (u=0.05 m/s) showed always the largest deviations. It was discussed, that this experimental case might have some weak points in the uniform distribution of gas inflow.

The calculated bed height at different inflow velocities was evaluated. From this, the same critical velocity (u_c) to identify the onset of turbulent fluidization was found as in

the experiment. However, the experiment applied a pressure fluctuation measurement to determine u_c . The numerically predicted pressure fluctuations do not agree with the experiment. This measure is the only one that shows quantitative and qualitative disagreement with the experiment. In contrast to the expectation and the experimental findings, the simulation predicts an increase in pressure fluctuation for increasing velocities above u_c.

A generally applicable numerical setup was identified, that can predict the behavior of bubbling beds and fast beds at a reasonable accuracy.

CFD simulation of a jetting bed

From a literature review, and comparison of the jet Froude number the experiment from Hensler et al. [116] was identified as suitable reference experiment.

The calculated jet angle and jet length differ by 10% and 22% compared to the experiment. The commonly applied empirical correlations from Merry [113] to predict jet angle and jet length are in poor agreement with the experiment (and the simulation). It is concluded that the correlations from Merry must be used carefully for jetting beds comparable to the experiments from Hensler et al..

The calculated height of the recirculation cell differs by only 1 cm with the experimentally determined height. The radial solids concentration profiles at different heights deviated between 6% and 30% compared to the experiment. The voidage in the surrounding bubbling bed is overestimated as already found for the simulation of the experiments from Holland et al. [126] (see above).

The applied numerical setup was proven to be capable to calculate jetting beds (in addition to bubbling beds and fast beds) at a reasonable accuracy.

CFD simulation of the COORVED gasifier

The validated simulation setup was employed to the COORVED lab-scale gasifier. The quality of the numerical grid, especially in the jet region, was proven by comparing the simulation against gas velocity measurements from Schimpke et al. [205]. Jet velocity profiles are in very good agreement with the experiment.

It was found that the patented boundary conditions will result in the desired zone formation. The bubbling-bed zone and the fast-bed zone have a voidage of 0.8 and 0.96, respectively. This compares very well with the findings from the Reh diagram. The simulation showed the formation of strands and a distinct core-annulus structure in the fast bed.

The jetting zone was shown to have a distinct lean core and a dense ($\varepsilon_{s,max}$>0.4) surrounding that can potentially protect the wall from flame radiation.

In general, the COORVED gasifier was successfully calculated by means of a TFM in conjunction with the KTGF. It was shown, that the expected zone will occur under the patented design.

ASPEN Plus® simulation

The 1D approach from ASPEN Plus® was successfully validated against the experiments from Holland et al. [126]. Differences in mean voidage compared to the experiment are between 7% and 11%.

After validation, the COORVED gasifier was calculated. The agreement with the CFD results is very good. The mean voidage in the bubbling bed-zone and fast-bed zone deviates by less than 10%. However, despite the very good agreement of the axial voidage profile in the bubbling bed and fast bed, the jet cannot be captured by ASPEN Plus®. Because ASPEN Plus® cannot reflect the development and vanish of the jet, a sudden jump in voidage is predicted due to the nature of a 1D approach.

Conclusion

Three computer-aided engineering tools to calculate different types of fluidized beds have been applied. Their advantages and disadvantages in terms of retrievable data, accuracy reliability, as well as simulation and modelling effort have been discussed.

After an extended validation, the COORVED gasifier was successfully calculated with all three approaches. All simulations predicted the development of the desired zones (bubbling bed, jetting bed, fast bed). Thus, the COORVED design is reasonable.

In the future, the three tools can be used to calculate reactive multi-phase flows in the COORVED lab-scale and industrial-scale unit. In addition, design changes can be evaluated on a high degree of reliability.

9 Outlook

9.1 Modeling Tools

From the literature review it can be expected, that enhanced drag models can improve the numerical results. It is suggested to test EMMS-type models [250] and filtered drag models [251,252] towards their applicability for bubbling beds, fast beds, and jetting beds.

Additional validation experiments for the jetting bed are required to investigate the recirculation cell under different operation conditions (jet velocity, velocity of base fluidization, gas properties, solids properties, reactor geometry). Moreover, a jet regime diagram could be developed employing nondimensional groups.

The simulations need to be extended by chemical reactions. This includes devolatilization, gas-solid reactions and gas-phase reactions. However, simulations of reactive fluidized beds found in literature [253–259], often spare out the validation of their model setup in terms of hydrodynamics. Thus, first priority is to capture the hydrodynamics accurately.

Polydispersity is another issue that need to be reflected in the simulations. It will affect the hydrodynamics as well as the chemical conversion Fine particles will heat up faster, devolatized earlier and be consumed faster compared to larger particles. This will affect the gas phase and temperature profile.

9.2 COORVED Development

During the course of the experimental campaigns EC1 (see Table 12), the set gas velocity was comparably high, for safety reasons as explained in Chapter 5.2. This resulted in comparably short residence times in the main reaction zone of the gasifier (jetting bed zone). In addition, it was found that the central hot flame was too close the walls (inner reactor diameter 0.15 m). This resulted in undesired deposition of ash and slag at the wall in this zone. Both issues can be solved by increasing the reactor diameter in the main reaction zone (compare Appendix 10.2). Thus, the following experimental campaigns EC2 and EC3 have been conducted in the new geometry with much more success. The approach of different diameters at different heights was patented in the following [260]. The new lab-scale unit needs to be calculated by means of CFD in the future to evaluate the hydrodynamics.

10 Appendix

10.1 Appendix 1 – Results Thermodynamic Calculations with ASPEN Plus

Brennstoff		Lausitzer Braunkohle	Süd-afrikanische Steinkohle	Pittsburgh No. 8	Herdofen-koks	Lausitzer Braunkohle	Süd-afrikanische Steinkohle	Pittsburgh No. 8	Herdofen-koks		Referenz-fall = 66 %
Anbieter		Vattenfall	Sasol	-	RWE	Vattenfall	Sasol	-	RWE	Maximum	%
Heizwert	MJ/kg	21.0	20.5	29.7	**29.9**	21.0	20.5	29.7	**29.9**	29.9	94.0
Anlagenleistung	kW	58.3	56.9	82.5	**83.1**	58.3	56.9	82.5	**83.1**	83.1	94.0
Aschegehalt	Ma.-% (wf*)	6.7	**25.33**	10.24	9.05	6.7	**25.33**	10.24	9.05	25.33	
Kohlemassenstrom	kg/h	10	10	10	10	10	10	10	10	10	
Skalierung	-	1	1	1	1	1	1	1	1		
Primär-O2	kg/h	4.71	4.75	6.00	6.99	4.79	4.88	6.08	**7.07**	7.07	99.2
	m³(i.N.)/h	3.29	3.33	4.20	4.89	3.35	3.42	4.26	**4.95**	4.95	
Temperatur	°C	200	200	200	200	200	200	200	200	200	
Primär-Dampf	kg/h	0.33	0.33	0.42	0.49	0.33	0.34	0.43	**0.49**	0.49	99.2
	g/min	5.49	5.54	7.00	8.15	5.58	5.69	7.09	**8.25**	8.25	
Temperatur	°C	200	200	200	200	200	200	200	200	200	
Düsendurchmesser (Mix)	mm	6.19	6.22	6.99	7.55	6.24	6.31	7.04	**7.59**	7.59	80.9
Austrittsgeschwindigkeit	m/s	60	60	60	60	60	60	60	60	60	
Sekundär-O2	kg/h	0.63	0.66	0.46	0.49	1.12	1.07	1.23	**1.24**	1.24	**129.4**
	m³(i.N.)/h	0.44	0.46	0.32	0.34	0.79	0.75	0.86	**0.87**	0.87	
Temperatur	°C	200	200	200	200	200	200	200	200	200	
Sekundär-Dampf	kg/h	5.76	**5.99**	4.16	4.44					5.99	68.6
	g/min	95.95	**99.75**	69.41	74.00					99.75	
Temperatur	°C	200	200	200.0	200					200	
Sekundär-CO2	kg/h					13.90	13.23	15.23	**15.31**	15.31	**NEU**
	m³(i.N.)/h					7.03	6.69	7.71	**7.74**	7.74	
Temperatur	°C					200	200	200	200	200	
Aschestrom	kg/h	0.25	2.09	0.64	0.57	0.25	**2.10**	0.60	0.54	2.10	**546.3**
Staubmenge (im Rohgas)	kg/h	0.70	0.65	0.74	0.67	0.70	0.63	**0.82**	0.74	0.82	76.9
Basisgas mit C-Umsatz	m³/h	15.89	15.90	15.89	15.90	15.89	15.90	15.90	15.89	15.90	
u	m/s	0.25	0.25	0.25	0.25	0.25	0.25	0.25	0.25	0.25	
Temperatur	°C	291	250	**506**	458	272	276	219	217	506	
Basisgas ohne C-Umsatz	m³/h	13.30	13.82	9.62	10.25	13.80	13.14	15.12	**15.19**	15.19	75.4
u	m/s	0.21	0.22	0.15	0.16	0.22	0.21	0.24	0.24	0.24	
Temperatur	°C	200	200	200	200	200	200	200	200	200	
Rohgas	m³/h	109.26	102.27	116.01	106.04	109.54	99.48	**127.97**	116.42	127.97	77.3
u	m/s	1.72	1.61	1.82	1.67	1.72	1.56	**2.01**	1.83	2.01	
Temperatur	°C	993	999	1000	1002	1000	1004	1000	999	1004	

		Lausitzer Braunkohle	Süd-afrikanische Steinkohle	Pittsburgh No. 8	Herdofen-koks	Lausitzer Braunkohle	Süd-afrikanische Steinkohle	Pittsburgh No. 8	Herdofen-koks	
		Vattenfall	Sasol	-	RWE	Vattenfall	Sasol	-	RWE	Max
Komponente										
H2	mol%	32.41	33.49	**39.98**	27.70	13.58	11.87	16.40	3.48	39.98
N2	mol%	0.24	0.54	0.40	0.21	0.24	**0.55**	0.36	0.19	0.55
CO	mol%	26.35	30.55	46.41	67.11	41.94	50.79	57.08	**77.68**	77.68
H2O	mol%	**24.62**	20.45	6.71	1.64	12.81	8.43	6.91	0.99	24.62
CO2	mol%	16.12	14.75	6.14	3.12	**31.19**	28.12	18.95	17.51	31.19
CH4	ppmv	28.92	39.37	301.98	**575.54**	5.64	6.40	24.78	2.30	575.54
H2S	ppmv	2306.60	2103.62	**3085.62**	1395.63	2102.36	1890.96	2540.77	696.12	3085.62
HCL	ppmv	48.64	27.53	0.00	0.00	**48.79**	28.42	0.00	0.00	48.79
COS	ppmv	86.24	88.11	164.43	155.16	298.00	371.21	406.00	**713.65**	713.65
NH3	ppmv	2.05	3.13	**3.50**	1.46	0.54	0.65	0.88	0.06	3.50
HCN	ppmv	0.02	0.04	0.21	**0.53**	0.02	0.04	0.06	0.04	0.53
Druck	bar	1	1	1	1	1	1	1	1	
Taupunkt	°C	64.6	60.5	38.2	14.4	50.7	42.5	38.8	6.9	64.6
Temperatur	°C	993	999	1000	1002	1000	1004	1000	999	
Massenstrom	kg/h	20.47	18.99	19.66	21.16	29.19	26.80	31.56	**32.83**	32.83
Molenstrom	kmol/h	1.04	0.97	1.10	1.00	1.03	0.94	**1.21**	1.10	1.21
Volumenstrom	m³/h	109.26	102.27	116.01	106.04	109.54	99.48	**127.97**	116.42	127.97
Normvolumenstrom	m³(i.N.)/h	23.25	21.66	24.54	22.41	23.18	20.98	**27.07**	24.65	27.07
Staubbeladung	g/m³(i.N.)	30.09	30.09	30.08	30.10	30.13	30.13	30.12	**30.14**	30.14
Brennstoffzusammensetzung										
Immediatanalyse	Ma.-%									
Wasser		**10.5**	5.61	2.4	0.5	**10.5**	5.61	2.4	0.5	10.50
Fixer Kohlenstoff	wf	42.46	51.38	53.69	**87.95**	42.46	51.38	53.69	**87.95**	87.95
Flüchtige	wf	**50.84**	23.29	36.07	3	**50.84**	23.29	36.07	3	50.84
Asche	wf	6.7	**25.33**	10.24	9.05	6.7	**25.33**	10.24	9.05	25.33

10.2 Appendix 2 – New Reactor Geometry

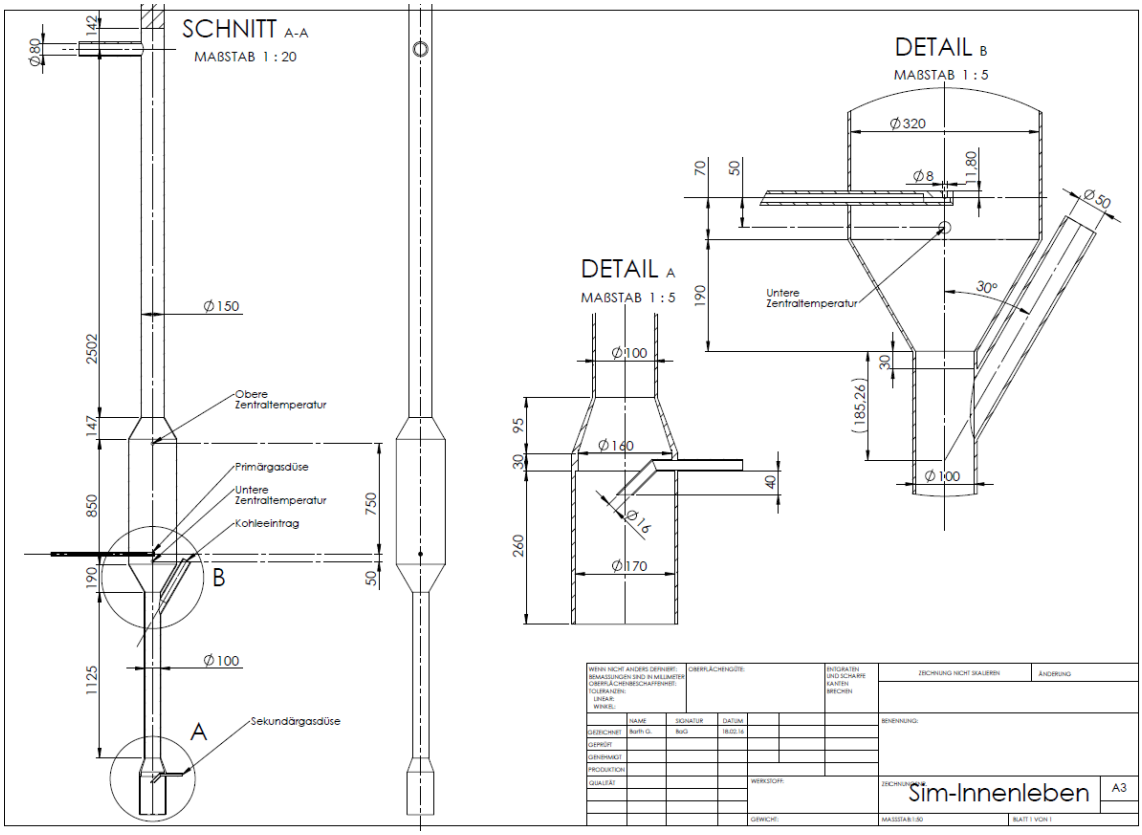

Figure 63 New reactor geometry

10.3 Appendix 3 – Additional CFD Results

10.3.1 Effect of Parallelization

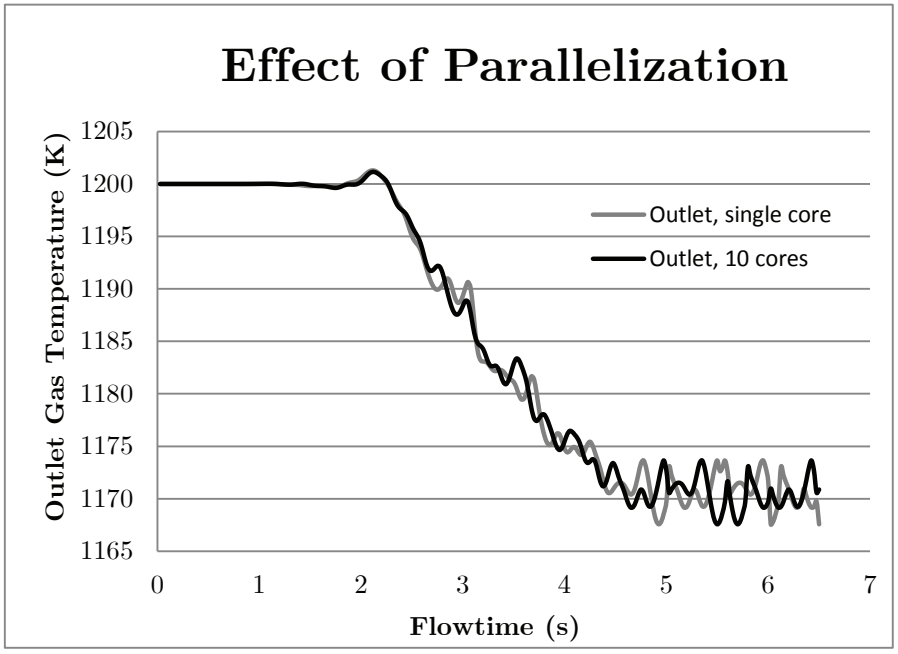

10.3.2 Sensitivity of voidage on grid resolution

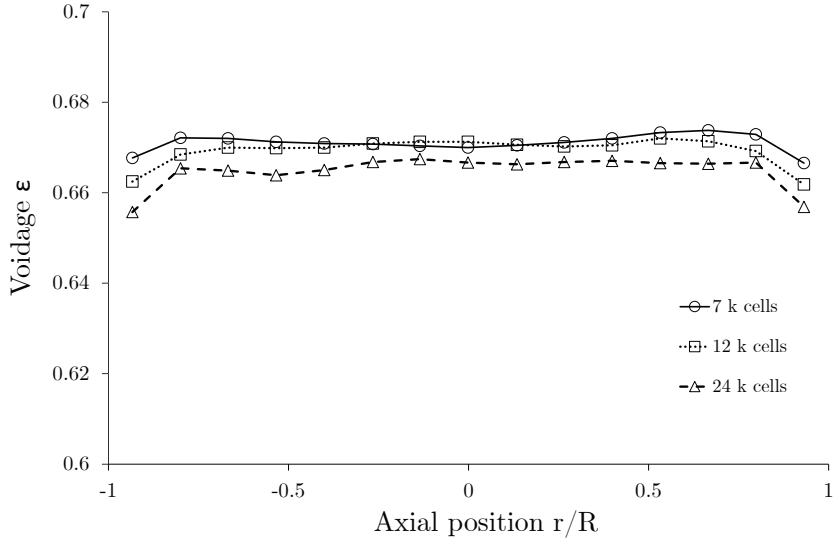

10.3.3 Effect of modified drag model on voidage

The modified drag model (G+) does not significantly increase the voidage, compared to the standard drag model (G).

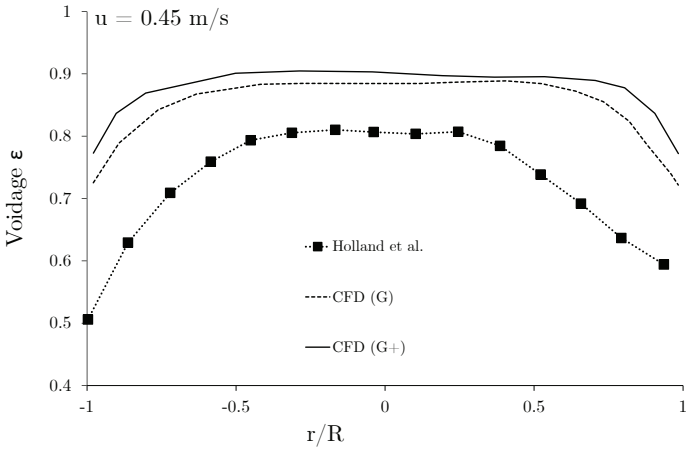

10.3.4 Comparison of solids velocity

The numerical results are compared to the experimental results from Holland et al. [126]. Evaluated is the vertical component of the solids velocity for the case u=0.45 m/s.

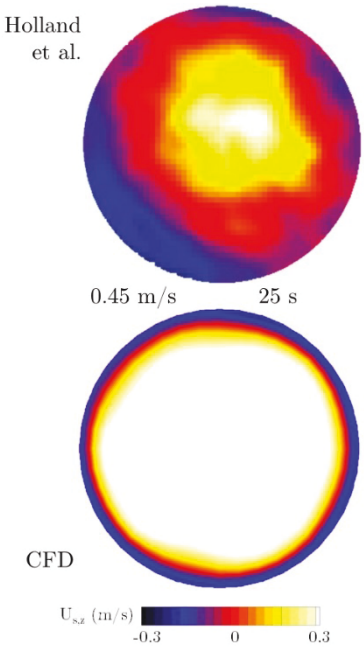

11 References

[1] Higman C. State of the Gasification Industry: Worldwide Gasification Database 2015 Update. Colorado Springs; 2015.

[2] Laugwitz A. Thermo-chemical and exergetic analysis of recent developments in coal gasification. Leipzig, Germany; 2011.

[3] Pardemann R, Meyer B. Stand und Perspektiven der Kohlenutzung in Kraftwerken mit Vergasung: Status and Perspectives of Coal Utilisation in Power Plants including Gasification. Chemie Ingenieur Technik 2011;83(11):1805–19.

[4] Tsuji H, Shirai H, Matsuda H, Rajoo P. Emission characteristics of NOx and unburned carbon in fly ash on high-ash coal combustion. Fuel 2011;90(2):850–3.

[5] Sadhukhan AK, Gupta P, Saha RK. Modelling of combustion characteristics of high ash coal char particles at high pressure: Shrinking reactive core model. Fuel 2010;89(1):162–9.

[6] Everson RC, Neomagus HW, Kaitano R, Falcon R, van Alphen C, du Cann, Vivien M. Properties of high ash char particles derived from inertinite-rich coal: 1. Chemical, structural and petrographic characteristics. Fuel 2008;87(15-16):3082–90.

[7] Sastry, Kal V. S. Pelletization of fine coals. Pittsburgh, PA; 1993.

[8] Haldar DD. Technologies for fine coal beneficiation in India. Dhanbad, India; 2010.

[9] Govender A, van Dyk J. Effect of wet screening on particle size distribution and coal properties. Fuel 2003;82(18):2231–7.

[10] Gräbner M. Industrial coal gasification technologies covering baseline and high-ash coal. Weinheim: Wiley-VCH; 2014.

[11] Xia L. China gasification market outlook. San Francisco, USA; 2011.

[12] Huang Z, Zhang J, Yue G. Status of domestic gasification technology in China. Front. Energy Power Eng. China 2009;3(3):330–6.

[13] Hartung J, Darby A. Pratt & Whitney Rocketdyne (PWR) - Compact gasification system

. Washington, D.C; 2006.

[14] Zhuang Q, Bowers K. Unlocking potential value from low rank coal with TRIG gasification technology. Beijing; 2013.

[15] Meyer B. Gasification technology development under changing constraints. Huhhot, Inner Mongolia; 2015.

[16] Nikrityuk PA, Meyer B (eds.). Gasification Processes: Modeling and Simulation. Hoboken: Wiley; 2014.

[17] Xu J. ECUST Coal Gasification Update: New Projects and Operations Experience. Washington, D.C; 2014.

[18] Nan Z, Ziman Yang. Energy project delivers historic first shipment. China Daily 2017, 16 January 2017; Available from: http://usa.chinadaily.com.cn/business/2016-12/29/content_27807069.htm. [January 16, 2017].

[19] Le Roux M, Campbell QP, Smit W. Large-scale design and testing of an improved fine coal dewatering system. The Journal of The Southern African Institute of Mining and 2012;112:673–6.

[20] White Energy. Coal fines opportunety. [March 09, 2016]; Available from: http://www.whiteenergyco.com/current-projects/south-africa/.

[21] Harrison CD, Akers DJ. Coals fines: Ressource of the future. [March 09, 2016]; Available from: http://www.netl.doe.gov/publications/proceedings/97/97cl/harrison.pdf.

[22] Meyer B, Seifert P, Krzack S, Ogriseck S, Rauchfuß H, Rieger M et al. Verfahren, Vergasungsreaktor und Anlage zur Flugstromvergasung fester Brennstoffe unter Druck(DE 10 2007 006 981 84 2009.01.29); 2007.

[23] Gräbner M, Meyer B. Performance and exergy analysis of the current developments in coal gasification technology. Fuel 2013.

[24] Reh L. Das Wirbeln von körnigem Gut im schlanken Diffusor als Grenzzustand zwischen Wirbelschicht und pneumatischem Transport. PhD Thesis. Karlsruhe; 1961.

[25] Miller BG. Coal energy systems. Amsterdam, Boston: Elsevier; 2005.

[26] Miller BG, Tillman DA. Combustion engineering issues for solid fuel systems. Amsterdam, Boston: Academic Press/Elsevier; 2008.

[27] Żelkowski J. Kohlecharakterisierung und Kohleverbrennung: Kohle als Brennstoff, Physik und Theorie der Kohleverbrennung, Technik. 2nd ed. Essen: VGB TowerTech; 2004.

[28] Berkowitz N. The chemistry of coal. Amsterdam, New York: Elsevier; 1985.

[29] Littlewood K. Gasification: Theory and application. Progress in Energy and Combustion Science 1977;3(1):35–71.

[30] Higman C, Burgt M. Gasification. Amsterdam: Gulf Professional; 2003.

[31] Smoot LD, Smith PJ. Coal combustion and gasification: Springer; 1985.

[32] Bell DA, Towler BF, Fan M (eds.). Coal gasification and its applications. 1st ed. Oxford, U.K, Burlington, MA: William Andrew/Elsevier; 2011.

[33] Breault RW. Gasification Processes Old and New: A Basic Review of the Major Technologies 2010;3(2):216–40.

[34] Schmalfeld J (ed.). Die Veredlung und Umwandlung von Kohle: Technologien und Projekte 1970 bis 2000 in Deutschland. Hamburg: DGMK; 2008.

[35] Yang W-C (ed.). Handbook of fluidization and fluid-particle systems. New York: Marcel Dekker; 2003.

[36] Gidaspow D. Multiphase Flow and Fluidization - Continuum and Kinetic Theory Descriptions. Amsterdam, Boston: Academic Press; 1994.

[37] Epstein N, Grace JR (eds.). Spouted and spout-fluid beds: Fundamentals and applications. Cambridge, New York: Cambridge University Press; 2011.

[38] Grace JR. Fluidized-bed hydrodynamics. In: Hetsroni G, editor. Handbook of multiphase systems: Hemisphere Pub. Corp; 1982, ch. 8-5 pp. 8-64.

[39] Grace JR, Avidan AA, Knowlton TM. Circulating fluidized beds. 1st ed. London, New York: Blackie Academic & Professional; 1997.

[40] Kunii D, Levenspiel O. Fluidization Engineering. Stoneham: Butterworth-Heinemann; 1991.

[41] Gupta CK, Sathiyamoorthy D. Fluid bed technology in materials processing. Boca Raton, Fla: CRC Press; 1999.

[42] Basu P. Combustion and gasification in fluidized beds. Boca Raton: CRC/Taylor & Francis; 2006.

[43] Fan L-S, Zhu C. Principles of gas-solid flows. 1st ed. Cambridge: Cambridge University Press; 2005.

[44] Krzack S. Grundlagen der Vergasung. In: Schmalfeld J, editor. Die Veredlung und Umwandlung von Kohle: Technologien und Projekte 1970 bis 2000 in Deutschland. Hamburg: DGMK; 2008.

[45] Gräbner M. Modeling-based evaluation of gasification processes for high-ash coals. Dissertation. Freiberg; 2012.

[46] Higman C, Tam S. Advances in coal gasification, hydrogenation, and gas treating for the production of chemicals and fuels. Chemical reviews 2014;114(3):1673–708.

[47] World energy outlook. Paris: OECD/IEA; 2014.

[48] Gräbner M, Meyer B. Coal gasification - Quo vadis? World of Mining - Surface and Underground 2010;62(6):355–62.

[49] Klara JM. Cost and Performance Baseline for Fossil Energy Plants: Volume 1: Bituminous Coal and Natural Gas to Electricity; 2007.

[50] Meyer B, Murza S. CO2 freie Kohlechemie für das Nach-Erdöl-Zeitalter. Dresden, Germany; 2011.

[51] Antonopoulos I-S, Karagiannidis A, Elefsiniotis L, Perkoulidis G, Gkouletsos A. Development of an innovative 3-stage steady-bed gasifier for municipal solid waste and biomass. Fuel Processing Technology 2011;92(12):2389–96.

[52] Yuehong Z, Hao W, Zhihong X. Conceptual design and simulation study of a co-gasification technology. Energy Conversion and Management 2006;47(11-12):1416–28.

[53] Kersten, Sascha R. A., Prins W, van der Drift, Bram, van Swaaij, Wim P. M. Principles of a novel multistage circulating fluidized bed reactor for biomass gasification. 17th International Symposium of Chemical Reaction Engineering (IS CRE 17) 2003;58(3–6):725–31.

[54] Wu J, Fang Y, Peng H, Wang Y. A new integrated approach of coal gasification: The concept and preliminary experimental results. Fuel Processing Technology 2004;86(3):261–6.

[55] Tsuji T, Uemaki O. Coal gasification in a jet-spouted bed. Can. J. Chem. Eng. 1994;72(3):504–10.

[56] Hirschfelder H. The BGL-Commercial Plants and Pilot Testing: Status and Perspectives on Envirotherm BGL-technology. Dresden, Germany; 2014.

[57] Turna O, Vierrath H, Meyer B, Guhl S, Reimert R. British Gas/Lurgi-Schlackebad-Vergaser (BGL). In: Schmalfeld J, editor. Die Veredlung und Umwandlung von Kohle: Technologien und Projekte 1970 bis 2000 in Deutschland. Hamburg: DGMK; 2008, p. 363–391.

[58] Lacey JA. The Gasification of Coal in a Slagging Pressure Gasifier. Solihull, England; 1966.

[59] Sander H-J, Daradimos G, Hirschfelder H. Operating Results of the BGL Gasifier at Schwarze Pumpe. San Francisco, USA; 2003.

[60] Olschar M, Schulze O. The BGL Commercial Plants and Pilot Testing. Leipzig, Germany; 2012.

[61] Tang X. Composition and Utilization of the Co-Products from Lurgi Gasifier. Beijing; 2013.

[62] Timmermann H. Mk Plus The Next Generation Lurgi FBDB Gasification. Leipzig, Germany; 2012.

[63] Adlhoch W. Hochtemperatur-Winkler-Verfahren (HTW). In: Schmalfeld J, editor. Die Veredlung und Umwandlung von Kohle: Technologien und Projekte 1970 bis 2000 in Deutschland. Hamburg: DGMK; 2008, p. 409–446.

[64] Adlhoch W, Keller J, Herbert PK. The development of the HTW coal gasification process; 1990.

[65] Schaaf T, Hermann L, Johansson R, Pardemann R. Integrate Concept for Biomass Utilization to Produce Fuel Gas and Fertilizer. Malmö, Sweden; 2016.

[66] Horvath A, Salo K, Patel J. Synthesis Gas Production from Biomass. San Francisco, USA; 2011.

[67] Goyal A, Rehmat A, Knowlton TM, Leppin D, Waibel RT, Patel JG. Support studies for the U-GAS coal gasification process: Part I: Fluidization. Fuel Processing Technology 1987;17(2):169–86.

[68] Goyal A, Rehmat A, Knowlton T, Leppin D, Waibel R, Patel J. Support studies for the U-GAS coal gasification process. Part II: Combustion characteristics. Fuel Processing Technology 1988;17(3):209–19.

[69] Sheng R. Recent Developments and Deployment of SES Gasification Technology. Beijing, China; 2013.

[70] Salvador LA, Holmgren JD, Rath LK, Margaritis PJ. Development of the Westinghouse coal gasification process - A status report. Washington, D.C.: Westinghouse Electric Corp; 1977.

[71] Arnold, M. S. T. J., Gale JJ, Laughlin MK. The British Coal Spouted Fluidised Bed Gasification Process. Can. J. Chem. Eng. 1992;70(5):991–7.

[72] Radtke K. Tailor-made Gasification Solutions: ThyssenKrupp Uhde's HTW™ and PRENFLO® Technologies. Colorado Springs; 2013.

[73] Hannemann F. Economical and Environmental Targets for Gasification. Dresden, Germany; 2014.

[74] Hannemann F. Gasification: status, outlook and technical developments. In: ; 2010.

[75] Chen W-H, Peng J, Bi XT. A state-of-the-art review of biomass torrefaction, densification and applications. Renewable and Sustainable Energy Reviews 2015;44:847–66.

[76] Beckmann M, Hurtado A. Kraftwerkstechnik: Sichere und nachhaltige Energieversorgung - Band 2 ; [Beiträge des 42. Kraftwerkstechnischen Kolloquiums 12. und 13. Oktober 2010 in Dresden]. Neuruppin: TK-Verl., Thomé-Kozmiensky; 2010.

[77] Woolcock PJ, Brown RC. A review of cleaning technologies for biomass-derived syngas. Biomass and Bioenergy 2013;52:54–84.

[78] Liu Z, Fang Y, Deng S, Huang J, Zhao J, Cheng Z. Simulation of pressurized ash agglomerating fluidized bed gasifier using aspen plus. Energy and Fuels 2012;26(2):1237–45.

[79] Gómez-Barea A, Leckner B, Villanueva Perales A, Nilsson S, Fuentes Cano D. Improving the performance of fluidized bed biomass/waste gasifiers for distributed electricity: A new three-stage gasification system. Applied Thermal Engineering 2013;50(2):1453–62.

[80] Gräbner M, Meyer B. Introduction of a ternary diagram for comprehensive evaluation of gasification processes for ash-rich coal. Advances in Coal Science and Technology, ICCS&T 2011 2013;114:56–63.

[81] Xie H-Y. The role of interparticle forces in the fluidization of fine particles. Powder Technology 1997;94(2):99–108.

[82] Geldart D. Types of Gas Fluidizaiton. Powder Technology 1973(7):285–92.

[83] Molerus O. Interpretation of Geldart's type A, B, C and D powders by taking into account interparticle cohesion forces. Powder Technology 1982;33(1):81–7.

[84] Grace JR. Contacting modes and behaviour classification of gas-solid and other two-phase suspensions. Can. J. Chem. Eng. 1986;64(3):353–63.

[85] Goossens WR. Classification of fluidized particles by Archimedes number. Powder Technology 1998;98(1):48–53.

[86] D18 Committee. Test Method for Measuring the Minimum Fluidization Velocities of Free Flowing Powders. West Conshohocken, PA: ASTM International; 2012. doi:10.1520/D7743-12.

[87] Issangya A, Hays R, Cocco RA, Knowlton TM, Karri S. An Acoustic Method for the Measurement of Minimum Fluidization and Bubbling Properties of Group A Solids. San Francisco, USA; 2013.

[88] Abbasi M, Sotudeh-Gharebagh R, Mostoufi N, Zarghami R, Mahjoob MJ. Nonintrusive characterization of fluidized bed hydrodynamics using vibration signature analysis. AIChE J. 2009:NA-NA.

[89] Yang W-C. Bubbling Fluidized Beds. In: Yang W-C, editor. Handbook of fluidization and fluid-particle systems. New York: Marcel Dekker; 2003, p. 53–111.

[90] Farshi A. Experimental Measurement of Differten Fluidization Parameters. Petroleum and Coal 2013;55(4):311–21.

[91] Ergun S, Orning, A. A. Fluid Flow through Randomly Packed Columns and Fluidized Beds. Ind. Eng. Chem. 1949;41(6):1179–84.

[92] Wen CY, Yu, Y. H. A generalized method for predicting the minimum fluidization velocity. AIChE J. 1966;12(3):610–2.

[93] Babu SP, Shah B, Talwalkar A. Fluidization correlations for coal gasificaiton materials - Minimum fluidization velocity amd fluidized bed expansion ratio. AIChE Symp Ser 1978;74(176):176–86.

[94] Chitester DC, Kornosky RM, Fan L-S, Danko JP. Characteristics of fluidization at high pressure. Chemical Engineering Science 1984;39(2):253–61.

[95] Yerushalmi J, Cankurt NT. Further studies of the regimes of fluidization. Powder Technology 1979;24(2):187–205.

[96] Horio M, Ishii H, Nishimuro M. On the nature of turbulent and fast fluidized beds. Powder Technology 1992;70(3):229–36.

[97] Yerushalmi J, Turner DH, Squires AM. The Fast Fluidized Bed. Ind. Eng. Chem. Proc. Des. Dev. 1976;15(1):47–53.

[98] Reh L. Fluidized bed processing. Chemical Engineering Progress 1971;67(2):58–63.

[99] Bi HT, Ellis N, Abba IA, Grace JR. A state-of-the-art review of gas–solid turbulent fluidization. Chemical Engineering Science 2000;55(21):4789–825.

[100] Grace JR, Bi HT, Gorliz M. Circulating Fluidized Beds. In: Yang W-C, editor. Handbook of fluidization and fluid-particle systems. New York: Marcel Dekker; 2003, p. 485–544.

[101] Chen JC. Heat Transfer. In: Yang W-C, editor. Handbook of fluidization and fluid-particle systems. New York: Marcel Dekker; 2003, p. 257–286.

[102] H.T. Bi, J.R. Grace. Effect of measurement method on the velocities used to demarcate the onset of turbulent fluidization. The Chemical Engineering Journal and the Biochemical Engineering Journal 1995;57(3):261–71.

[103]Leu L, Huang J, Gua B-B. Axial pressure distribution in turbulent fluidized beds. In: Leu L, Lu W, editors. Proceedings of the Second Asian Conference on Fluidized-bed & Three-phase Reactors; 1990, p. 71–79.

[104]Bi H, Fan L-S. Existence of turbulent regime in gas-solid fluidization. AIChE J. 1992;38(2):297–301.

[105]Adánez J, Diego LF de, Gayán P. Transport velocities of coal and sand particles. Powder Technology 1993;77(1):61–8.

[106]Tsukada M, Nakanishi D, Horio M. The effect of pressure on the phase transition from bubbling to turbulent fluidization. International Journal of Multiphase Flow 1993;19(1):27–34.

[107]Karri S, Werther J. Gas Distributor and Plenum Design in Fluidized Beds. In: Yang W-C, editor. Handbook of fluidization and fluid-particle systems. New York: Marcel Dekker; 2003, p. 155–170.

[108]Yang S, Li H, Zhu Q. Experimental study and numerical simulation of baffled bubbling fluidized beds with Geldart A particles in three dimensions. Chemical Engineering Journal 2015;259:338–47.

[109]Yang W-C. Other Nonconventional Fluidized Beds. In: Yang W-C, editor. Handbook of fluidization and fluid-particle systems. New York: Marcel Dekker; 2003, p. 545–570.

[110]Yang W-C. Fluidization, solids handling, and processing: Industrial applications. Westwood, N.J.: Noyes Publications; 1998.

[111]Yang W-C. Jet penetration in a pressurized fluidized bed. Ind. Eng. Chem. Fund. 1981;20(3):297–300.

[112]Yang W-C. 30 years of industrial research on fluidization: Bridging the gap btween theory and practice. In: Fan L-S, Knowlton TM, editors. Fluidization IX: Proceedings of the Ninth Engineering Foundation Conference on Fluidization Durango, Colorado, May 17-22, 1998. New York, NY: Engineering Foundation; 1998, p. 31–43.

[113]Merry, J. M. D. Penetration of vertical jets into fluidized beds. AIChE J. 1975;21(3):507–10.

[114]WU C-S, WHITING WB. Interacting jets in fluidized beds. Chemical Engineering Communications 1988;73(1):1–17.

[115]Yang W-C, Keairns DL. Momentum Dissipation of and Gas Entrainment into a Gas-Solid Two-Phase Jet in a Fluidized Bed. In: Grace JR, Matsen JM, editors. Fluidization. Boston, MA: Springer US; 1980, p. 305–314.

[116]Hensler T, Tupy M, Strer T, Pöschel T, Wirth K-E. Positron emission particle tracking in fluidized beds with secondary gas injection. Powder Technology 2015;279:113–22.

[117]Yang W-C, Keairns DL. Solid entrainment rate into gas and gas—solid, two-phase jets in a fluidized bed. Powder Technology 1982;33(1):89–94.

[118]Mathur KB, Epstein N. Spouted beds. New York: Academic Press; 1974.

[119]He Y-L. Hydrodynamic and scale-up studies of spouted beds. Ottawa: National Library of Canada = Bibliothèque nationale du Canada; 1995.

[120]Shao Y, Liu X, Zhong W, Jin B-S, ZHANG M. Recent advances of spout-fluid bed: A Review of Fundamentals and Applications. International Journal of Chemical Reactor Engineering 2013;11(1).

[121]Sahoo A, Ramesh C, Biswal, K. C. Experimental and computational study of the bed dynamics of semi-cylindrical gas–solid fluidized bed. Can. J. Chem. Eng. 2009;87(1):11–8.

[122]Altzibar H, Lopez G, Bilbao J, Olazar M. Minimum Spouting Velocity of Conical Spouted Beds Equipped with Draft Tubes of Different Configuration. Ind. Eng. Chem. Res. 2013;52(8):2995–3006.

[123]Mathur KB, Gishler PE. A technique for contacting gases with coarse solid particles. AIChE J. 1955;1(2):157–64.

[124]King DF, Harrison D. The minimum spouting velocity of a spouted bed at elevated pressure. Powder Technology 1980;26(1):103–7.

[125]Cheremisinoff NP. Review of experimental methods for studying the hydrodynamics of gas-solid fluidized beds. Industrial & Engineering Chemistry Process Design and Development 1986;25(2):329–51.

[126]Holland, D. J., Müller CR, Dennis JS, Gladden LF, Davidson JF. Magnetic Resonance Studies of Fluidization Regimes. Ind. Eng. Chem. Res. 2010;49(12):5891–9.

[127]Samuelsberg A, Hjertager BH. An experimental and numerical study of flow patterns in a circulating fluidized bed reactor. International Journal of Multiphase Flow 1996;22(3):575–91.

[128]Sasic S, Leckner B, Johnsson F. Characterization of fluid dynamics of fluidized beds by analysis of pressure fluctuations. Progress in Energy and Combustion Science 2007;33(5):453–96.

[129]Xu G, Gao S. Necessary parameters for specifying the hydrodynamics of circulating fluidized bed risers—a review and reiteration. Powder Technology in China 2003;137(1–2):63–76.

[130]Zhu J-X, Li G-Z, Qin S-Z, Li F-Y, Zhang H, Yang Y-L. Direct measurements of particle velocities in gas–solids suspension flow using a novel five-fiber optical probe. Powder Technology 2001;115(2):184–92.

[131]Rüdisüli M, Schildhauer TJ, Biollaz, Serge M. A., van Ommen, J. Ruud. Scale-up of bubbling fluidized bed reactors — A review. Powder Technology 2012;217:21–38.

[132]Leckner B, Szentannai P, Winter F. Scale-up of fluidized-bed combustion – A review. Fuel 2011;90(10):2951–64.

[133]Al-Rashed M, Wójcik J, Plewik R, Synowiec P, Kuś A. Multiphase CFD modeling: Fluid dynamics aspects in scale-up of a fluidized-bed crystallizer. Chemical Engineering and Processing: Process Intensification 2013;63:7–15.

[134]Knowlton TM, Karri S, Issangya A. Scale-up of fluidized-bed hydrodynamics. Powder Technology 2005;150(2):72–7.

[135]Wilhelm RH, Kwauk M. Fluidization of solid particles; 1948.

[136]Doichev K, Todorov S, Dimitrov V. Transition between particulate and aggregative fluidization at different state-of-flow of the solids. Chemical Engineering Science 1975;30(4):419–24.

[137]Zenz FA. Two-Phase Fluid-Solid Flow. Ind. Eng. Chem. 1949;41(12):2801–6.

[138]Bi HT, Grace JR. Flow regime diagrams for gas-solid fluidization and upward transport. International Journal of Multiphase Flow 1995;21(6):1229–36.

[139]Michel W. Wirbelschichttechnik in der Energiewirtschaft: Mit 16 Tabellen. 1st ed. Leipzig: Dt. Verl. für Grundstoffindustrie; 1992.

[140]Zhong W, ZHANG M, JIN B, Chen X. Flow pattern and transition of rectangular spout–fluid bed. Chemical Engineering and Processing: Process Intensification 2006;45(9):734–46.

[141]Marmo L. Low temperature drying of pomace in spout and spout-fluid beds. Journal of Food Engineering 2007;79(4):1179–90.

[142]Sutkar VS, Deen NG, Kuipers, J. A. M. Spout fluidized beds: Recent advances in experimental and numerical studies. 5th International Granulation Workshop 2013;86:124–36.

[143]Guo Q, Yue G, Liu Z. Gas discharge patterns in a large jetting fluidized bed with a vertical nozzle. Industrial and Engineering Chemistry Research 2001;40(16):3689–96.

[144]Link JM, Cuypers LA, Deen NG, Kuipers J. Flow regimes in a spout–fluid bed: A combined experimental and simulation study. Chemical Engineering Science 2005;60(13):3425–42.

[145]Dymen J, Reimers C, Beck R. Overview of solids modeling for chemical processes: An industry white paper; 2013.

[146]Yan L, Jim Lim C, Yue G, He B, Grace JR. One-dimensional modeling of a dual fluidized bed for biomass steam gasification. Energy Conversion and Management 2016;127:612–22.

[147]Nikoo MB, Mahinpey N. Simulation of biomass gasification in fluidized bed reactor using ASPEN PLUS. Biomass and Bioenergy 2008;32(12):1245–54.

[148]Pauls JH, Mahinpey N, Mostafavi E. Simulation of air-steam gasification of woody biomass in a bubbling fluidized bed using Aspen Plus: A comprehensive model including pyrolysis, hydrodynamics and tar production. Biomass and Bioenergy 2016;95:157–66.

[149]Mirmoshtaghi G, Li H, Thorin E, Dahlquist E. Evaluation of different biomass gasification modeling approaches for fluidized bed gasifiers. Biomass and Bioenergy 2016;91:69–82.

[150]aspentech. Aspen Plus: user guide; 2016.

[151]Anderson TB, Jackson R. A fluid mechanical description of fluidized beds: Equations of motion. Industrial and Engineering Chemistry Fundamentals 1967;6(4):527–39.

[152]Ishii M. Thermo-fluid dynamic theory of two-phase flow. [Paris]: Eyrolles; 1975.

[153]van der Hoef, M. A., van Sint Annaland M, Deen NG, Kuipers, J. A. M. Numerical Simulation of Dense Gas-Solid Fluidized Beds: A Multiscale Modeling Strategy. Annu. Rev. Fluid Mech. 2008;40(1):47–70.

[154]Enwald H, Peirano E, Almstedt A-E. Eulerian two-phase flow theory applied to fluidization. Internation Journal of Multiphase Flow 1996;22:21–66.

[155]Tsuji Y, Kawaguchi T, Tanaka T. Discrete particle simulation of two-dimensional fluidized bed. Powder Technology 1993;77(1):79–87.

[156]Schreiber M. Modellierung von Hydrodynamik und Wärmeübertragung in blasenbildenden Wirbelschichten zur Trocknung von Braunkohle. Dissertation. Cottbus; 2013.

[157]Syamlal M, Pannala S. Multiphase continuum formulation for gas-solids reacting flows. In: Pannala S, Syamlal M, O'Brien TJ, editors. Computational gas-solids flows and reacting systems: Theory, methods and practice. Hershey, PA: Engineering Science Reference; 2011, p. 1–65.

[158]Gidaspow D, Jung J, Singh RK. Hydrodynamics of fluidization using kinetic theory: an emerging paradigm. Powder Technology 2004;148(2-3):123–41.

[159]Sinclair JL, Jackson R. Gas-particle flow in a vertical pipe with particle-particle interactions. AIChE J. 1989;35(9):1473–86.

[160]Klimanek A, Adamczyk W, Katelbach-Woźniak A, Węcel G, Szlęk A. Towards a hybrid Eulerian–Lagrangian CFD modeling of coal gasification in a circulating fluidized bed reactor. International Freiberg Conference on IGCC & XtL Technologies in 2014 2015;152:131–7.

[161]Deen NG, van Sint Annaland M, van der Hoef, M. A., Kuipers J. Review of discrete particle modeling of fluidized beds. Fluidized Bed Applications 2007;62(1–2):28–44.

[162]Dufty JW, Baskaran A. Hydrodynamic equations from kinetic theory: Fundamental considerations. In: Pannala S, Syamlal M, O'Brien TJ, editors. Computational gas-solids flows and reacting systems: Theory, methods and practice. Hershey, PA: Engineering Science Reference; 2011, p. 66–101.

[163]Ishii M, Mishima K. Study of two-fluid model and interfacial area. Washington, D.C, Springfield, Va: The Commission; Available from GPO Sales Program, Division of Technical Information and Document Control, U.S. Nuclear Regulatory Commission; National Technical Information Service; 1980.

[164]Balzer G, Boelle A, Simonon O. Eulerian gas–solid flow modeling of dense fluidised bed. In: Large JF, Laguérie C, Foundation E, editors. Fluidization VIII: Proceedings of the Eighth Engineering Foundation Conference on Fluidization, May 14-19, 1995, Tours, France: Engineering Foundation; 1996, p. 409–418.

[165]van der Hoef, M. A., Ye M, van Sint Annaland M, Andrews AT, Sundaresan S, Kuipers, J. A. M. Multiscale Modeling of Gas-Fluidized Beds. In: Guy B. Marin, editor. Advances in Chemical Engineering Computational Fluid Dynamics: Academic Press; 2006, p. 65–149.

[166]Fan L-S, Zhu C. Principles of gas-solid flows. 1st ed. Cambridge: Cambridge University Press; 2005.

[167]Yates JG. Effect of temperature and presure. In: Yang W-C, editor. Handbook of fluidization and fluid-particle systems. New York: Marcel Dekker; 2003, p. 129–154.

[168]Lundberg J, Halvorsen BM. A review of some existing drag models descibing the interaction between phases in bubbling fluidize beds. Telmark, Norway; 2008.

[169]Prabhansu, Dey S, Karmakarm Malay K., Chandra P, Chatterjee PK. Studies on various drag models in fluidized bed for abatement of environmental pollution. Internation Journal of Environmental Science 2015;5(5).

[170]Huilin L, Gidaspow D. Hydrodynamics of binary fluidization in a riser: CFD simulation using two granular temperatures. Chemical Engineering Science 2003;58(16):3777–92.

[171]Syamlal M, O'Brien TJ (eds.). Computer simulation of bubbles in a fluidized bed; 1989.

[172]DallaValle JM. Micromeritics: The technology of fine particles. 2nd edition. New York: Pitman Pub. Corp; 1948.

[173]Richardson JF, Zaki WN. Sedimentation and fluidisation: Part I. Chemical Engineering Research and Design 1997;75:S82-S100.

[174]Garside J, Al-Dibouni MR. Velocity-voidage relationships for fluidization and sedimentation in solid-liquid systems. Ind. Eng. Chem. Proc. Des. Dev. 1977;16(2):206–14.

[175]Li J, Kwauk M. Particle-fluid two-phase flow: The energy-minimization multi-scale method. Beijing: Metallurgical Industry Press; 1994.

[176]Ghadirian E, Arastoopour H. CFD simulation of a fluidized bed using the EMMS approach for the gas-solid drag force. Powder Technology 2016;288:35–44.

[177]Benzarti, S. Mhiri, H. Bournot, H. Drag models for simulation gas-olid flow in the bubbling fluidized bed of FCC particles. International Journal of Chemical, Molecular, Nuclear, Materials and Metallurgical Engineering 2012(1):111–6.

[178]Benzarti S, Mhiri H, Bournot H, Occelli R. Numerical simulation of turbulent fluidized bed with Geldart B particles. Advanced Powder Technology 2014;25(6):1737–47.

[179]Du W, Bao X, Xu J, Wei W. Computational fluid dynamics (CFD) modeling of spouted bed: Influence of frictional stress, maximum packing limit and coefficient of restitution of particles. Chemical Engineering Science 2006;61(14):4558–70.

[180]Loha C, Chattopadhyay H, Chatterjee PK. Assessment of drag models in simulating bubbling fluidized bed hydrodynamics. Chemical Engineering Science 2012;75:400–7.

[181]Min J, Drake JB, Heindel TJ, Fox RO. Experimental validation of CFD simulations of a lab-scale fluidized-bed reactor with and without side-gas injection. AIChE J. 2010;56(6):1434–46.

[182]Li P, Lan X, Xu C, Wang G, Lu C, Gao J. Drag models for simulating gas–solid flow in the turbulent fluidization of FCC particles. Particuology 2009;7(4):269–77.

[183]Hernández-Jiménez F, Sánchez-Delgado S, Gómez-García A, Acosta-Iborra A. Comparison between two-fluid model simulations and particle image analysis & velocimetry (PIV) results for a two-dimensional gas–solid fluidized bed. Chemical Engineering Science 2011;66(17):3753–72.

[184]Lungu M, Zhou Y, Wang J, Yang Y. A CFD study of a bi-disperse gas–solid fluidized bed: Effect of the EMMS sub grid drag correction. Powder Technology 2015;280:154–72.

[185]Jenkins JT, Savage SB. A theory for the rapid flow of identical, smooth, nearly elastic, spherical particles. Journal of fluid mechanics 1983;130:187–202.

[186]Lun CK, Savage SB, Jeffrey DJ, Chepurniy N. Kinetic theories for granular flow: inelastic particles in Couette flow and slightly inelastic particles in a general flowfield. Journal of fluid mechanics 1984;140:223–56.

[187]Huilin L, Yurong H, Wentie L, Ding J, Gidspow D, Bouillard J. Computer simulations of gas–solid flow in spouted beds using kinetic–frictional stress model of granular flow. Chemical Engineering Science 2004;59:865–78.

[188]Patil DJ, van Sint Annaland M, Kuipers J. Critical comparison of hydrodynamic models for gas–solid fluidized beds—Part I: Bubbling gas–solid fluidized beds operated with a jet. Chemical Engineering Science 2005;60(1):57–72.

[189]Lindborg H, Lysberg M, Jakobsen HA. Practical validation of the two-fluid model applied to dense gas–solid flows in fluidized beds. Chemical Engineering Science 2007;62(21):5854–69.

[190]Gidaspow D, Bezburuah R, Ding J. Hydrodynamics of circulating fluidized beds: Kinetic theory approach. Washington, D.C., Oak Ridge, Tenn.: United States. Dept. of Energy; distributed by the Office of Scientific and Technical Information, U.S. Dept. of Energy; 1991.

[191]Schaeffer DG. Instability in the evolution equations describing incompressible granular flow. Journal of Differential Equations 1987;66(1):19–50.

[192]Reuge N, Cadoret L, Coufort-Saudejaud C, Pannala S, Syamlal M, Caussat B. Multifluid Eulerian modeling of dense gas-solids fluidized bed hydrodynamics: influence of the dissipation parameters. Chemical Engineering Science 2008;63(22):5540–51.

[193]Arastoopour H, Gidaspow D, Abbasi E. Computational transport phenomena of fluid-particle systems. Cham, Switzerland: Springer; 2017.

[194]Johnson PC, Jackson R. Frictional–collisional constitutive relations for granular materials, with application to plane shearing. J. Fluid Mech. 1987;176(-1):67.

[195]Goldschmidt M, Kuipers J, Swaaij W. Hydrodynamic modeling of dense gas-fluidised beds using the kinetic theory of granular flow: effect of coefficient of restitution on bed dynamics. Chemical Engineering Science 2001;56:571–8.

[196]Laugwitz A, Gräbner M, Meyer B. Modeling based development of internally circulating gasifier for high ash coals. In: University of Pittsburgh, editor. Proceedings of the Pittsburgh Coal Conference. Beijing, China; 2013.

[197]Reza MO, Laugwitz A, Nikrityuk P. Cylindrical-conical spouted bed dynamics: Laminar and turbulent flow predictions; 2016.

[198]Loha C, Chattopadhyay H, Chatterjee PK. Effect of coefficient of restitution in Euler-Euler CFD simulation of fluidized-bed hydrodynamics. Particuology 2014;15:170–7.

[199]Sebastian Zimmermann, Fariborz Taghipour. CFD Modeling of the Hydrodynamics and Reaction Kinetics of FCC Fluidized-Bed Reactors. Industrial & Engineering Chemistry Research 2005;44(26):9818–27.

[200]Geng S, Jia Z, Zhan J, Liu X, Xu G. CFD modeling the hydrodynamics of binary particle mixture in pseudo-2D bubbling fluidized bed: Effect of model parameters. Powder Technology 2016;302:384–95.

[201]Lun CKK, Savage SB. The effects of an impact velocity dependent coefficient of restitution on stresses developed by sheared granular materials. Acta Mechanica 1986;63(1):15–44.

[202]Laugwitz A, Schurz M, Meyer B. Modeling and experimental investigation of an internally circulating gasifier for high ash coals. In: University of Pittsburgh, editor. Proceedings of the Pittsburgh Coal Conference. Pittsburgh, PA, USA; 2014.

[203]Laugwitz A, Meyer B. New frontiers and challenges in gasification technologies. In: Nikrityuk PA, Meyer B, editors. Gasification Processes: Modeling and Simulation. Hoboken: Wiley; 2014.

[204]Ogriseck S. Verfahrenstechnische Auslegung grosstechnischer Wirbelschichtvergaser der 1000 MW(th)-Klasse. Düsseldorf: VDI-Verl; 2007.

[205]Schimpke R, Laugwitz A, Schurz M, Krzack S, Meyer B. Flow pattern evaluation of the internal circulation gasifying principle. Fuel 2015;147:221–9.

[206]Schurz M, Laugwitz A, Krzack S, Meyer B. Start-up of internal circulation gasifier COORVED. Dresden, Germany; 2014.

[207]Schurz M, Laugwitz A, Krzack S, Meyer B. Ash agglomeration in the modified COORVED gasifier. Cologne, Germany; 2016.

[208]Stelzner B, Hunger F, Laugwitz A, Gräbner M, Voss S, Uebel K et al. Development of an inverse diffusion partial oxidation flame and model burner contributing to the development of 3rd generation coal gasifiers. Fuel Processing Technology 2013;110:33–45.

[209]Nilsson S, Gómez-Barea A, Fuentes-Cano D, Ollero P. Gasification of biomass and waste in a staged fluidized bed gasifier: Modeling and comparison with one-stage units. Fuel 2012;97:730–40.

[210]van Rossum G, Kersten, Sascha R. A., van Swaaij, Wim P. M. Staged Catalytic Gasification/Steam Reforming of Pyrolysis Oil. Ind. Eng. Chem. Res. 2009;48(12):5857–66.

[211]Hsieh CR, Roberts PT. Chevron Research Company - A laboratory study of agglomeration in coal gasification; 1985.

[212]Mason DM, Rehmat A, Tsao K. Chemistry of ash deposits in the U-GAS process. Chicago, Ill: Institute of gas technology; 1982.

[213]Bartels M, Lin W, Nijenhuis J, Kapteijn F, van Ommen, J. Ruud. Agglomeration in fluidized beds at high temperatures: Mechanisms, detection and prevention. Progress in Energy and Combustion Science 2008;34(5):633–66.

[214]Khadilkar AB, Rozelle PL, Pisupati SV. A study on initiation of ash agglomeration in fluidized bed gasification systems. Fuel 2015;152:48–57.

[215]Khadilkar AB, Rozelle PL, Pisupati SV. Review of Particle Physics and Chemistry in Fluidized Beds for Development of Comprehensive Ash Agglomeration Prediction Models. Energy Fuels 2016;30(5):3714–34.

[216]Chen D, Tang L, Zhou Y, Wang W, Wu Y, Zhu Z. Effect of char on the melting characteristics of coal ash. Journal of fuel chemistry and technology 2007;35(2):136–40.

[217]Schurz M. Experimental investigation in the lab-scale INCI gasifier (prelim. title). Dissertation (under review). Freiberg; 2017.

[218]Grace JR, Taghipour F. Verification and validation of CFD models and dynamic similarity for fluidized beds. Powder Technology 2004;139(2):99–110.

[219]Syamlal M, Rogers WA, O'Brien TJ. MFIX Documentation: Volume 1: Theory Guide. Springfield, Va; 1993.

[220]Patankar SV, Spalding DB. A calculation procedure for heat, mass and momentum transfer in three-dimensional parabolic flows. International Journal of Heat and Mass Transfer 1972;15(10):1787–806.

[221]Brauer H. Grundlagen der Einphasen- und Mehrphasenströmungen: 2nd ed.: Sauerländer; 1971.

[222]Guenther C, Syamlal M. The effect of numerical diffusion on simulation of isolated bubbles in a gas-solid fluidized bed. Powder Technology 2001;116(2-3):142–54.

[223]Xie N, Battaglia F, Pannala S. Effects of using two- versus three-dimensional computational modeling of fluidized beds. Part I, hydrodynamics. Powder Technology 2008;182(1):1–13.

[224]Li T, Grace J, Bi X. Study of wall boundary condition in numerical simulations of bubbling fluidized beds. Powder Technology 2010;203(3):447–57.

[225]Wang Y, Chao Z, Jakobsen HA. A sensitivity study of the two-fluid model losure parameters (β, e) determining the main gas-solid flow pattern characteristics. Industrial and Engineering Chemistry Research 2010;49(7):3433–41.

[226]Chalermsinsuwan B, Gidaspow D, Piumsomboon P. Two- and three-dimensional CFD modeling of Geldart A particles in a thin bubbling fluidized bed: Comparison of turbulence and dispersion coefficients. Chemical Engineering Journal 2011;171(1):301–13.

[227]Sande PC, Ray S. Mesh size effect on CFD simulation of gas-fluidized Geldart A particles. Powder Technology 2014;264:43–53.

[228]A. Samuelsberg, B.H. Hjertager. An experimental and numerical study of flow patterns in a circulating fluidized bed reactor. International Journal of Multiphase Flow 1996;22(3):575–91.

[229]Van den Moortel, T, Azario E, Santini R, Tadrist L. Experimental analysis of the gas-particle flow in a circulating fluidized bed using a phase Doppler particle analyzer. Chemical Engineering Science 1998;53(10):1883–99.

[230]Tim McKeen, Todd Pugsley. Simulation and experimental validation of a freely bubbling bed of FCC catalyst. Powder Technology 2003;129(1–3):139–52.

[231]Justin M. Weber, Joseph S. Mei. Bubbling fluidized bed characterization using Electrical Capacitance Volume Tomography (ECVT). Powder Technology 2013;242:40–50.

[232]Pita JA, Sundaresan S. Developing flow of a gas-particle mixture in a vertical riser. AIChE journal 1993;39(4):541–52.

[233]Porter L. CFD Simulation von Wirbelschichten. Masterarbeit. Freiberg; 2016.

[234]Syamlal M, O'Brien TJ. Derivation of a drag coefficient from velocity-voidage correlation. US Dept. of Energy, Office of Fossil Energy, National Energy Technology Laboratory, Morgantown, West Virginia April 1987.

[235]Gao J, Lan X, Fan Y, Chang J, Wang G, Lu C et al. CFD modeling and validation of the turbulent fluidized bed of FCC particles. AIChE journal 2009;55(7):1680–94.

[236]Wang J. A review of Eulerian simulation of Geldart A particles in gas-fluidized beds. Industrial & Engineering Chemistry Research 2009;48(12):5567–77.

[237]Wang S, Lu H, Zhang Q, Liu G, Zhao F, Sun L. Modeling of bubble-structure-dependent drag for bubbling fluidized beds. Industrial & Engineering Chemistry Research 2014;53(40):15776–85.

[238]Lv X, Li H, Zhu Q. Simulation of gas-solid flow in 2D/3D bubbling fluidized beds by combining the two-fluid model with structure-based drag model. Chemical Engineering Journal 2014;236:149–57.

[239]Chen S, Fan Y, Yan Z, Wang W, Lu C. CFD simulation of gas–solid two-phase flow and mixing in a FCC riser with feedstock injection. Powder Technology 2016;287:29–42.

[240]Asegehegn TW, Schreiber M, Krautz HJ. Numerical simulation and experimental validation of bubble behavior in 2D gas-solid fluidized beds with immersed horizontal tubes. Chemical Engineering Science 2011;66(21):5410–27.

[241]Esmaili E, Mahinpey N. Adjustment of drag coefficient correlations in three dimensional CFD simulation of gas-solid bubbling fluidized bed. Advances in Engineering Software 2011;42(6):375–86.

[242]Almuttahar A, Taghipour F. Computational fluid dynamics of a circulating fluidized bed under various fluidization conditions. Chemical Engineering Science 2008;63(6):1696–709.

[243]Taghipour F, Ellis N, Wong C. Experimental and computational study of gas–solid fluidized bed hydrodynamics. Chemical Engineering Science 2005;60(24):6857–67.

[244]Hiby JW. Untersuchungen über den kritischen Mindestdruckverlust des Anströmbodens bei Fluidalbetten (Fließbetten). Chemie Ing. Techn. 1964;36(3):228–9.

[245]Zenz FA. Regimes of fluidiazed behavior. In: Davidson JF, Harrison D, editors. Fluidization. London: Academic Press; 1971, p. 1–23.

[246]Wang J, Van der Hoef, MA, Kuipers JA. Why the two-fluid model fails to predict the bed expansion characteristics of Geldart A particles in gas-fluidized beds: a tentative answer. Chemical Engineering Science 2009;64(3):622–5.

[247]Schwarzer D. CFD-Simulation von Wirbelschichten mit Sekundärgaseindüsung. Masterarbeit. Freiberg; 2016.

[248]Wang Q, Zhang K, Brandanr S, Jiang J. Scale-up strategy for the jetting fluidized bed using a CFD model based on two-fluid theory. Canadian Journal of Chemical Engineering 2009;87(2):204–10.

[249]Zhong W, ZHANG M, JIN B, YUAN Z. Flow behaviors of a large spout-fluid bed at high pressure and temperature by 3D simulation with kinetic theory of granular flow. Powder Technology 2007;175(2):90–103.

[250]Wang W, Li J. Simulation of gas-solid two-phase flow by a multi-scale CFD approach—of the EMMS model to the sub-grid level. Chemical Engineering Science 2007;62(1):208–31.

[251]Igci Y, Andrews AT, Sundaresan S, Pannala S, O'Brien T. Filtered two-fluid models for fluidized gas-particle suspensions. AIChE journal 2008;54(6):1431–48.

[252]Schneiderbauer S, Pirker S. Filtered and heterogeneity-based subgrid modifications for gas-solid drag and solid stresses in bubbling fluidized beds. AIChE journal 2014;60(3):839–54.

[253]Couto ND, Silva VB, Monteiro E, Rouboa A. Assessment of municipal solid wastes gasification in a semi-industrial gasifier using syngas quality indices. Energy 2015;93, Part 1:864–73.

[254]Mazumder M, Wang T, Khan J. Design and Simulation of a Hybrid Entrained-Flow and Fluidized Bed Mild Gasifier: Part 1 - Design Considerations and Development of a Multiphase Model. Denver, USA; 2011.

[255]Papadikis K, Gu S, Fivga A, Bridgwater AV. Numerical Comparison of the Drag Models of Granular Flows Applied to the Fast Pyrolysis of Biomass. Energy Fuels 2010;24(3):2133–45.

[256]Singh RI, Brink A, Hupa M. CFD modeling to study fluidized bed combustion and gasification. Applied Thermal Engineering 2013;52(2):585–614.

[257]Xiong Q, Aramideh S, Kong S-C. Modeling Effects of Operating Conditions on Biomass Fast Pyrolysis in Bubbling Fluidized Bed Reactors. Energy Fuels 2013;27(10):5948–56.

[258]Zhou W, Zhao CS, Duan LB, Qu CR, Chen XP. Two-dimensional computational fluid dynamics simulation of coal combustion in a circulating fluidized bed combustor. Chemical Engineering Journal 2011;166(1):306–14.

[259]Zhou W, Zhao C, Duan L, Liu D, Chen X. CFD modeling of oxy-coal combustion in circulating fluidized bed. International Journal of Greenhouse Gas Control 2011;5(6):1489–97.

[260]Meyer B, Schurz M, Wolfersdorf C, Laugwitz A. Vergasungsreaktor zur Erzeugung von Synthesegasen aus festen Vergasungsstoffen mit Hilfe sauerstoffhaltiger Vergasungsmittel(2016).